CHARACTERIZATION OF NICKEL HYDROXIDE SLUDGE USING THE VARIABLE PRESSURE SEM

KEVIN ROBERTSON

DEPARTMENT OF MINING, METALS AND MATERIALS ENGINEERING

MCGILL UNIVERSITY
MONTREAL, CANADA
APRIL 2004

A THESIS SUBMITTED TO THE FACULTY OF
GRADUATE STUDIES AND RESEARCH
IN PARTIAL FULILLMENT OF THE REQUIREMENTS OF THE
DEGREE OF MASTER OF ENGINEERING

Your file Votre référence
ISBN: 0-612-98730-2
Our file Notre référence
ISBN: 0-612-98730-2

ACKNOWLEDGEMENTS

I would like to thank Profs. James Finch and Raynald Gauvin for their guidance, encouragement, boundless enthusiasm and financial assistance throughout this thesis.

Many thanks go to Ray Langlois who helped in the lab and to Helen Campbell who educated me on the usage of the microscope, as well as helping in sample preparation for the skirt measurement experiments. Special thanks goes to Dr. Rao for his assistance in the leach experiments. Profs B.J. Griffin and D.C. Joy must be thanked for their visits to the microscope as well as providing fruitful discussions.

I would like to acknowledge financial support of the Natural Sciences and Engineering Research Council of Canada (NSERC) under the NSERC Collaborative Research and Development program. This program is sponsored by Inco, Falconbridge, Noranda, Teck Cominco, COREM, and SGS Lakefield Research.

Finally, I would like to thank my mother who supported me every step of the way and my father and sister for helping me in times of stress. Thank you to my friends for their enthusiastic distractions, and of course to Lindsay.

ABSTRACT

Acid mine drainage lime treatment sludge is characterized with the variable pressure scanning electron microscope. The major components are shown to be detrital material such as silicates and clay minerals and neutralization products such as gypsum and metal hydroxides.

X-ray mapping and progressive sludge leaching experiments are performed to locate the major nickel bearing species. Progressive leaching was performed for two hours at pH 4, 3.5, and 3. It is observed that there is incomplete nickel extraction for all leach conditions. X-ray mapping establishes that the remaining nickel is due to minor amounts of Ni/S and Ni/O and more significantly colloidal sized nickel-silicon-aluminum complexes; which seem to result from neutralization.

Charge contrast imaging was also considered for characterization. It was studied on the mineral gibbsite to establish optimum working conditions for maximum contrast. Pressure, working distance, bias, scan rate and beam current are varied independently while the specimen current was monitored. Maximum contrast is shown to occur consistently at a specimen current of 3 nA. This implies that the user can operate over a wide range of conditions as long as the specimen current is maintained at its optimum value. This technique is then applied to the analysis of precipitated nickel hydroxides. Charge contrast proved not too informative because the particles are too small. Large electron doses at high magnifications can mask the subtle variation in local charging.

RESUMÉ

L'exhaure acide est charactérizeé par microscope électronique a pression variable. Les constituants principaux son des silicates, des minerais argileux, et des produits de neutralisation (gypse et hydroxides métalliques).

Les constituants majeurs de nickel sont déterminés par des experiences de lixivation de boue. La lixivation progressive a été performé pour 2 heures à des pH de 4, 3.5 et 3. Il a été observé que l'extraction de nickel était incomplète pour toutes les conditions. La cartographie par rayon x a établi que le nickel restant est sous forme de sulfides et d'oxides, mais principalement dans des complexes de Ni-Si-Al resultants du procédé neutralisation.

Le contraste de charge a aussi été considéré dans la charactérisation. En effet l'étude des minéraux de gibbsite a permis d'établir les conditions optimales à l'obtention du contraste maximum. La pression, la distance de travail, la vitesse de balayager, et le courant de faisceau ont été variés indépendamment pendant que le courant dans l'éechantillon était mesuré. Le contraste maximum existe à un courant de 3 nA. L'implication est que le microscopiste peut opéré le microscope sur une gamme étendue de conditions en maintenant un contraste maximum. Cette technique est appliquée à l'analyse de précipités d'hydroxides de nickel. Le contraste de charge ne fournit pas beaucoup d'informations puisque les précipités sont trops petits. De larges doses électroniques à de grandes magnifications peuvent masquer des variations subtiles de charge.

TABLE OF ACCRONYMS AND ABBREVIATIONS

AMD	Acid Mine Drainage
VP-SEM	Variable Pressure Scanning Electron Microscope
CSEM	Conventional Scanning Electron Microscope
FEG-SEM	Field Emission Gun Scanning Electron Microscope
CCI	Charge Contrast Imaging
CC	Charge Contrast
Pyrite	FeS_2
Pyrrhotite	FeS
HDS	High Density Sludge
I_{SC}	Specimen Current
I_b	Primary Beam Current
SE	Secondary Electron
BSE	Backscattered Secondary Electron
η	Backscattered Secondary Electron Coefficient
δ	Secondary Electron Coefficient
ESE	Environmental Secondary Electron
ESED	Environmental Secondary Electron Detector
I	Induced Current
$\tilde{E}$	Electric Field
V_d	Drift Velocity of Charged Particle
q	Charge Carrier
V_{bias}	Voltage Applied to Electrode at Pole Piece
GSED	Gaseous Secondary Electron Detector
SE1	SE Generated from Primary Electrons

SE2	SE Generated from BSE
SE3	SE Generated from BSE Colliding with Sample Chamber
EDS	Energy Dispersive Spectrometry
keV	Kilo-electron Volt
σ	Cross-Section
σ^{el}	Elastic Cross-Section
Z	Atomic Number
E_o	Incident Electron Energy
α	Screening Parameter
GPL	Gas-Path-Length
D	GPL
P	Pressure (Pascals)
T	Temperature (Kelvin)
I_p	X-ray Intensity Contribution from Non-Scattered Beam
I_m	X-ray Intensity Contribution from the Skirt Electrons
f_p	Fraction of Non-Scattered Electrons
m	Mean Number of Collisions Between Electron and Gas
λ	Mean free path
DHL	Duane Hunt Limit
CCWWTP	Copper Cliff Waste Water Treatment Plant
YAG	Yttrium-Aluminum-Garnet Crystal
UTW	Ultra Thin Window
ET	Everhart-Thornley Detector
WD	Working Distance
R_{90}	Radius of Skirt with 90 Percent of Electrons Counted

TABLE OF CONTENTS

LIST OF TABLES

LIST OF FIGURES

CHAPTER 1

INTRODUCTION

1.1 Background

1.1.1 Acid Mine Drainage Treatment Sludges

Acid mine drainage (AMD) is the term referring to an acidic effluent created through the oxidation of sulfide minerals. Chemical weathering of sulfide minerals represents a series of reactions where-by metals and other contaminants are released into the environment. Sulfides represent only a small portion of the valuable ore body, however, mining operations tend to expose large amounts to the atmosphere in their waste heaps (tailing ponds). The mining industry has been focusing with ever-increasing scrutiny on the generation and treatment of AMD due to the catastrophic effect it can have on the fauna and flora of a given area.

Active research in prevention of AMD generation involves the inhibition of sulfide oxidation [4]. Land covers and water covers have provided an adequate method of prevention, by isolating sulfides from water or oxygen [2]. Chemical inhibitors involve blocking reactive surface area by forming surface precipitates on the sulfides [4]. These preventative measures are adequate for new mines where AMD has not started, however, more active treatment processes are required for areas where AMD has been initiated.

There are many types of active treatment methods available due to the wide range of acidic effluents in the mining industry. Typical AMD treatment process are; neutralization through alkali dosing, sulfidization, sorption and ion exchange, membrane filtration, solvent extraction, electrochemical extraction, and biochemical extraction. The specific type of treatment is based on the economic-environmental cost benefit analysis of individual sites [4].

The most common treatment process is the neutralization of the AMD through the addition alkali materials. Chemical reactions between the AMD and alkali involve the removal of sulfate ions which increases the pH. Metal ions precipitate from solution as hydroxides in a sequence dependant on their individual solubility [1, 2, 3, 4].

Sludge is the metal-bearing by-product waste precipitate from the treated waste stream. It typically exhibits low weight percent solids, on the order of 5%. The low-density sludge results in large volumes, which poses problems in terms of handling and disposal. The chemical complexity of sludge prevents the release into the environment. The long term availability of neutralizing components diminishes, reducing the ability to buffer against pH decrease. Re-dissolution of metals results, exposing fauna and flora to potential environmental hazard. Storage of sludge is therefore the only viable option at present. Sludge must be stored in ponds, or they are returned to the tailings ponds, which is not a favorable solution [11].

A more beneficial approach to dealing with sludge is to remove the hazardous components entirely. AMD and resultant sludges are composed of the metals leached from the tailings ponds. The valuable metal content is elevated

enough to present economic gain, thereby turning sludge into a resource and not a waste. There appears to be significant amount of valuable metal in these sludges to make metal extraction favorable economically speaking. Results from metal extractive techniques such as flotation, electrowinning, bio-remediation, and solvent extraction however, have been less than favorable [3].

1.1.2 Characterization of Sludges

A characterization of these mine waste sludges is necessary in order to discover the best possible method for metal extraction. In this project, a mineralogical and structural analysis was performed on nickel hydroxide sludge from the Clarabelle mill in Sudbury, Ontario.

Characterization was performed primarily with the variable pressure scanning electron microscope (VP-SEM). The VP-SEM operates along the same basic principles as the conventional SEM (CSEM) in that a finely focused electron beam is irradiated across a specimen, generating various signals, giving topographic and compositional information [13]. The fundamental difference with the VP-SEM is that the chamber can be pressurized, allowing analysis of non-conductive materials without the need for a conductive coating. VP-SEM's also provide a new contrast mechanism due to interactions between the gas and trapped charge on the sample surface. This charge contrast imaging (CCI) allows internal microstructures to be observed that would otherwise not be seen with the CSEM [52]. These benefits of the VP-SEM make its use favorable for a characterization of hydroxide sludges in terms of mineralogical and structural analyses.

1.2 Objectives

The main objective of this project was to characterize nickel hydroxide sludge in terms of its mineralogy and structure in an attempt to facilitate the discovery of a metal extraction technique. Specific objectives were set to meet the main objective:

1. Perform a general qualitative analysis of the sludge to discover the mineralogy of the hydroxide particles.
2. Find optimal conditions for charge contrast imaging on a gibbsite particle which has become a standard for CCI. Apply these conditions to hydroxide particles in order to observe microstructures.
3. Model the beam spread (skirt) caused through the interaction of the primary beam and the gas particles, to facilitate microanalysis.
4. Perform a series of leaching tests on nickel sludge to observe the percent recovery of nickel as a function of pH.

1.3 Summary of Chapters

The thesis is divided into eight chapters. The first chapter provides a brief background on acid mine drainage and lime treatment sludges, as well as the overall objectives of the project. Chapter 2 is a survey of the literature pertaining to lime neutralization and the VP-SEM. The crystallization theory of these sludges is reviewed due to it's relevancy to a thorough characterization. Due to the majority of research being performed with the VP-SEM, an exhaustive review of the current state of knowledge is presented. Experimental procedures and techniques are reviewed in Chapter 3, as well as providing information on the location that the samples were taken. Due to the infancy of charge contrast as a method for analyzing microstructures, Chapter 4 is dedicated to obtaining optimal working conditions for observing this phenomenon. This chapter also reviews the application of this contrast mechanism to hydroxide sludge. In Chapter 5, the characterization of the beam spread is described, providing information on the potential hazards of using the VP-SEM for quantitative analysis. Chapter 6 presents the preliminary characterization of the nickel hydroxide sludge. A detailed description of the mineralogy and structure is provided in a qualitative manner. The results from leach tests are provided, focusing on the location of the nickel bearing species. Chapter 7 presents the conclusions as well as recommendations for future work in this area of research.

CHAPTER 2

LITERATURE REVIEW

2.1 Introduction

This chapter reviews the main fields of research pertaining to this thesis. The generation of acid mine drainage as well as the common types of mine effluent treatment are covered. A summary of previous work on sludge characterization is described in detail. Fundamental theory on the variable pressure scanning electron microscope is presented, providing advantages and disadvantages to its use in materials characterization.

2.2 Acid Mine Drainage

Typical sources of acidic mineral effluents are exposed road cuts, quarries, and mining sites [1]. Essentially, any site that has large quantities of exposed

sulfides will generate acidic effluents [2]. Mines tend to be the largest source for this effluent due to large scale rock removal and dumping, exposing significant amounts of acid producing material.

AMD can be generated from various materials including aluminosilicates, metal-oxides, organic matter and sulfides [3]. However, iron sulfides tend to represent the largest contributor to acid mine drainage due to their high reactivity when exposed to the atmosphere [4]. Marcasite, pyrite and pyrrhotite are the principle iron sulfides contributing to AMD, they are listed in terms of their reactivity [3]. Oxidation of pyrite produces an acidic effluent which leaches metals from other minerals in the tailings pond [1]. For this reason, AMD contains elevated concentrations of major rock constituents and heavy metals, sulfate and salt [2].

Metals and acid are released during pyrite weathering precipitating iron oxy-hydroxide (ochre), which is a red-brown mineral. Weathering represents a series of linked geochemical reactions, where, redox reactions are the fundamental driving process [3,4]. The following reaction is the fundamental starting point for pyrite oxidation.

$$2FeS_{2(s)} + 7O_{2(aq)} + 2H_2O \Rightarrow 2Fe^{2+} + 4SO_4^{2-} + 4H^+ \qquad [2.1]$$

As can be seen by equation 2.1, dissolved oxygen and water transforms pyrite into soluble Fe and S. If sufficient amounts of oxygen are present, ferrous iron oxidizes to ferric iron, which actually consumes acidity.

$$2Fe^{2+} + \tfrac{1}{2}O_2 + H_2 \Rightarrow 2Fe^{3+} + H_2O \qquad [2.2]$$

However, acid reduction is short lived, in that ferric iron reacts with water to form iron oxyhydroxide. Ferric iron also reacts with water and pyrite to further solubilize Fe and S.

$$2Fe^{3+} + 6H_2O \Rightarrow 2Fe(OH)_{3(s)} + 6H^+ \qquad [2.3]$$

$$14Fe^{3+} + FeS_{2(s)} + 8H_2O \Rightarrow 2SO_4^{2-} + 15Fe^{2+} + 16H^+ \qquad [2.4]$$

Therefore, it can be seen from equations 2.3 and 2.4, that ferric iron contributes significantly to the acid generation. The reaction between ferric iron and pyrite reduces ferric iron back to ferrous, which enables equation 2.1 to begin. This cycle of acid generation allows mine sites to generate AMD for decades, which emphasizes the fact that responsible prevention is necessary at the onset of a mining operation.

Pyrite oxidation depends on amount of pyrite, concentration of oxygen, and most importantly the availability of reactive surface area [1]. Increasing the surface area by a factor of 10 has been shown to increase the rate of pyrite weathering by a factor of 10 [4]. Surface area depends on particle size, morphology and porosity. Mining operations grind particles to very small sizes (<25um), which offers large amounts of surface area in the tailings ponds. This is another reason why AMD is so pervasive at mine sites.

2.3 Lime Neutralization

The mining industry has long used alkali dosing as the method of treatment for acid mine drainage, due to its simplicity and low cost. Adding an alkali consumes sulphate and increases the pH of the effluent. As pH increases, soluble/mobile metal ions begin to precipitate from solution to form metal hydroxides [2]. Flocculation of hydroxides allows for effective solid-liquid separation, yielding a final effluent meeting regulated limits [5].

The two primary choices for reagent are calcium hydroxide/oxide or sodium hydroxide/bicarbonate. Calcium reagents are more commonly used by the mining industry, primarily due to their low price and high rate of neutralization (reactivity). Lime has the ability to raise effluents to a very high pH in a relatively short period of time [2]. Calcium oxide (quicklime) is a dehydrated form of calcium hydroxide. It is generally cheaper than the hydrated form [5]. It is stored in silos and mixed with water to form slaked lime (hydrated lime slurry) [5]. The lime slurry is added directly to the effluent in order to raise the pH [4].

Sodium hydroxide (caustic soda) is used occasionally due to it's high rate of reactivity. A given mass of NaOH achieves a higher pH than the equivalent mass of quicklime. It is also much easier to handle than quicklime, posing less of a hazard. The cost is quite higher however, which is the main deterrent for its use in the industry [4]. The process of lime neutralization is not very complicated in terms of the chemistry. Lime added to the effluent raises the pH through the addition of hydroxyl ions. This process is described by the following equation:

$$Ca(OH)_2 \Rightarrow Ca^{2+} + 2OH^- \qquad [2.5]$$

This reaction is driven by the amount of lime that is added into the effluent [2].

As the pH raises, metal ions begin to precipitate out of solution in the form of hydroxides. The pH of precipitation varies for different metals in solution. Ferric iron precipitates at around pH 3, while nickel precipitates at a pH of 8. Due to this range, a high pH is used in order to precipitate all metals. Due to their amphoteric nature, it complicates matters when deciding what pH to operate at. The initial chemistry of the tailings pond and the acidic effluent determines the target treatment pH, however, pH 9.5 is commonly used as the target in most systems. Hydroxide formation can be described by this general equation [2]:

$$M^{x+} + xOH^- \Rightarrow M(OH)_x \qquad [2.6]$$

Hydroxides produced are gelatinous and they hold a great deal of water which decreases the solids density of the sludge [6].

The problem with lime neutralization is that it produces a high volume, low solids material that is quite unstable [5]. This means that these high volumes of sludge must be stored instead of released back into the environment. Sludge is typically stored in large ponds, where a natural gravity settling is allowed to occur. The water is recycled into the plants as process water. Sludge is also very often placed directly back into tailings ponds. This treats the problem of acid mine drainage but does not solve it.

In the last 30 years, a great deal of work has been done trying to improve the method of lime neutralization. Increasing the stability and the percent solids content for sludge has been the primary area of research [6,7].

Sludge treatment can be classified into three types, being basic, conventional and high density sludge (HDS) [2]. Aubé and Zinck (1999) suggest that the neutralization process affects sludge density, metal leachability, crystallinity, excess alkalinity and overall sludge stability [7].

Basic treatment involves direct lime addition to the acidic effluent. There is no pH monitoring meaning no control on the amount of lime added. Treated effluent is stored in a pond where natural settling occurs through gravity. The lack of control on the system generates a large volume, low percent solids sludge (1%-5%) composed of colloidal particles [5]. The particles tend to be porous which hinders the overall settleability. The size tends to be more heterogeneous, ranging from 5-45 microns [5].

The conventional treatment differs from the basic, in that it uses a greater amount of control over the process. A mix tank is used, which increases the agitation. A careful pH control is employed. The mix tank allows a more thorough reactivity, while pH monitoring increases the lime efficiency [5]. A flocculant is added to the effluent and sent to a clarifier. The underflow is generally sent to the tailings pond, while the overflow is released into the environment after pH adjustment. Conventional treatment produces sludge with larger particles and a slightly higher solids percent (3-10%) [5]. There is still a very large volume of sludge however, and the overall stability is low.

High density sludge (HDS) treatment process is a relatively new process which significantly increases the stability of sludge and the overall volume produced [6,8,9,10]. It follows the same principle as the conventional method, except the clarifier underflow is recycled back into the mix tank in specific ratios. This process improves the overall neutralization and settling characteristics of the sludge. Aeration improves the lime efficiency. A higher density sludge is produced (10%-30% solids) which results in a lower volume. Particles tend to become more homogenous in terms of size [7] as well as being denser and

spherical. The recycling process produces much denser particles which aids in the flocculation. This method is hindered by the higher initial cost of set-up. The initial investment is higher which can act as a deterrent.

2.4 Sludge Characterization

There has been a moderate amount of sludge characterizations performed to date. The most comprehensive sludge characterization study was undertaken under the Mine Environment Neutral Drainage MEND program, which was a multistake-holder program to study acid drainage in terms of its problem and solutions [11, 12]. CANMET performed a great deal of the sludge characterization work. This study sampled and characterized AMD sludge from a wide range of mines across Canada.

Sludge is difficult to characterize due to its high variability in the natural environment. The composition of sludge is directly influenced by the chemistry of the acidic effluent which in turn is a function of the tailings impoundment. Different mines will have different mine waste compositions which ultimately results in specific sludge compositions.

Generally speaking sludge has a high iron content. Iron sulfides are a common component of waste rock no matter what type of base metal mine we are dealing with. All sludges contain an amorphous phase which serves as the sink for many of the metal species. Gypsum is the main reaction product between calcium and sulfate. Detrital silicates are often found in the sludge. The sludge stability appears to depend on the stability of the amorphous mass rather than the other components.

The MEND program showed that solids density differences between basic and conventional AMD sludge are quite often negligible. HDS were quite a bit higher. Basic and conventional sludge ranges from 1% to 10% solids whereas HDS is closer to 30% solids. Aged sludge has a larger solids percent than fresh sludge by about 25%.

Particle size is often bimodal in sludge, this bimodality is believed to be related to different structures. The smaller size fraction related to the amorphous

hydroxide mass. The larger size fraction is believed to represent the unreacted lime and detrital silicates.

Sludge is alkaline, ranging between a pH of 8 and 11. As mentioned above the alkalinity depends on the process used and the specifications designated by the mine chemistry and environmental factors in the case of aged sludge.

Base metals are present in high concentrations, representing a potential for metal recovery. Trace level chemicals often include arsenic, boron, cadmium, chromium, mercury, and lead. Sulphate content is a direct relation to the amount of sulphur present in the waste rock.

The major mineralogical phase appears to be hydrated, amorphous, and metal rich. Typical metals found in this phase are the base metals, these tend to be leached quite readily. Carbonates and silicates are more crystalline and they tend to stabilize the amorphous phase.

2.5 Variable Pressure SEM

The variable pressure scanning electron microscope (VP-SEM) is the generic name given to an SEM that operates with a gaseous environment in the sample chamber. Electron scattering processes occur in the gas, creating an ionized gas species which neutralizes charge accumulation at the sample surface. The pressure and type of gas can be altered in order to analyze a wide range of uncoated non-conductors and hydrated materials. There is a suite of variables which must be monitored in order to optimize the use of this instrument. The following section presents the basic theory behind this technology as well as techniques for optimizing its usage.

2.5.1 General Differences between CSEM and VPSEM

A conventional SEM (CSEM) requires a high vacuum in the sample chamber and column in order to obtain a highly focused electron beam. The presence of gas in the column would scatter the electron beam to the point where

a focused probe would be impossible to obtain. Adsorption of molecules onto the filament would create burn outs, making imaging impossible [13]

Charge implantation typically occurs in specimens under high vacuum because the total electron yield falls below unity at beam energies above a few keV [13,14]. Grounded conductive materials allow for charge dissipation, however, an isolated conductor or non-conductor will not. Charge quickly accumulates in non-conductors resulting in image drift, distortion, and electrostatic reflection of the primary beam [15].

Equation 2.7 describes the relationship between electron yield and charge neutralization [17].

$$I_{sc} = I_b[1-(\eta+\delta)] \qquad [2.7]$$

Where, I_{sc} and I_b are the specimen current and primary beam current. The secondary electron (SE) and back-scattered electron (BSE) emission coefficient is denoted with η and δ respectively and is an indication of the amount of electrons emitted from the sample surface [13]. When SE and BSE emission is low, more electrons are implanted than ejected resulting in a negative specimen current. At unity, the specimen current is zero resulting in a charge balance. Electron emission is controlled by beam energy, therefore charge neutralization occurs at a specific beam energy as denoted by the E2 and E1 values in Fig. 2.1. Below E1 and above E2, negative sample charging is observed. Typical values for E1 are under 1 keV and around 3 keV for E2.

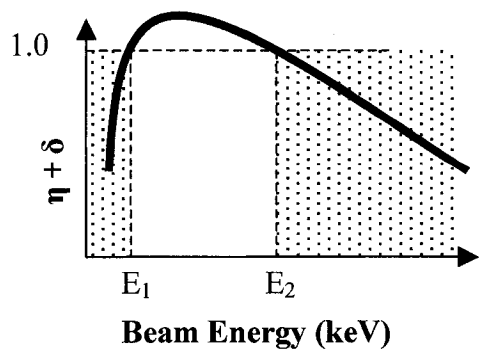

Figure 2.1. SE and BSE emission as a function of beam energy. At E_1 and E_2, emission is at unity indicating charge balance. Shaded region indicates negative charging.

Charging can be eliminated by operating at the E1 and E2 accelerating voltage. Low voltage charge neutralization has some drawbacks however. E1 and E2 values are material dependant creating heterogeneous charge accumulation across the sample surface. E1 values are also often too low to operate at therefore, for homogeneous samples the user is limited to one electron beam energy which can hinder the ability to perform adequate microanalysis.

The traditional method for imaging non-conductive specimens is with a thin conductive coating of carbon or gold-palladium several nanometers in thickness, which allows the charge to flow to ground [13]. A conductive coating is not ideal however due to image and signal artifacts created during image acquisition and X-ray microanalysis. Small microstructures on the sample surface can be masked as well as a reduction in the signal-to-noise ratio (S/N). Low energy signals and X-rays can also be absorbed in this thin coating which limits the reliability of the results in microanalysis [16].

The VP-SEM avoids these problems through a process of ionized gaseous charge neutralization. The VP-SEM acts as a parallel plate gas capacitor in order to amplify and collect electrons emitted from the sample surface [17]. A positively biased electrode at the pole piece along with the negative charge on the sample surface create an electric

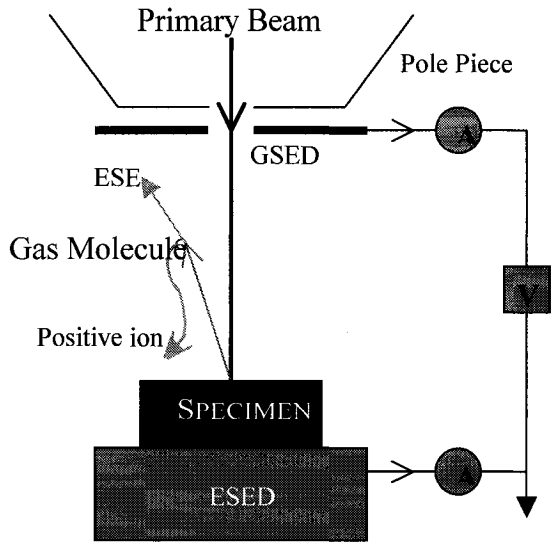

Figure 2.2. An emitted SE accelerates towards the positively biased electrode until it reaches the critical ionization energy, where it starts to ionize the gas molecules. An "environmental" secondary electron (ESE) is ejected and a positive ion is formed. The ESE accelerates and ionizes another molecule creating a cascade/amplification effect.

field in the sample chamber. This field accelerates low-energy electrons towards the pole piece as in Fig. 2.2. Ionization events between the accelerating electrons and gas molecules produce an 'environmental' SE (ESE) and a positive ion. ESE and SE continue to produce more ionization events, resulting in a cascade amplification effect. Fig 2.3 shows this amplification effect. The positive ions, due to the electric field, drift towards the sample surface where they recombine with free electrons to neutralize charge build-up [18].

The pressurized chamber is achieved through the use of a vacuum gradient between the chamber and the column. A differential pumping system allows for this gradient as well as the presence of pressure limiting apertures. Differences between brands relates to the quality of the vacuum gradient as well as the maximum attainable pressure [19]. A complete vacuum in the column is the desired situation but it is rarely achieved. There will always be some gas that enters into the column, which reduces the life span of the filaments as well as the resolution of the imaging probe. Benefits of this system include electron signal amplification, leading to higher contrast images and charge neutralization at the sample surface through positive ion recombination with electrons. The disadvantage such as beam spread will be discussed in a later section.

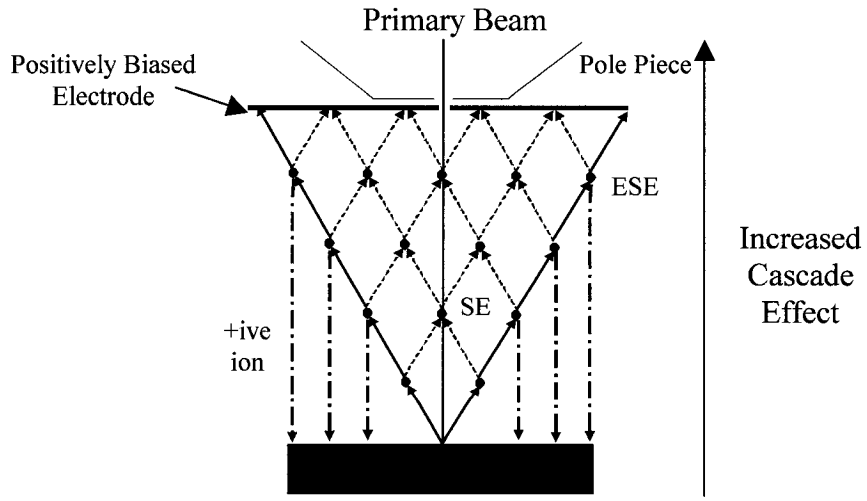

Figure 2.3. The accelerated SE collides with a gas molecule which ejects an ESE and leaves a positive ion behind. The SE and ESE accelerate in the field where more collisions occur. The result is an amplification effect, where majority of ionization events occur near the pole piece. The positive ions drift towards the sample surface.

2.5.2 ESED Detector

Everhart-Thornley detectors cannot be used in the VP-SEM because the high voltage applied to the scintillator and faraday cage would ionize all of the gas creating electrical breakdown [17]. Until recently the VP-SEM has been limited to the use of a BSE detector for imaging.

Danilatos [21] described a way to use the charge carriers produced during amplification as the imaging signal. Imaging is possible through collection of the induced currents from SE's and ESE's at the pole piece or from the positive ions at the sample stage.

The induced currents are generated from the electric field ($\bar{E}$) and the drift velocity of the charge carrier (q) in the sample chamber.

$$I = \widetilde{E} \cdot v_a \left(\frac{q}{V_{bias}}\right) \qquad [2.8]$$

Where, I is the induced current, v_d is the drift velocity of the particle and V_{bias} is the voltage applied to the electrode at the pole piece [17,23]. The biased plate, the sample and the gas behave like a virtual capacitor as described by Ramos's (1939) theorem [17]. The sample and the biased electrode are the negative and positive plates, while the ions and electrons are considered space charges. The space charge moves due to the influence of the electric field, which uses energy. This

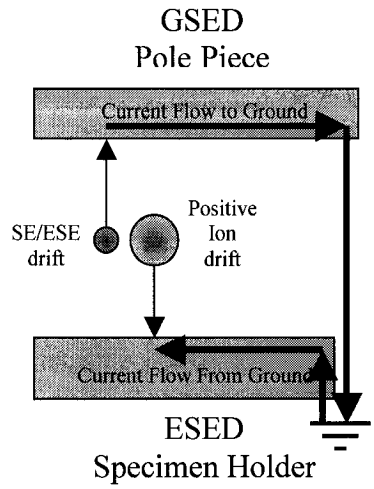

Figure 2.4. Positive ions drift towards sample and induce current from ground, SE/ESE induce a current in the GSED towards ground.

energy is derived from the potential between the plate and the sample (electric field strength) and results in current flow in the circuit.

The GSED is a proprietary device which measures the induced current from the electrons, whereas the ESED is the generic name given to the detector measuring the current induced from positive ion drift. The GSED measures the induced current at the pole piece and the ESED measures the current induced at the specimen stage. The SE/ESE's collide with the GSED and create a current flow *to* ground. The positive ions recombine with electrons at the ESED, which creates current flow *from* ground (Fig 2.4). Therefore, for the ESED, the current is based on the ion flux striking the sample surface [17, 21].

The electric field, gas pressure and gas type influences the degree of ionization events per unit length which effects the ion flux and the resultant ESED current [24]. The ion flux is also a function of the incident and emitted electron currents due to their role in the gas ionization process [16]. An increase in SE production will ionize more gas molecules, which will in turn increase the ion flux [17]. The specimen current is based on the emissive properties of the sample as well as the specific operating parameters used, such as pressure, working distance and plate bias.

2.5.3 Signal-Gas Interactions

The presence of gas in the chamber complicates the interactions between the primary beam, the sample, and the emitted signals. In a CSEM, the primary electrons penetrate the sample and undergo elastic and inelastic collisions. Through this process, SE, BSE, X-rays, auger electrons and photons are emitted [13]. Secondary electrons can be further grouped into SE1, SE2, and SE3. SE1 are created from the scattering of primary electrons. SE2 are generated from the scattering of BSE. SE3 are generated from BSE colliding with the sample chamber. Of these three types of secondary electrons, only the SE1 provide a useful signal at high accelerating voltages. The other signals only decrease the signal to noise ratio [13].

Introducing a gas into this environment further complicates matters because the amplification process does not discriminate against spurious signals [25]. All secondary electrons regardless of their origin will ionize gas, contributing to the cascade. Figure 2.5 provides a comparison of the particle interactions between the VP-SEM and a CSEM. Interactions between the gas and the emitted signals are very important to the imaging mechanisms of this microscope as described in the above section. Secondary electrons collide with the gas molecules and create an ionization event as long as the energy is above the ionization threshold [26,27]. Acceleration increases the particles' energy past the threshold for ionization thereby initiating the cascade effect [28].

Beam-gas interactions involve the scatter of the primary beam electrons due to elastic and inelastic collisions with the gas. The scattered primary electrons interact with the sample and generate SE, BSE etc. outside of the area of interest. Skirt electrons generate all of the signals mentioned above, the only difference being that they contribute entirely to the background [25]. Gas-sample interactions involve the collision of positive ions on the sample surface [29]. Positive ions recombine with electrons on the sample surface and

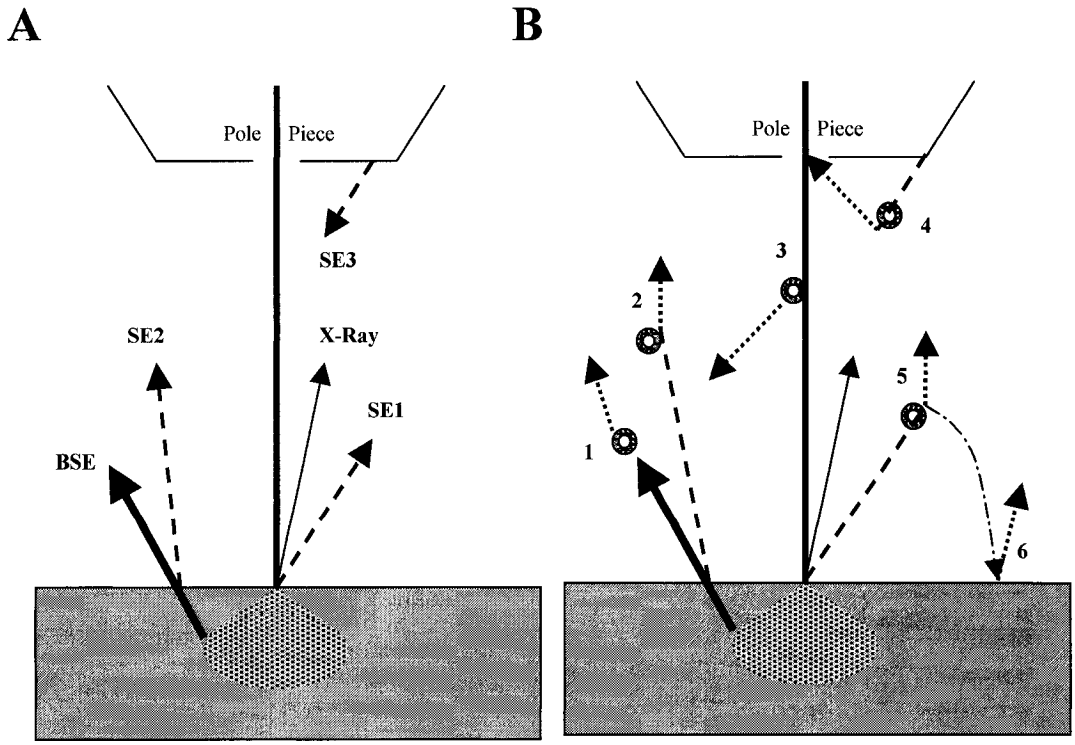

Figure 2.5. **A**. Particle interactions in the CSEM. **B**. Particle interactions in the VP-SEM. Same behaviour as in the CSEM accept the signals interact with the gas. 1. BSE-gas 2. SE2-gas 3. PE-gas 4.SE3-gas 5. SE1-gas 6.Positive ion-sample emits SE.

neutralize the charge build-up [26]. Upon impact however, secondary electrons can be emitted which contribute to the cascade. This behavior decreases the signal-to-noise ratio as well [25, 29].

It is quite clear, that there is a strong source of background noise in the VP-SEM. However, it has been shown by Danilatos [28] and Farley and Shah [20, 22] that the overall resolution does not become hindered as long as the central probe is still generating a strong enough signal. Fletcher [25]; suggests that this unwanted signal contribution can be minimized by using a gas with a low ionization efficiency at low pressures.

2.5.4 Skirt Effect

Understanding the interactions between the beam electrons and the gaseous molecules is of paramount importance in order to properly characterize a material. Skirting is a phenomenon that is well known yet properly designed models still elude us. Many variables come into play which can complicate these interactions.

Beam electrons scatter as they pass through the chamber, due to elastic collisions with gas molecules. Each electron has a finite number of collisions, which can be defined by a poisson distribution [14, 19]. It is important to mention that when the average number of collisions is high, there are still some electrons that have not been scattered at all.

Skirting affects the image resolution and more importantly the ability to perform quantitative analysis with EDS X-ray microscopy. This section will explore the theory behind skirting as well as the variables which affect it. A detailed description of experiments to measure the skirting effect as well as the potential ways in correcting or reducing the skirt will be given.

2.5.4.1 Elastic Cross-Section

Scattering can be described as a discrete process whereby each beam electron interacts independently of the others. Scattering of an electron in the VP-SEM occurs when it passes within a critical distance of a gas particle.

In order to model the skirt effect, one has to understand the electron-gas interactions. Scattering is in large part a function of the probability that an event will take place. This probability is defined as the cross-section (σ). The cross-section can be referred to as the effective "size" that the atom presents as a target to the incident electron. The cross-section however, in reality is quite smaller than the physical size of the target atom [13]. Cross-sections are a function of the atomic density of the gas molecule. Therefore specific operating parameters are important in order to minimize the skirting effect. Once various cross-sections are known for specific conditions, electron distributions resulting from these collisions can be modeled [37].

Farley and Shah [20], Moncrieff [36], and Danilatos [21, 28] provide a method for calculation of these cross-sections based on work done by von Engel 1955 [34]. These calculations are difficult and prone to errors due to problems associated with molecular clustering and vibrational effects which alter the values for cross-sections. Most cross-sections in the literature have been calculated for solids and what little work has been done with gases is in pressures and electron energies well outside the range of SEM's. Gauvin [38, 39] suggested using a Rutherford cross-section which has been shown to be valid for light elements at low electron energies and heavier elements above 10 keV. Most of the work performed on the VP-SEM is above 10 keV, therefore Rutherford cross-sections are assumed to be valid. Calculation of the elastic cross-section is:

$$\sigma_i^{el} = (5.21\times10^{-21})\times\left(\frac{\pi Z_i^2}{E_0^2\alpha_i(1+\alpha_i)}\right)(cm^2) \qquad [2.9]$$

Where, E_0 is the incident electron energy (keV), Z_i is the atomic number of element i and α_i is a screening parameter:

$$\alpha_i = (3.4\times10^{-3})\times\left(\frac{Z_i^{2/3}}{E_0}\right) \qquad [2.10]$$

Recently, He and Joy [37] proposed a technique for the experimental measurement of the cross-section in the VP-SEM, based on the technique developed by Gauvin [38]. Cross-sections are measured through the variation of X-ray intensity excited by the un-scattered probe as the pressure is changed. The sample consists of a small target less than 25 μm in diameter, embedded in an epoxy of different chemical composition. As the pressure is increased, more electrons become scattered away from the focused beam, these scattered electrons do not generate an X-ray signal on the target. Therefore, by measuring the X-ray intensity as a function of pressure, the variation in scattered electrons can be observed.

Calculation of the cross-section can then be performed using an equation derived from Gauvin et al., (2000) [40]:

$$\ln(I) = -\left(\frac{D\sigma_T}{RT}\right)P + \ln(I_0) \qquad [2.11]$$

Where I is the measured X-ray intensity measured at pressure P, D is the distance between the sample and the point where the electron enters the gaseous chamber (gas path length), σ_T is the total elastic cross section, which is a function of gas type and accelerating voltage, R is the perfect gas constant, and T is the temperature in Kelvin. Seeing as the above equation is linear, the slope can be rearranged to calculate the elastic cross-section as in equation 2.22:

$$\sigma_T = -\alpha\frac{RT}{D} \qquad [2.12]$$

Where, α is the value of the slope. The calculated cross-section includes all elastic and inelastic events.

The authors [37] show that there is some discrepancy between the experimental and theoretical cross-sections at low beam energies and low pressures. It is believed that at low beam energies there is an increased inelastic contribution that is not accounted for in the theoretical models. At low pressure,

gases are molecular instead of atomic, which affects the size of the target (cross-section). He and Joy [37], show that the molecular cross-section of N is larger than twice the atomic cross-section of N, which is an assumption made by Moncrieff [36]. The cross-section for air tracks that of molecular nitrogen, not atomic nitrogen. These observations allow for more accurate modeling of skirt effects in the VP-SEM.

2.5.4.2 Skirt Behaviour

A great deal of work has been accomplished in terms of the dependency of electron scatter on specific variables. It appears that pressure, gas type, working distance, and accelerating voltage have the greatest influence on the degree of electron scattering [41].

Danilatos [28], Gilpen and Sigee [42], Mathieu [29], and Kadoun et al [43] have shown the relationship between gas-path-length (GPL) and skirting. Gas-path-length is the distance that the primary electron travels in the pressurized chamber. Using a copper target on a carbon background, Gilpen and Sigee [42] showed that a shorter GPL relates to less scattering. This is intuitive when the cross-section and mean free path are taken into account. Decreasing the distance that the electron travels will mean that statistically, less collisions will occur in the chamber. This work led to the development of longer detector assemblies, which reduced the gas-path-length. Not all VP-SEM's use long detector assemblies due to patent restrictions.

Griffin [45] used a copper target and measured k α peak intensity as a function of pressure and accelerating voltage. The copper target was fixed as the beam was moved various distances away. Carlton [46], measured the skirt by focusing the beam through a platinum aperture 200 um in diameter. Measuring the platinum counts is relative to the amount of scattered electrons hitting the aperture. The authors showed that the percentage of scattered electrons increases with pressure and accelerating voltage. Increasing pressure created more scattering events in the microscope effectively increasing the intensity and radius

of the skirt. Decreasing accelerating voltage increases the degree of scattering as well.

Griffin [45] showed that pressure had a greater influence on scattering than did accelerating voltage. Carlton [46] also showed that GPL has the greatest effect on the scattering of electrons, however this effect decreases with lower pressures (< 133 Pa).

Wight [41] used a high purity copper block mounted in a non-conductive epoxy in order to compare experimental and theoretical results of scattering. The author measured the radial size and the intensity of the scattered electrons in the skirt. Comparison was made with a monte carlo program designed by Joy [47]. Results showed good agreements with the general trends however there was a systematic deviation from theoretical results.

It is of great benefits to minimize the effect of the skirt in the microscope. Previous research has shown that optimum conditions for minimizing the skirt are low pressures, high accelerating voltage, short GPL, and use of a gas with a low elastic cross-section. Some samples however require higher pressures and lower accelerating voltages, which complicate matters. There is a always a trade-off with electron microscopes however.

2.5.4.3 Skirt Correction

Knowledge about the behaviour of the skirt as well as why it occurs is invaluable information when performing microanalysis so as not to misinterpret information. However, in order to perform accurate quantitative analysis the skirt must be eliminated or corrected. This section reviews the three correction techniques that have been developed.

Beam stop Method

The beam stop method as described by Mansfield [48] consists of a fine needle of a known element which is not present in the sample. The needle is placed under the electron beam, effectively shadowing the area of interest. An X-ray spectrum is recorded, which essentially is the skirt contribution seeing as the

electron beam is prevented from hitting the sample. The beam stop is then removed, and another spectrum is collected. This spectrum contains contribution from the beam as well as the skirt. The first spectrum is subtracted from the second spectrum, the difference is the X-ray contribution solely from the focused beam. Mansfield [48] tested this method, showing that the subtraction of spectra is not perfect resulting in erroneous results.

Pressure Variation Method

The pressure-variation method developed by Doehne [49] uses the variation in X-ray intensity with pressure as a way to extrapolate to 0 Pa. Two spectra are recorded at different pressures. Spectrum B is subtracted from spectrum A resulting in spectrum C.

$$C = B - [(A - B) \times D] \qquad [2.13]$$

Where, B is the second spectrum, A is the first spectrum and D is an empirical adjustment factor used to correct changes in the background shape. There are two assumptions associated with this equation, the first is that spectrum A has a larger intensity than B, which is valid considering B is taken at higher pressures. The second assumption is that the changes in skirt intensity are more important than the radius. This assumption has been shown to be valid by Danilatos [28].

As the pressure reduces, so do the peak intensities which are a contribution from the skirt. The contribution from the non-scattered electrons increases and the relative X-ray peaks increase as well. Extrapolating this relationship to the zero pressure regime provides the X-ray intensity of the area of interest.

Mansfield [48] shows that there is good agreement between linearly extrapolated intensity and those obtained in high vacuum. It is observed however, that the variation of X-ray intensity with pressure is not always linear [38].

Gauvin Method

Gauvin [38] suggests a variation to the Pressure-Variation method for skirt correction. The following equation is a derivative of the pressure-variation method,

$$I = (I_p - I_m)f_p + I_m \qquad [2.14]$$

where, I is the intensity at a given pressure. I_p is the intensity contribution from the non-scattered beam, I_m is the intensity contribution from the skirt and f_p is the fraction of non-scattered electrons. Equation (2.25) should be linear (y = mx + b), therefore plotting I versus f_p is linear. Extrapolating I to f_p of 1 (no scattering) provides the corrected intensity. Once f_p is experimentally known for any I, the correction procedure can be used for any pressure.

The value for f_p must be known for the specific operating conditions at the time of the experiments. These f_p values can be calculated theoretically or measured experimentally. Experimentally measuring is quite simple with the proper sample. The target must contain an element that is not present in the rest of the sample. This ensures that the unscattered electrons are being measured through the emission of characteristic X-rays. Dividing the peak intensity at a given pressure by the peak intensity at zero pressure provides the ratio of un-scattered electrons (fp).

Calculating f_p theoretically is not quite as simple, but Gauvin [38] does provide a method to do this. The poisson distribution for electron scattering can be described by the following equation:

$$P(x) = \frac{m^x e^{-m}}{x!} \qquad [2.15]$$

Where, P(x) is the probability that an electron will be scattered x times. The average number of collisions is denoted by m. As described [19], for x=0, the probability that an electron will not scatter at all is:

$$P(0) = e^{-m} \quad [2.16]$$

Where P(0) is the fraction of non-scattered electrons (f_p). According to Danilatos [28], if a single scattering model is used, that is if one assumes that electrons only undergo one scattering event,

$$m = \frac{D}{\lambda} \quad [2.17]$$

where D is the GPL and λ is the mean free path.

$$\frac{1}{\lambda} = \rho\sigma \quad [2.18]$$

$$\rho = \frac{P}{kT} \quad [2.19]$$

therefore,

$$f_p = e^{\frac{-PD\sigma}{kT}} \quad [2.20]$$

where. P is pressure, D is GPL, σ is the total elastic cross-section, k is boltzmanns constant, and T is temperature in Kelvin.

From this point one needs to know the GPL and the total elastic cross-sections at a specific pressure and gas type. As mentioned above, GPL changes with pressure and elastic cross-sections are difficult to calculate. Therefore this method for f_p calculation is prone to errors. Gauvin et al [44] showed that the GPL can vary with pressure which alters the value of f_p. He and Joy [37] show that total elastic cross-section measured experimentally differ from theoretical. Therefore it is important to obtain accurate measurements of both GPL and total elastic cross-sections.

2.5.5 Charge Contrast Imaging

Charge Contrast Imaging (CCI) is a unique imaging mode detected in the ESEM and VP-SEM that has recently been documented by Griffin [50,51] and

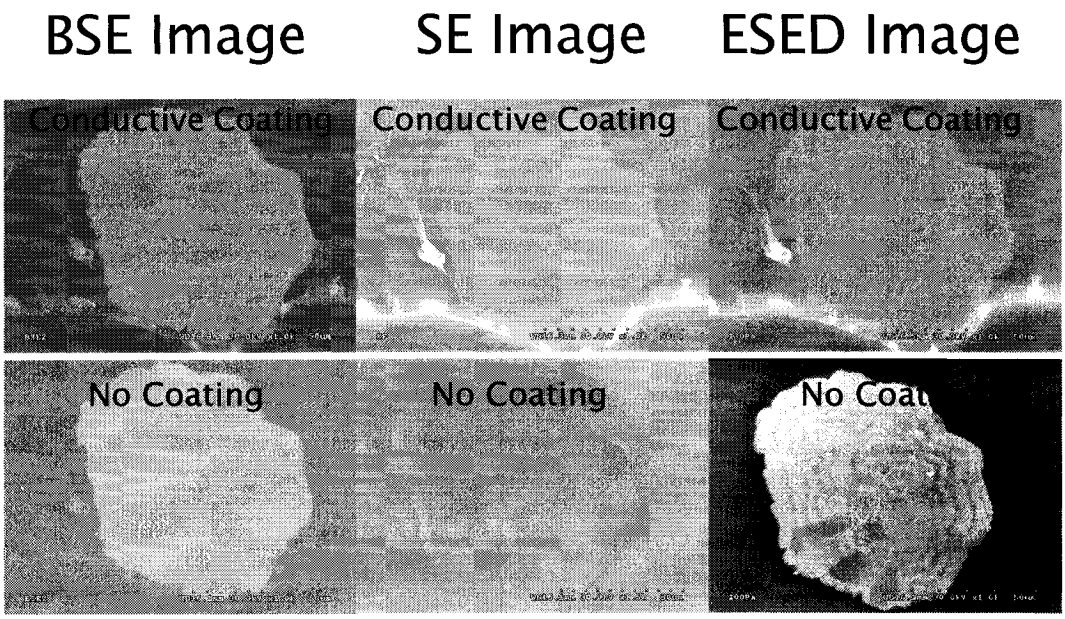

Figure 2.6: Comparison of a gibbsite particle imaged under an ESED, BSED, and SE detector. Comparison as well of the coated and uncoated sample. The uncoated gibbsite imaged with the ESED detector is the only one that shows CCI.

Toth [53]. CCI provides information about the microstructures of non-conducting materials that are not seen with conventional SE and Backscattering Electron (BSE) imaging modes [52]. Figure 2.6 compares a gibbsite particle imaged under three different detectors. It can be seen that the image taken with the ESED detector offers a great deal more information than the SE and BSE detectors. It has been shown the growth rings are related to preferential calcium precipitation during a batch precipitation process. CCI has been observed in many materials such as gibbsite, calcite, zircon, silicon, and sphalerite.

Charge contrast imaging is still in the process of being understood, and the actual mechanism which produces the CCI is still debatable. Charge contrast is believed to be caused by complex interactions between SE emission, local variations in trapped charge, the ion flux and the induced electric field. It has been hypothesized that the CCI is related to the electron-ion recombination in the specimen as well as enhanced secondary electron emission due to trapped charge [31, 53].

Toth et al., 2002 suggests that a field assisted SE emission in areas with localized charging may be the cause for CCI. Charge trapping is highly

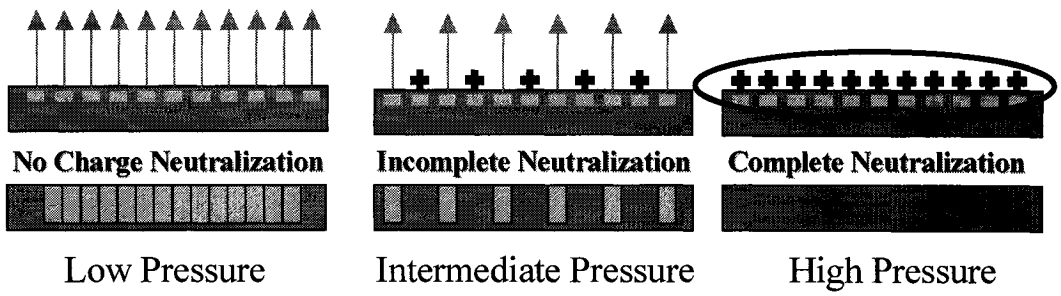

Figure 2.7. At low pressure, there are no positive ions to neutralize the free electrons on the sample surface. As the pressure increases, an increase in ion flux begins to neutralize the charge build-up. Areas of increased charge density will be further amplified. As the pressure is increased above the optimal charge compensation, all of the charges are neutralized.

dependant on crystal lattice defects, dislocations, grain boundaries, impurities and vacancies [51]. Therefore it can be hypothesized that the charge contrast the structural features just mentioned. Modeling charge build-up however, is very complicated due to the dynamic nature of the electric fields, as well as the complex variation in charge trapping. Charging is sample dependant therefore a mechanism to describe charge contrast would be sample dependant as well.

Another model, invoked by Griffin [51] suggests that charge contrast is caused by an optimum charge compensation at a given pressure allowing mapping of surface potential differences in materials, giving an enhanced sensitivity in SE emission. Figure 2.7 provides an example of this model.

Incomplete charge neutralization allows preferential charging to occur in areas where there is increased charge trapping. This is typically observed in areas with increased defect densities and lattice heterogeneities. Areas of compositional and structural variation will show differences in charging which results in contrast variations called charge induced contrast. It has been shown that this charge contrast is related to the effect of charge neutralization because the contrast is not seen with the SE or BSE detectors [14].

It can be seen that the suggested mechanisms for CCI revolve around the intrinsic electrical properties of the material as well as the extrinsic effects of the ion flux and electric fields. The ion flux maybe of greater importance because the microscopist has more control over the parameters. Heterogeneous ion flux across the specimen surface can cause variations in the rates of recombination,

leading to insufficient localized charge neutralization and resultant contrast [53]. Changing pressure, working distance and bias gives the ability to control the degree of neutralization in the sample. This means that it is possible to obtain conditions where maximum CCI is observed. It is fair to say that most materials will have a different set of optimum conditions for CCI because their intrinsic characteristics differ from each other.

A great deal more work must be performed in order to develop a rigorous model for the charge-induced contrast. Great steps towards this model have been achieved using Duane Hunt Limit experiments [53, 54] in order to examine the relation between PE landing energy, increased SE emission and charging. Griffin has provided a great deal of work proving that CCI is not seen in SE and BSE imaging modes, as well as linking the contrast with cathodoluminescence which is related to defect density measurements.

CHAPTER 3

EXPERIMENTAL

3.1 Introduction

This chapter is concerned with the techniques and procedures used for the experiments. Sampling locations for the nickel hydroxide sludge will be described, as well as the sample preparation techniques. A thorough description of the instrumentation as well as the methodology behind the various experiments is presented.

3.2 Geology and Hydrology

The composition of acid mine drainage and the resultant treatment sludge is dependant on the waste rock and/or tailings as well as the methods for treatment. Characterization for this project was conducted on AMD treatment

sludge from the INCO operation in Sudbury, Ontario. Therefore, a description of the major minerals as well as the general hydrology will be presented.

The geology of Sudbury is comprised of an igneous complex, divided into four groups. The first three layers consist of silicates and aluminosilicates, while the fourth is primarily composed of disseminated and massive sulphide ore. This sulphide layer is the host for the Ni-Cu-PGE bearing minerals which are of interest economically.

The primary ore minerals are pentlandite [$(Ni,Fe)_9S_8$] and chalcopyrite [$CuFeS_2$], while the primary sulphide gangue mineral is pyrrhotite (FeS). All gangue is pumped to the Clarabelle Mill tailings impoundment.

The hydrology of the area is shown schematically in Figure 3.1. Acid runoff from the tailings impoundment is fed into the Copper Cliff Creek, which flows towards the wastewater treatment plant. Slaked lime slurry is added directly to the stream, elevating the pH to 10.5 as described in Chapter 2. Organic and inorganic debris is removed through a screening process before the effluent is pumped into the treatment plant. The overflow is pumped to the sludge pond where it is allowed to gravity settle.

The sludge in the treatment plant undergoes solid/liquid separation in a clarifier. A flocculant (Magnifloc) is added to increase the rate of settling. The clarified water is sent to a pH control facility to be released into the environment. The underflow is a voluminous, low % solids sludge, which is pumped to the tailings impoundment.

Sludge in the sludge pond is dredged yearlyand stored in the tailings impoundment. Surface water is pumped continuously back into the Clarabelle Mill to be used as process water.

3.3 Sample Locations

Fresh sludge was collected in order to see the evolution of sludge over time. Fresh samples were taken from the Copper Cliff Creek Waste Water Treatment Plant (CCCWWT), on its way to the tailings dump. Therefore the fresh samples are the clarified, voluminous, low density sludges.

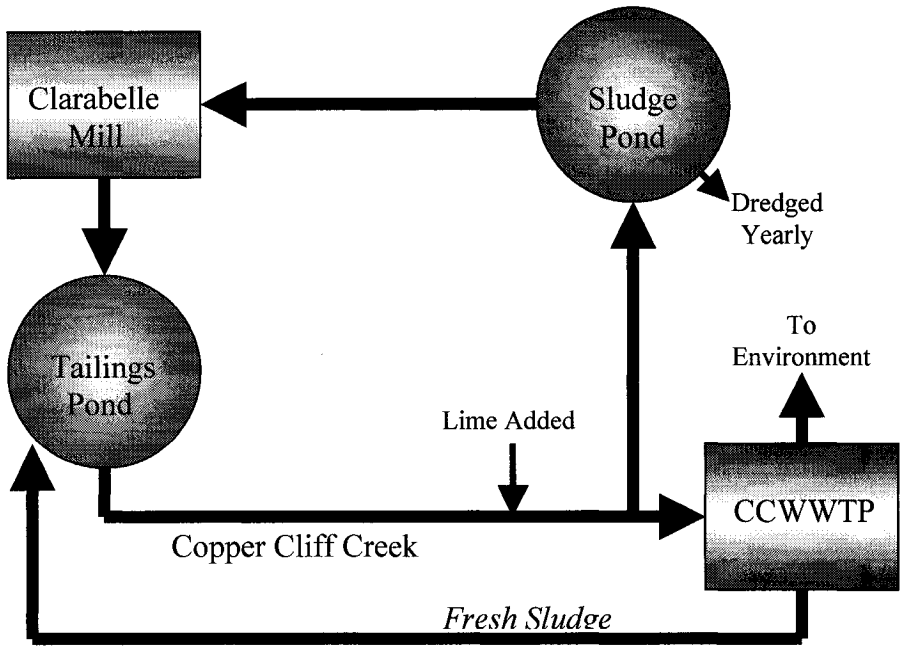

Figure 3.1. Rejects from the Clarabelle mill are stored in the tailings pond. AMD runoff is collected in Copper Cliff Creek, where lime is added directly. Sludge is pumped to the waste water treatment plant and clarified. Underflow is pumped to the tailings pond and clarified water released into the environment. Sludge pond is dredged yearly and pumped to the tailings pond.

3.4 Sample Preparation

Sludge samples were stored in seal tight 20 L plastic pails for transport back to the lab. Fresh samples were air-dried the day after collection in order to minimize chemical alteration. Air-drying in a fume hood took between one to two days. Dried samples formed large aggregates comprising small and large particles. The samples were ground in an attempt to re-liberate the particles. The small size of the hydroxides made this a difficult task, however.

Analysis of materials under the microscope involved either mounting on an aluminum stub or embedding in an epoxy or bakelite resin. Epoxy mounting involved the addition of the dried sample into a mount form. A two-part epoxy mounting resin from Clemex Technology was poured into the mold and mixed in order to wet all the particles. The mount was allowed to dry over 24 hours for the resin to cure.

Bakelite mounting involved adding a sample into the mounting chamber of a LaboPol 3 from Struers and covering with a bakelite powder (Leco

Corporation). A force of 20 kN and temperature of 180° is applied for 6 minutes followed by a 3 minute cooling. Bakelite is generally non-conductive, however there is a conductive form called Polyfast, available from Struers which is heavily loaded with conductive carbon. Advantages of bakelite are ease of preparation as well as the potential for producing a conductive media. A significant shortcoming is that high heat may alter the sample.

Samples were removed from their molds and ground on 240 grit abrasive SiC paper from Bueler until the sample was sufficiently flat. Samples were then ground with 320, 400 and 600 grit papers in order to remove the grinding marks. The final polish was performed with suspended alumina powders of 5μm, 1μm and 0.3μm on a Struers LaboPol5, using a Struers polishing cloth.

When necessary, non-conductive samples were coated with a gold/palladium layer several nanometers in thickness, using a Hummer VI sputter coater from Anatech Ltd.

3.5 Instrumentation

The VP-SEM operates with a tungsten hairpin filament as the electron source. It is equipped with an Everhart Thornley secondary electron detector and a YAG backscattered electron detector. The scintillator in the BSE detector is made of single crystal yttrium-aluminum–garnet (YAG). As described in chapter 2, the VP-SEM is also equipped with an ESED detector designed by Hitachi. A Si(Li) crystal energy dispersive spectrometer from Oxford instruments is used with an ultra thin window (UTW). The resolution on this detector is 138 eV at 5.9 keV.

The field emission SEM is operated with a wire of single-crystal tungsten fashioned into a point and attached to a hairpin filament. This cold field emitter offers a much smaller electron beam than SEM's using a hairpin filament, allowing for much greater resolution. This microscope is equipped with a Robinson backscattered electron detector and an upper and lower secondary electron detector. The lower detector operates in the same manner as an Everhart-Thornely (ET) detector in that it collects all secondary electrons (SE). The upper

detector is located in the column, outside the sample chamber. Through electric and magnetic fields, SE1 spiral up the beam and into the column, leaving the SE2, SE3 and SE4's behind. Therefore, the upper detector provides an image with a high signal-to-noise ratio. The EDS system is an identical Oxford system as used on the VP-SEM.

3.6 Procedures

The following section describes the procedures and techniques of data interpretation for all the experiments in this thesis. It is divided into four sections: charge contrast imaging, skirt modeling, sludge leaching and sludge characterization.

3.6.1 Charge Contrast Imaging

Charge contrast was observed on the Hitachi S-3000N VP-SEM using the Environmental Secondary Electron Detector (ESED), with air as the gas in the sample chamber. CCI was detected on gibbsite and observed on a nickel hydroxide sample.

Gibbsite specimens were obtained from the McGill Geology department, which were precipitated from a seed crystal in several batches resulting in growth rings. These growth rings are imaged with the ESED detector in a gaseous environment. The gibbsite particles were mounted in an epoxy based resin and

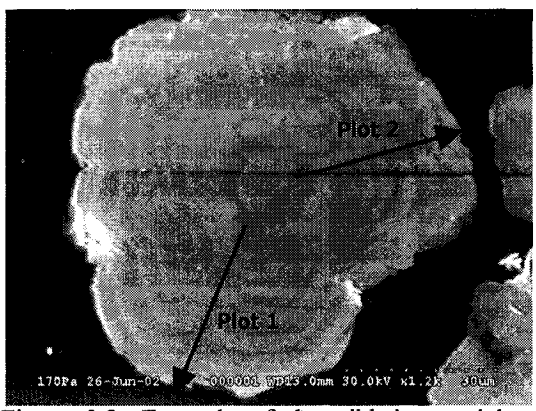

Figure 3.2: Example of the gibbsite particle used for the contrast measurements. The linescans were taken across the ring structures in the top right and bottom left areas.

allowed to dry for 24 hours. Once dried, the samples were ground to a level where there was a maximum amount of gibbsite grains in cross-section. The experiments were performed in order to see the variation of the charge contrast as a function of selected parameters: Pressure, plate bias, working distance, beam current, and scan rate are all factors which affect the ion flux and hence the degree of charge contrast. These parameters were varied independently while the other variables were kept constant. Images were taken for each set of conditions and the pixel linescan was taken as in Fig 3.2. The brightness and contrast controls were held constant throughout the experiment and the magnification was kept constant as well. The specimen current was measured for each image to correlate with the measured contrast.

Ni-Hydroxide particles were obtained from C. Cist of the McGill Hydrometallurgy group. One sample had been recycled 4 times and the other sample 10 times. The idea was to see if these recycled particles showed ring structures, similar to the gibbsite particles.

All the images used for CCI measurements were produced from the microscope's supplied imaging system. The images were captured using a Quartz PCI program installed on the microscope and saved as TIFF files for analysis on an image analysis program. The grayscale values in this case are determined by the image capture program on the microscope and are carried over to an external image processing program. The contrast was measured using Scion Image, obtained from www.ScionCorp.com. Line-scans were taken across areas experiencing charge contrast and the percent contrast was measured using equation 3.6.1. Max and min are the measured pixel intensities of the brightness levels on a grayscale of 255. For each image, two line-scans were taken and described as plot 1 and plot 2.

$$C = [(Max-Min)/(Max+Min)]*100 \qquad [3.6.1]$$

As seen in Fig 3.3, each image has a line-scan with a different mean intensity due to the differences in the absolute brightness. In order to compare the

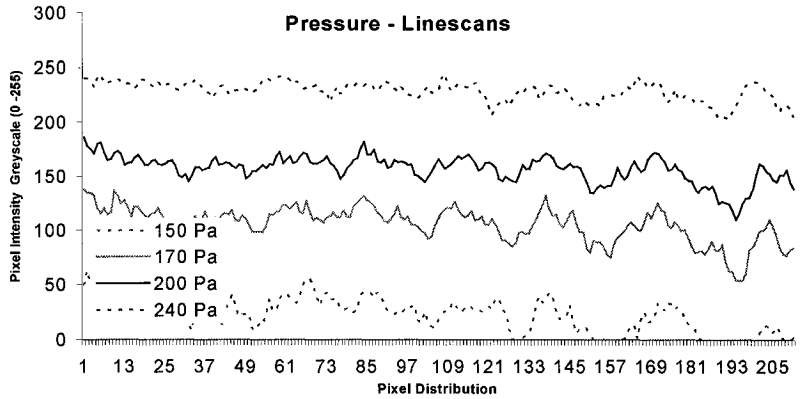

Figure 3.3.Graph of pixel intensities across the face of a gibbsite crystal for various pressures. Normalization required before measuring the percent contrast.

mean intensities, the line-scans for each condition were scaled so that they had the same mean intensity at 128. This normalization of line-scans allows for direct comparison of the contrast for each image

3.6.2 Skirt Modeling

Skirt modeling experiments were performed to properly determine the effect of the skirt on X-ray analysis. A comparison of experimental and theoretical models is presented in the results section.

A Monte Carlo program called GAZ has been developed by R. Gauvin, to model the electron behavior in various gases. Pressure, working distance, and type of gas are the main input parameters. This program uses Rutherford cross-sections as the values for calculating the probability of an elastic collision, and the following scattering of the electron beam. This program assumes no energy loss in the gas, which is a good approximation.

Two experiments were conducted on the microscope designed to measure the radius of scattering and the percent of scattered electrons. The first experiment involved scanning the electron beam over the interface between bakelite and an infinite copper block over a range of pressures as in Figure 3.4.

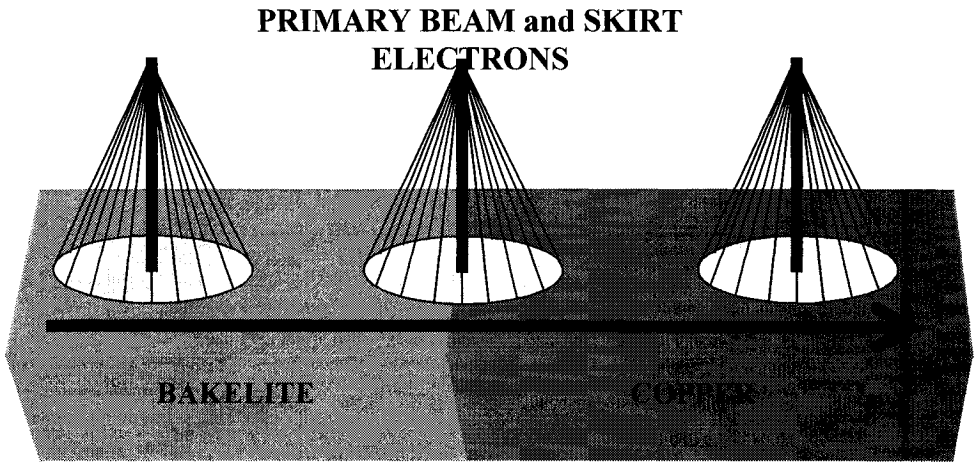

Figure 3.4. Schematic of the skirt radius experiment and a sample linescan. As primary beam scans towards the copper block, skirt electrons interact and increase the copper X-ray intensity. Once the beam is in the copper block, the X-ray intensity

The radius is calculated by obtaining the X-ray line-scans for copper and measuring the distance from the interface at which copper is first detected.

Measurements above 100 Pa were not taken because the skirt radius was larger than the field of view for the microscope. However, results were accurate enough to establish a trend line and extrapolate to maximum pressure of 270 Pa. Results showed that there was a background contribution due to the bremmstrahlung. An average baseline was measured from the first 150 pixels and applied to the entire line-scan. Radius measurements were taken from the point where the line-scan deviates from the baseline.

Measurement of the percent scattering (f_p) was performed on various samples including copper wire of differing radii and chalcocite (CuS) particles ground below 25 μm. The beam was focused onto the center of the objects and the pressure was varied. Scattered electrons hit the bakelite and epoxy whereas

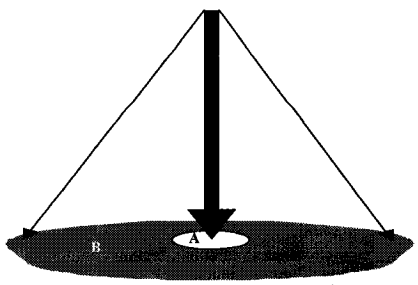

Figure 3.5: Geometry of the experiment to measure f_p. B represents the epoxy and A represents a target with diameter less than 25 μm. A and B must be of differing composition and the sample must be coated with a conducting media.

the unscattered electrons hit the copper as seen in Figure 3.5. Comparing the copper signal at high vacuum with the one from the pressure variation gives the percent scattered electrons as the pressure is varied.

3.6.3 Sludge Characterisation

Fresh sludge was air dried for several days creating an aggregate. The sludge was ground using a rolling pin and mortar and pestle. The ground sludge was separated into 8 size classes, which on investigation showed no significant chemical difference. Investigation also showed there were three main phases in the sludge: Small sized hydroxide slimes, larger detrital material, and the process well as from the water. Separation of these components allowed for a greater degree of characterization.

The samples were imaged under optical microscope in an attempt to classify on the basis of color. The VP-SEM and FE-SEM were used to obtain high magnification images and to perform the chemical analysis. The results for sludge analysis as a whole as well as in its component parts will be given.

3.6.4 Sludge Leaching Experiments

The basis for this aspect of the project is that metal extraction from sludge is not very efficient; there is always metal remaining in the sludge after conventional and/or amine leaching. Characterization will help determine in which phases the metals are located. Progressive leaching was performed on the sludge to reveal the refractory phases.

The sludge was leached with sulfuric acid. Three experiments were performed at pH 4, 3.5 and 3 as a function of time (0.5,1,1.5 and 2 hours). The pH was kept constant by addition of acid and the samples were agitated throughout the process. Twelve samples were thus generated in order to anlalyze the nickel distribution. Chemical assaying was performed, giving the percent iron and nickel. These results were correlated to X-ray microanalysis data using the VP-SEM. Emphasis was placed on locating the major sink for the nickel, whether it is forming new compounds or is still in its original form.

CHAPTER 4

CHARGE CONTRAST IMAGING

4.1 Introduction

This chapter is concerned with the experiments pertaining to charge contrast. The crux of the work was performed on gibbsite, however complementary tests were performed on nickel hydroxide.

4.2 Gibbsite

The results presented show the variation in the maximum contrast with a variation in electrode bias, working distance, pressure, scan rate and spot size. These variables tend to show a quantitative change in contrast and specimen current as they are altered. As described above, the specimen current is a function

of the ion flux as well as the degree of electron emission. These values were not monitored individually throughout the experiments therefore, the change in specimen current cannot be directly attributed to one or the other. The images used in this study are presented in Appendix A.

It must also be noted that the electric field produced in the chamber represents the potential difference between the biased electrode and the samples' steady-state value. The information provided in the section on bias is based on the direct values of the applied bias, not the potential difference. The results however, still provide useful information in terms of absolute changes in the specimen current.

The working distance is the distance between the sample and the pole piece, not the distance between the sample and the biased electrode. Since the distance between the biased electrode and the pole piece is constant, the same trends would be observed had the information been presented as the distance from the sample to the biased electrode.

The section on beam current represents the variation of the contrast as a result of changing the overall spot size. This parameter is specific to the microscope as well as from day-to-day use; however, the information provided shows qualitatively, the effect on specimen current and contrast.

4.2.1 Bias

The gibbsite images in Figure A.1 in Appendix A were obtained over a range of biases from 100 V to 300 V while maintaining the other microscope conditions at a pressure of 150 Pa, a working distance of 15 mm, a fast scan rate, a spot size 55 % of the maximum and a magnification of 1200X.

It is evident by looking at the images that the greatest contrast is observed at higher bias voltages. The greater the bias, the greater the acceleration of the secondary and environmental secondary electrons. Increasing the bias increases the amplification and overall brightness and contrast. Increasing the bias changes the electric field which alters the field assisted SE emission.

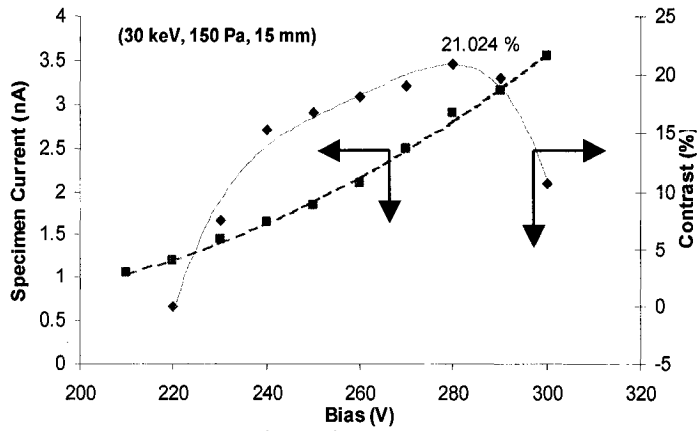

Figure 4.1: Contrast and specimen current measurements for bias. Greatest contrast occurs when specimen current is 2.9 nA which relates to a bias of 280 V.

Line-scans show the difference in terms of the brightness and clarity of the images at 300 V. The calculated % contrast shows that the greatest contrast is observed at higher voltages, as seen in Figure 4.1. There is a maximum contrast at around 280 to 290 V. Decrease in contrast after the maximum might be attributed to suppression of the SE emission due to an increase in the ion flux. The maximum contrast for the gibbsite occurred when the specimen current was at 2.9 nA.

4.2.2 Working Distance

The working distance for the gibbsite specimen was varied from 5 to 15 mm by one millimeter increments while maintaining the same conditions for all the other variables. Figure A.2 shows the image set obtained at the working distances of 8 mm, 10 mm, 13 mm and 15 mm respectively. It is noted that the brightness of the images increases with the working distance. The measured specimen current in Figure 4.2 shows a steady increase with increasing working distance, which explains the increased brightness of the images. An increase in specimen current is expected to occur due to an increase in ionization events between the electrons and the gas molecules. However, as the working distance is increased, there is an increase in the back-ground noise due to primary beam

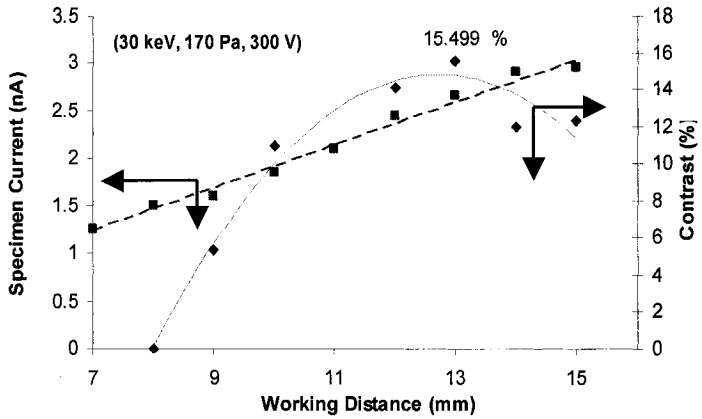

Figure 4.2: Contrast measurements and specimen current measurements for working distance. The greatest contrast occurs when the specimen current 2.9nA which corresponds to a WD of 13 mm.

ionizations This complicates matters when determining which factors are affecting the specimen current.

The measured contrast in Figure 4.2 for the line-scans shows an increase in contrast with specimen current until a maximum is reached around 13 or 14 mm. At this point the contrast decreases due to a decrease in SE emission from the ion cloud. Comparing the contrast with the I_{SC} in Figure 4.2 shows that the maximum contrast occurs around 2.5 to 3 nA, which is close to the range observed for the bias

4.2.3 Pressure

The CCI was observed for a range of pressures between 120 Pa to 270 Pa as seen in Figure A.3. The other parameters were maintained at 30 keV, a bias of 300 V, a slow scan rate, 15 mm working distance, and beam current of 60%.

A line scan was taken across the face of the particle in order to compare the observed contrast under various conditions. The resultant line scans show that the brightest image was 120 Pa and the darkest overall image was at 270 Pa. Calculation of the contrast shows that the greatest contrast is at 150 Pa. A surface plot shows that 150 Pa produces the greatest contrast between the growth zones in the gibbsite. The observed specimen current measurements show an increase in

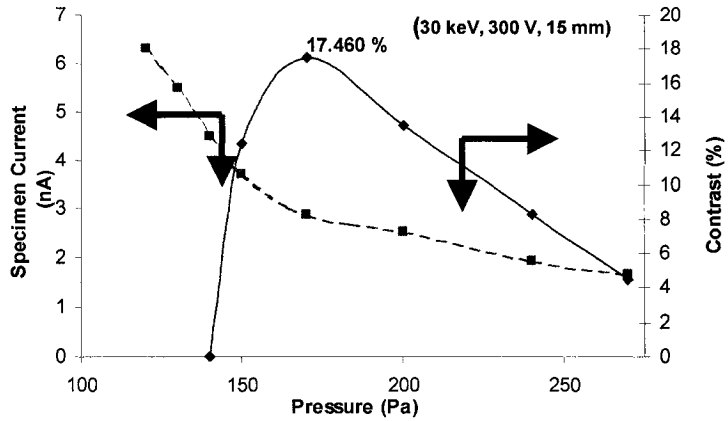

Figure 4.3: The contrast measurements and specimen current measurements for pressure. The greatest contrast occurs when the specimen current is 2.9.

specimen current with a decrease in pressure. At higher pressures, charging is visibly reduced due to the coupling of positive ions and negative electrons on the surface.

Comparing the percent contrast with the specimen current shows that maximum contrast occurs at pressures between 150 and 170 Pa, which corresponds to a specimen current around 2.9 to 3.7 nA. This is within the same range as the specimen currents for the working distance.

4.2.4 Scan Rate

Images in the data set were taken for four different scan speeds. The images in Figure A.4 show that there is an optimum scan rate for maximum contrast. Even though the image is not as clear, the overall contrast between the growth zones is better at the second fastest scan rate.

Comparing specimen current to scan rate shows that as the scan rate decreases as the specimen current increases. A fast scan rate means that the electron beam has shorter dwell time, resulting in a smaller electron dose. A smaller electron dose would result in a decrease in charge trapping and a resultant decrease in the field assisted SE emission. The longer the dwell time of the beam on an area, the more SE's will be generated due to larger electron doses which

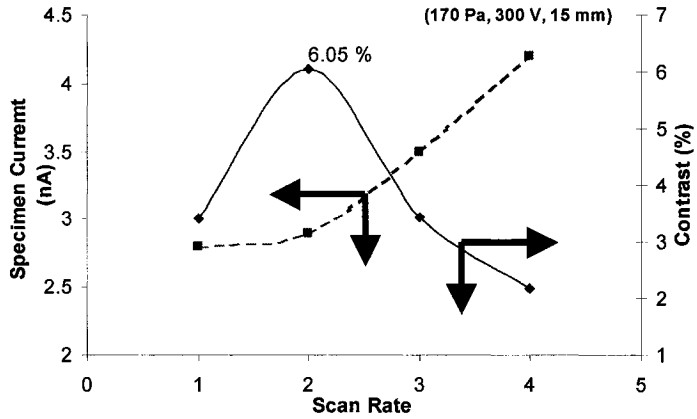

Figure 4.4: The contrast measurements and specimen current measurements for scan rate. The greatest contrast occurs when the specimen current is 2.9 nA

leads to more amplification and a greater specimen current. The linescans confirm the observed contrast in the images. Calculating the % contrast shows an interesting relationship between the contrast and the scan rate. The maximum contrast is observed at the scan rate #2, at a specimen current of 2.9 nA for both linescans. This maximum may be attributed to the larger dwell times on the sample surface. An increase in the beam dosage may mask subtle variations in local charging.

4.2.5 Beam Current

Charge contrast imaging (CCI) was observed for different beam currents while maintaining constant conditions for the other variables. The beam current was varied while at 30 keV, 150 Pa, 15 mm working distance and 300 V bias. A stronger beam current means a larger spot size and more electrons induced in the specimen. A beam current of 70% yields a larger spot size than a beam current of 30%, according to the design of the Hitachi S3000N VP-SEM. CCI was obtained for beam currents from 58 to 70.

Comparing contrast with specimen current shows that there is an optimum specimen current for the maximum CCI. Figure 4.5 shows that the max contrast is observed when the I_{SC} is between 7 and 8 nA. When the specimen current is

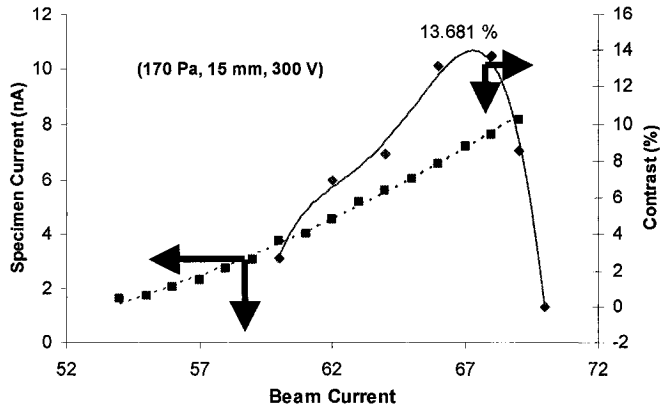

Figure 4.5: The contrast measurements and specimen current measurements for beam current. The greatest contrast occurs when the specimen current is 7.2 nA.

greater than these values the image becomes too bright and all contrast is lost due to the large flux of ions.

An account of the behaviour of charge contrast imaging as a function of typical operating parameters has been provided. This provides a useful method for identifying the optimum range of operation to observe the maximum contrast for gibbsite. Maximum contrast appears to occur at an optimal specimen current between 2.5 and 3.5 nA.

It should be noted that the reproducibility of these experiments is dependant on the microscope conditions. The quality and stability of the filament are very important, any deviation from the standard current will result in a different specimen current, and a different value for the maximum contrast. The values were reproducible in the sense that there always appears to be an optimum specimen current; however, the actual value changes, depending on the microscope conditions.

In the experiments performed, the greatest contrast for the growth zones were at high plate bias, low magnification, low pressure, high working distance, medium scan rate, and high beam current. The selected conditions were 30 keV, 150 Pa, 280 V, 13 mm, scan rate 2, 1200 X magnification, and a spot size of 68%. These values are not necessarily final due to the dependence on the specimen current. It was observed that some variation in the operating conditions was

possible. For example, if a specimen is used that charges quite readily, a high pressure is required to neutralization the charge. In so doing, the specimen current will decrease and the max charge-induced contrast will not be obtained. To compensate, the working distance could be increased in an attempt to increase the specimen current and return the value back to the optimum conditions.

The optimum specimen current for the gibbsite specimen was found to be between 2.5 and 3.5, but it is most likely not the case for other materials. Due to differences in dielectric properties and rates of charge dissipation, it is expected that materials will have different optimum specimen currents for maximum contrast. Much work remains to model charge accumulation in different materials.

4.2.6 Low Pressure Charge Contrast

To validate the proposed dependency of charge contrast on specimen current, imaging at low pressures is necessary. At low pressures, the ion flux reduces due to a decrease in ionization events. Therefore charging dominates and the resultant charge contrast is lost. Increasing the working distance, increasing the detector bias and decreasing the accelerating voltage are all viable options in order to obtain a balance between the ion flux and sample charging. It is also beneficial to minimize the amount of skirting that occurs so that the overall resolution is not compromised.

Increasing the bias is not possible because regular operation is already at the maximum of 300 V for this microscope. Increasing the working distance is possible; however, this drastically increases the percent of scattered electrons in the chamber. Decreasing the accelerating voltage increases the percent of scattered electrons as well; however, it would appear to have a lesser effect than the accelerating voltage.

Decreasing the accelerating voltage decreases the amount of charging that occurs on the sample surface, therefore a lower pressure attains the same amount of charge neutralization at 5 keV as a high pressure at 30 keV.

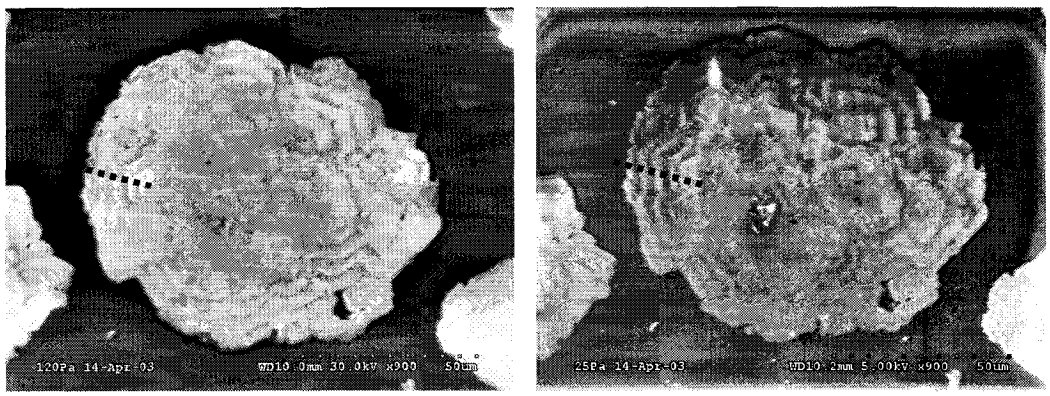

Figure 4.6: Comparison of Gibbsite charge contrast at 120 Pa and 30 keV with 25 Pa and 5 keV. The observable contrast between growth rings appears to be greater in the image at 25 Pa and 5 keV. This represents a balance between the ion flux and the sample charging. Dotted line represents area that linescan was taken.

Figure 4.6 compares two gibbsite particles taken at different operating conditions. One image was taken at 120 Pa and 30 keV and the other at 25 Pa and 5 keV. Figure 4.7 is a plot of the pixel intensity across the growth rings. The plots have been normalized to a mean intensity of 128 on the greyscale value. The comparison shows that they are very similar in terms of peaks and troughs. Percent contrast was measured on the three peaks marked in Fig. 4.7. Table 4.1 presents the percent contrast and the average contrast over the three measurements. It can be seen that the percent contrast at 25 Pa and 5 keV is greater than that for 120 Pa. Therefore, this opens the ability for the user to operate the microscope over a wide range of conditions and still have good charge contrast.

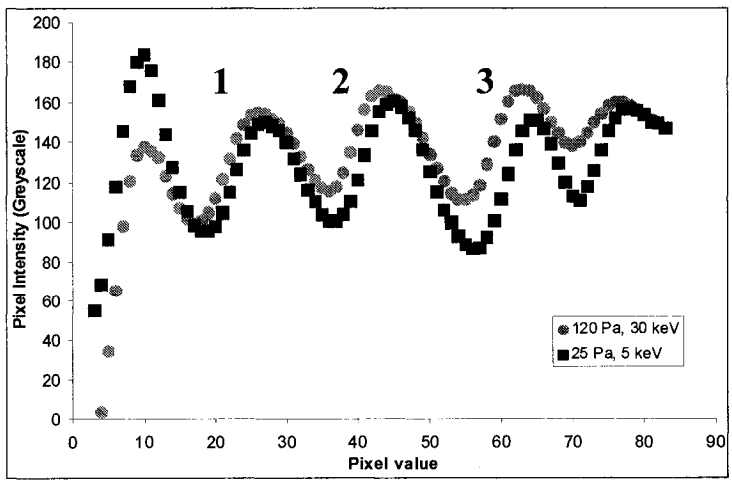

Figure 4.7: Plot of the pixel intensities for the two images in Fig. 4.6. The linescans have been normalized to accommodate for variations in the absolute brightness.

Table 4.1: Percent contrast measurements for the linescans across the growth rings of gibbsite at 120 Pa and 30 keV and 25 Pa and 5 keV. The percent contrast is greater for 25 Pa and 5 keV

	120 Pa, 30 keV	**25 Pa, 5 keV**
Measurement 1	21.6	21.9
Measurement 2	17.7	23.1
Measurement 3	19.9	27
Average	**19.7**	**24**

4.2.7 Reverse Contrast

Reverse contrast is a phenomena that has not been documented to any great extent in the literature. B. Griffin of the University of Western Australia has only observed it a handful of times [54].

Reverse contrast, as the term implies, is a reversal of the charge contrast on the particles, the brighter rings become dark and vice versa. Figure 4.8 presents results where reverse contrast was observed. This phenomena is not well understood and at present there is no agreed explanations.

4.3 Nickel Hydroxide

The application of charge contrast imaging to nickel hydroxides arises from the need to distinguish among individual colloidal size hydroxide particles in an aggregate. Hydroxide sludges are typically elevated in iron and magnesium

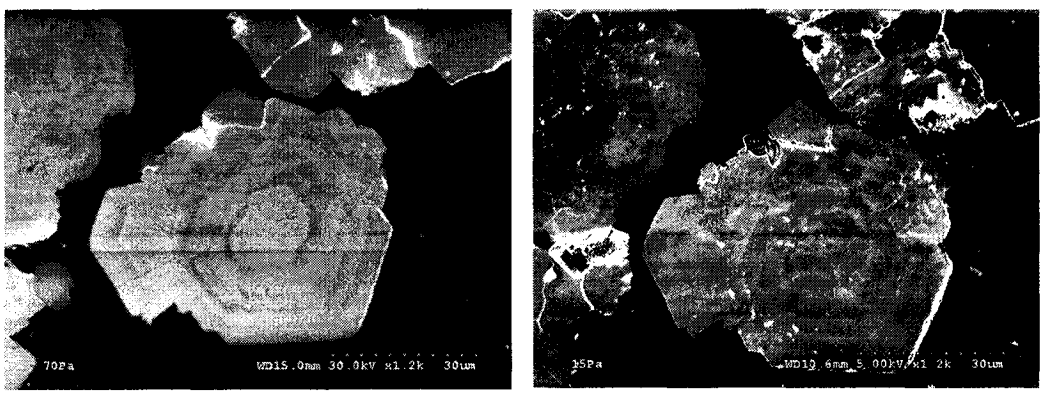

Figure 4.8: Comparison of the same gibbsite particle at two different operating conditions. Normal contrast observed at 70 Pa, 15 mm GPL, and 30 keV. Reverse contrast observed at 25 Pa, 10.6 mm GPL and 5 keV.

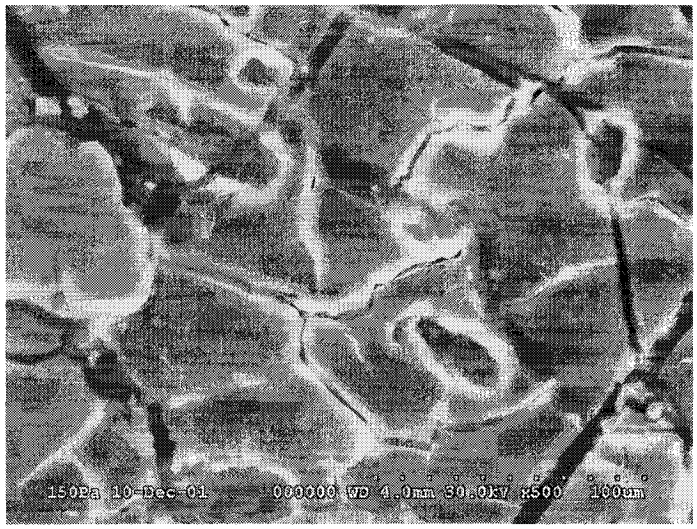

Figure 4.9: Image of dried fresh sludge particle, large inclusion on the left is a silicate, medium sized oval dark inclusions are calcium sulphate and the matrix is predominantly metal hydroxides.

hydroxides as well as the base metal of interest; in this case, it is nickel. A typical image of these sludges is presented in Fig. 4.9. There are large inclusions in a featureless matrix. These inclusions are predominantly silicates, clays and calcium sulphate. The matrix is composed of iron, magnesium and nickel hydroxides; however, distinguishing between them is difficult. Figure 4.10 provides a comparison between the SE, BSE and ESED detectors. The images were taken at magnification of 2500X and a pressure of 25 Pa. The ESED and BSE images are of uncoated hydroxides while the SE image is of the same area but coated with gold/palladium. It is seen that the image produced from the ESED detector has more contrast than the SE and BSE images. It becomes more obvious that the matrix is comprised of hydroxide aggregates.

Increasing the magnification to 5000X as in Fig. 4.11 shows these individual hydroxide particles more clearly. The scale on this image is 10 μm therefore the average size of these hydroxides is 1 to 2 μm, which corresponds to the expected size range for colloidal hydroxide particles [11].

In terms of our current knowledge of charge contrast imaging, it can be said that the brighter areas in the hydroxide aggregates represent particles that

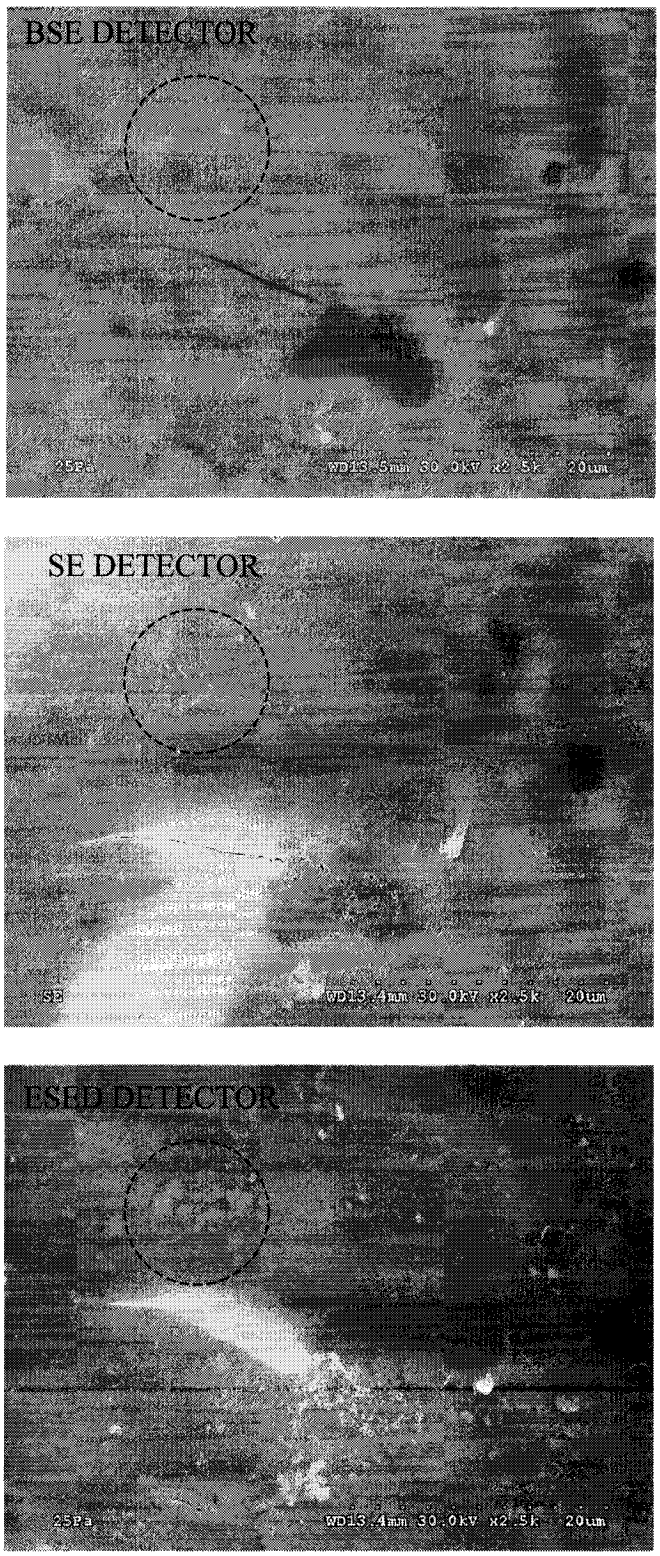

Figure 4.10: Comparison of hydroxide particles with three different detectors. Dotted circle emphasizes area of increased contrast in the ESED image

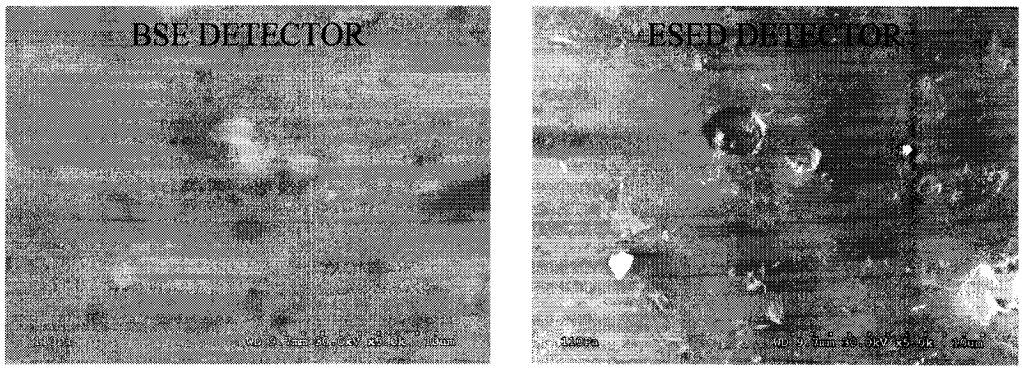

Figure 4.11: Comparison of hydroxide particles with the BSE and ESED detectors. The ESED image quite clearly shows enhanced contrast.

charge more readily than the surrounding areas. These particles require a greater degree of neutralization from the ions colliding on the surface. Therefore, assuming a homogeneous distribution of ions across the sample, these particles appear brighter and the contrast increases, thereby distinguishing individual particles from one another.

There is also a possibility that the ESED image shows more topographic contrast than the other two detectors. BSE images are generally absent of topographic contrast, whereas, the SE image may be masking the topography through the conductive coating. This being said, it is still apparent that the ESED detector has greater contrast than the other detectors.

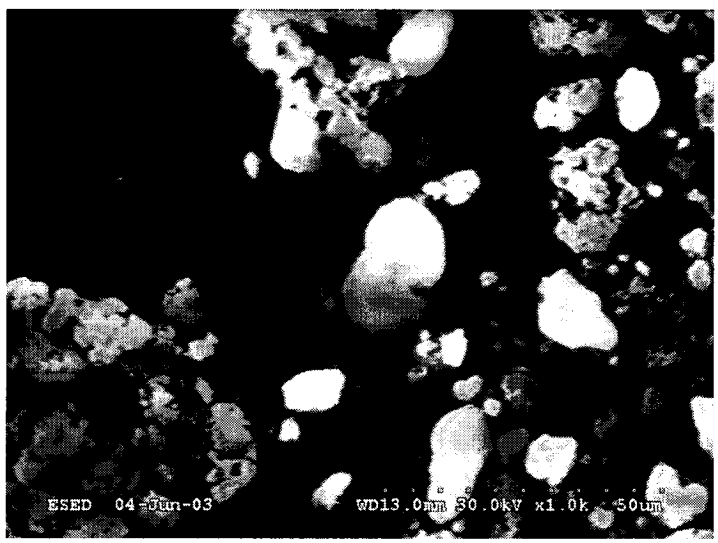

Figure 4.12: Image of nickel hydroxide particles used for measurement of charge contrast.

An ideal situation would be to distinguish between iron and nickel hydroxides based on their brightness, or more to the point, by the degree of charging that they exhibit. In order to do this, individual analysis of hydroxide particles is necessary in order to see the behavior of charging with certain operating conditions.

Figure 4.12 is a low magnification image of the nickel hydroxide particles that have been precipitated through a batch recycle process. The particle in the middle of the image is the one that the CCI experiments were performed on. In order to have good results, the zoom was increased on the particle. Figure 4.13 is a series of images which were used for the CCI linescan analysis.

It can be seen from Fig. 4.14 that higher contrast occurs at higher specimen current. This can be attributed to a higher ion flux allowing optimal charge compensation at the sample surface.

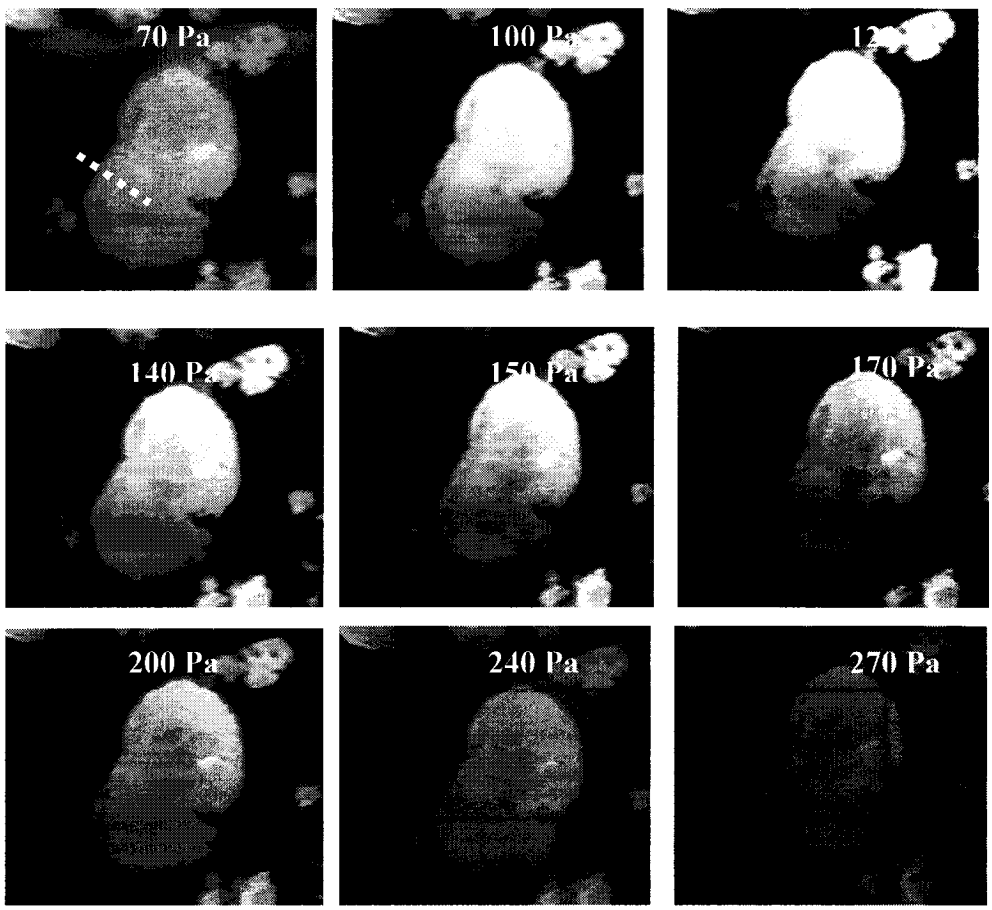

Figure 4.13: Images of nickel hydroxide from Fig. 4.22 at a higher magnification. Linescan taken along the left hand side of the image indicated by the stippled line.

Charge contrast does occur for nickel hydroxide however there are inherent difficulties. The small particle size is a fundamental difficulty associated with this analysis. Smaller sizes mean that higher magnifications are necessary to obtain proper pixel intensity measurements. At higher magnifications, however, charge contrast becomes diminished due to an increase in electron bombardment.

There is an increase in the number electrons penetrating an area of the sample. This increase in electron bombardment increases the overall charging that develops on the sample surface. An increase in overall charging tends to mask the subtle variations in local charging, which ultimately decreases the observable charge contrast.

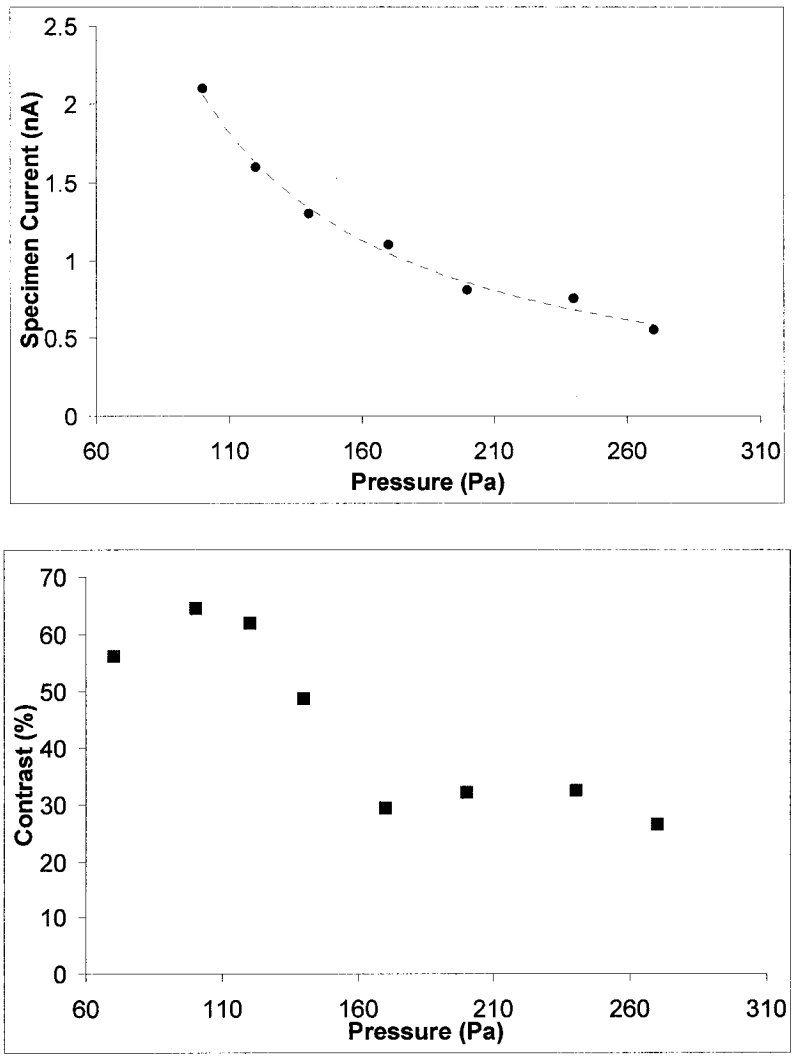

Figure 4.14: Contrast and specimen current measurements as a function of pressure. Increased contrast occurs at higher specimen currents.

CHAPTER 5

ELECTRON SKIRT MODELLING

5.1 Introduction

A complete understanding of the skirt behaviour is paramount in order to perform X-ray microanalysis on the variable pressure SEM. As described in Chapter 2, much work has been performed trying to model this behaviour, including the development of various Monte Carlo simulations. The variables used are gas type, gas pressure, effective gas path length, and accelerating voltage.

This chapter covers the experimental results pertaining to the measurement of skirt radius and percent scattering (fp). A comparison between these experimental results and theoretical results from the Monte Carlo program GAZ, are presented.

5.2 Skirt Radius

An electron colliding with a gas molecule in the sample chamber can be scattered over any angle between 0 and 180 degrees. According to particle interaction theory, the majority of scatter is over a small angle. This average angle of scattering controls how far the electron interacts with the sample outside the target area. A common way of describing the radius is to take the R90 value, which is the radius that includes 90 percent of the incident electrons. This is statistically valid as it eliminates the outliers.

The R90 value is dependant on the gas pressure, the type of gas, gas path length and accelerating voltage. Varying these parameters affects the number of scattered electrons as well as the angle with which they are scattered. This section presents the results for measuring the R90 value described in the experimental section.

The electron beam was scanned across the interface between the copper block and the conductive bakelite over successive pressures. Figure 5.1 is an image of the copper sample with linescans overlayed at 0 pascals and 200 pascals. It can be seen that at increased pressure, copper is detected well before the beam is at the interface.

The resultant linescans were saved as data files to be opened and processed in Excel. Figure 5.2 represents the data at 90 pascals. There is some background noise evident that must be dealt with. The source of this background

Figure 5.1: Comparison of two linecans overlayed on an image of the copper sample. Vertical line is the path that the electron beam followed and the curve is the resultant linescan. Copper is detected only up to the interface at 0 Pa and well before the interface at 90 Pa.

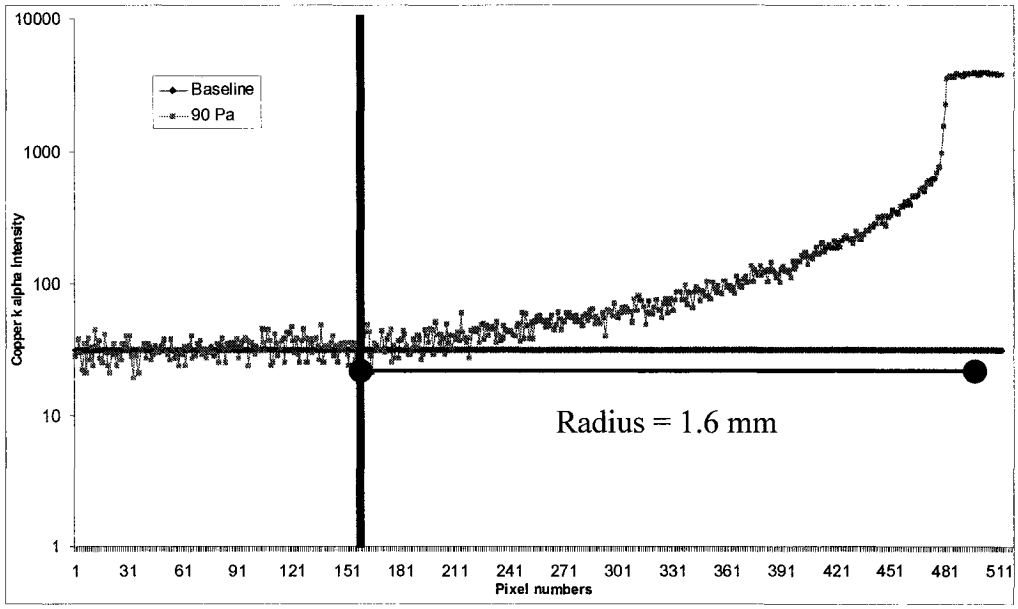

Figure 5.2: Copper k alpha intensity plot as a function of pixel number. Each pixel is equivalent to 4.87 X 10^{-3} mm. The copper interface is at pixel 481 and the intensity begins to deviate from the baseline at pixel 150; therefore the size of the skirt radius is 1.6 mm.

may be the bremmstrahlung as well as spurious signals from brass components in the microscope chamber. An average was taken for this background and called the "baseline". The baseline was overlaid on the figures. The point where the X-ray intensity significantly deviates from the baseline is deemed the distance where the skirt electron first interacts with the copper target. This point of deviation is somewhat subjective; however, taking the R90 values reduces the uncertainty significantly. This experiment was performed 8 times to ensure reproducible results.

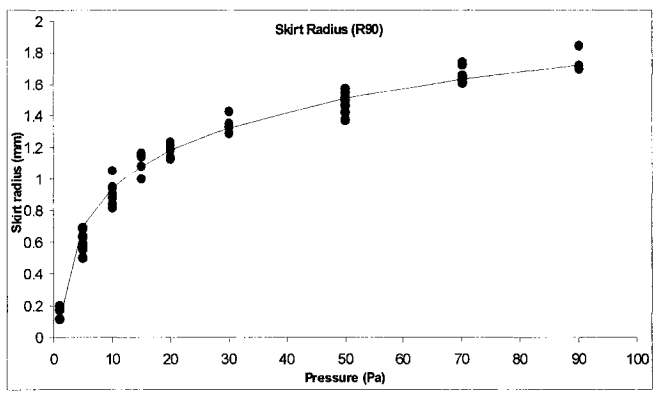

Figure 5.3: Plot of R90 versus pressure. Note the large increase in the radius at low pressures, and that the rate of

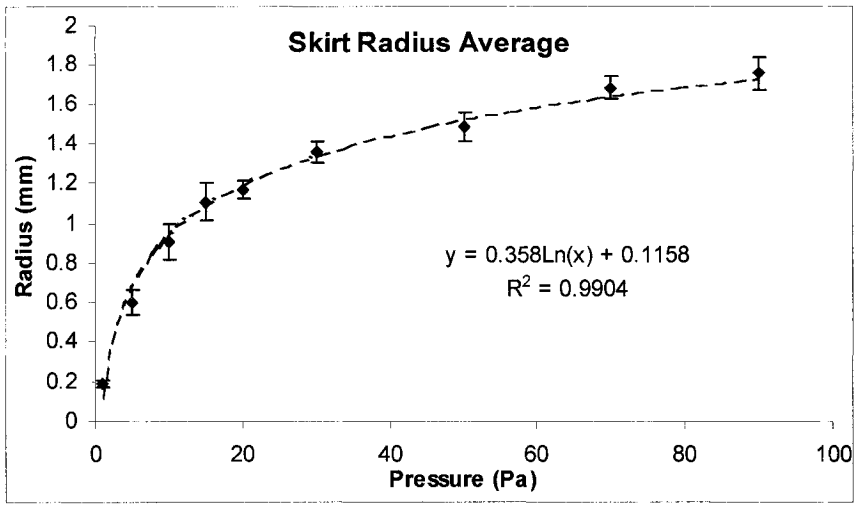

Figure 5.4: Average radius for all the trials follow closely to a logarithmic trendline.

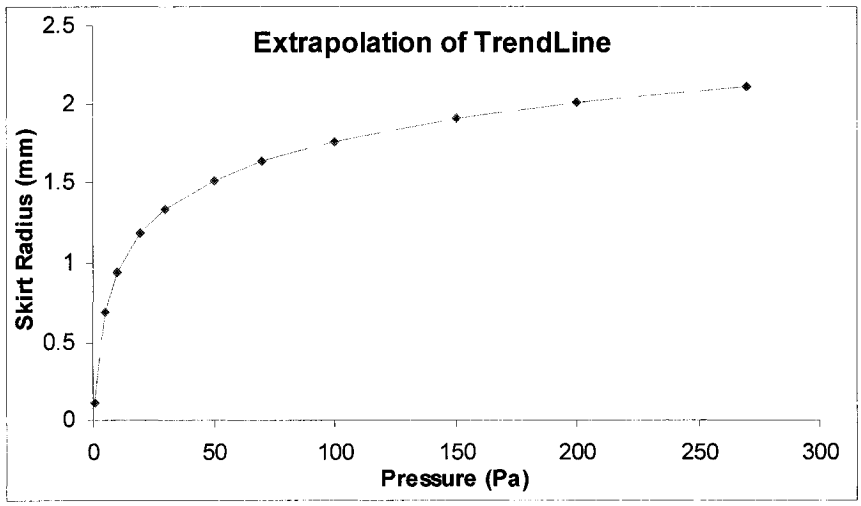

Figure 5.5: Extrapolation of the trendline assigned to the average skirt radius in figure 5.4. At 270 pascals the skirt radius is 2.12 mm.

The results are presented in Figure 5.3. Results are only presented up to 90 pascals because above this pressure the skirt was too large to measure. The field of view at minimum magnification on the microscope covers 2.5 mm. This means that if the skirt is larger than this distance it is not possible to measure. This is the case above 100 Pascals. The average radius for the experimental results, however, follows closely to a logarithmic trendline as seen in Figure 5.4, and extrapolating to the maximum pressure of 270 pascals shows that the skirt radius becomes well over 2 mm.

A skirt of this size is quite problematic when performing X-ray microanalysis. This is where the development of correction models is important, as discussed in chapter 2.

5.3 Percent Scattering

An important aspect in developing a model for scattering is the percent scatter that the beam electrons suffer as they pass through the gas. Gauvin (1999) proposed a technique for correcting the skirt for use in microanalysis. His method is based on a plot of the X-ray intensity as a function of the f_p (non-scattered fraction). Extrapolation to $f_p = 1$ provides the corrected X-ray intensity. It is therefore important to have accurate measurements and/or theoretical calculations of f_p.

The impact of the main parameters which affect f_p, beam energy, gas chamber pressure, effective gas path length and the type of gas, are expressed in equation 5.1 [39]:

$$f_p = e^{-0.035\frac{ZPD}{TE_0}} \qquad [5.1]$$

where, P is pressure, D is the effective gas path length, T is temperature in Kelvin, E_0 is accelerating voltage and Z is the effective atomic number given by equation 5.2:

$$Z = \sum_{j=1}^{m} x_j \sum_{i=1}^{n} n_i Z_i^{4/3} \qquad [5.2]$$

where, m is the number of molecules in the gas chamber, x_j is the molecular fraction of the j^{th} molecule, n_i is the number of atoms in the j^{th} molecule, and Z_i is the atomic number of the i^{th} atom in the j^{th} molecule. For air at 25°C, f_p is given by:

$$f_p = e^{-0.00329\frac{PD}{E_0}} \qquad [5.3]$$

Table 5.1: Experimental values for Cu L alpha intensity and resultant f_p. Ip is the intensity at experimental pressure and Io is the intensity at 0 Pa

Pressure (Pa)	fp(Ip/Io)	Intensity (Ip)
0	1	20095
1	0.96	19314
5	0.89	17866
10	0.81	16247
20	0.72	14370
50	0.51	10204
100	0.27	5479
200	0.09	1734
270	0.04	825

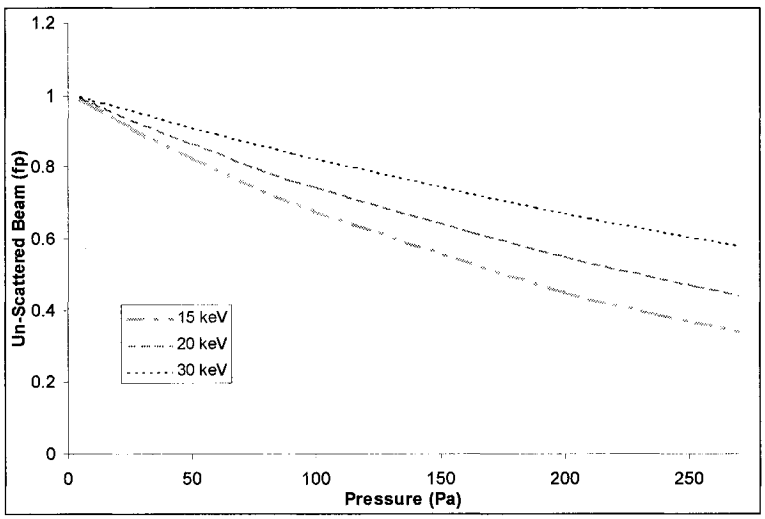

Figure 5.6: Plot of f_p for air computed with Eq. (5.3)

To calibrate the model, f_p must be measured experimentally. A simple experiment, as described in chapter 3, was conducted to measure f_p. The electron is positioned on the target at high vacuum and the characteristic X-ray line was collected (I_o). Pressure was changed and the same characteristic X-ray line was collected (I_p). Percent scattering (f_p) at various pressures is given by the ratio of I_o/I_p as long as scattered electrons do not interact with the target. This is a safe assumption considering that skirt diameters are typically on the order of several mm (Fig. 5.3).

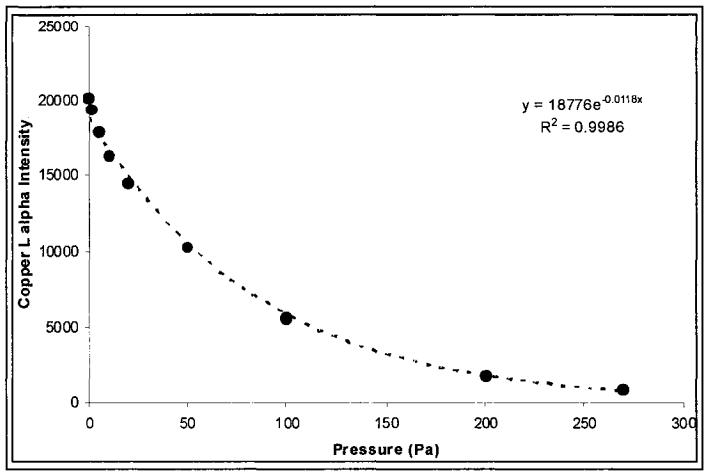

Figure 5.7: X-ray intensity versus pressure at 15 keV. An exponential decay is observed.

Table 5.1 is an example of the experimental copper L alpha X-ray results at an accelerating voltage of 15 keV. As seen in Figure 5.7, plotting intensity versus pressure does not yield a linear relationship. For this reason the pressure variation method as described in section 2.4.5.3 is not valid at elevated pressures. Data from Table 5.1 can be plotted as f_p versus intensity (Figure 5.8) which yields perfect linearity, allowing for the correction procedure as described in section 2.4.5.3. Figure 5.9 shows the experimental results for various accelerating voltages. As can be seen, the scatter significantly increases at lower accelerating voltages. Electrons with low energy tend to be more affected by the gas molecules creating a larger probability of collision.

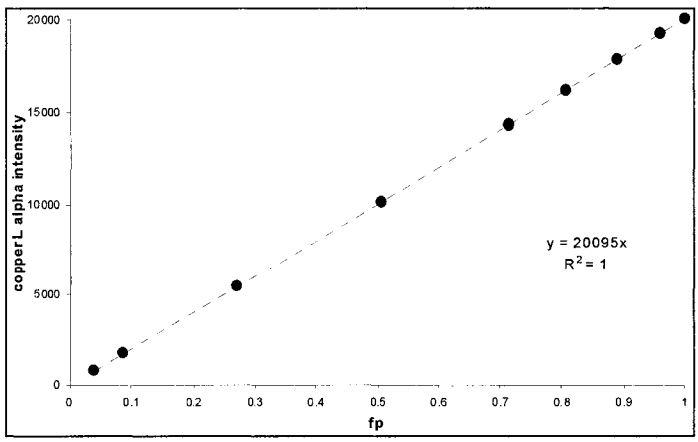

Figure 5.8: Copper L alpha X-ray intensity plotted as a function of f_p. Obtaining X-ray intensity for two pressures allows an extrapolation to $f_p = 1$ for the corrected no skirt net intensity.

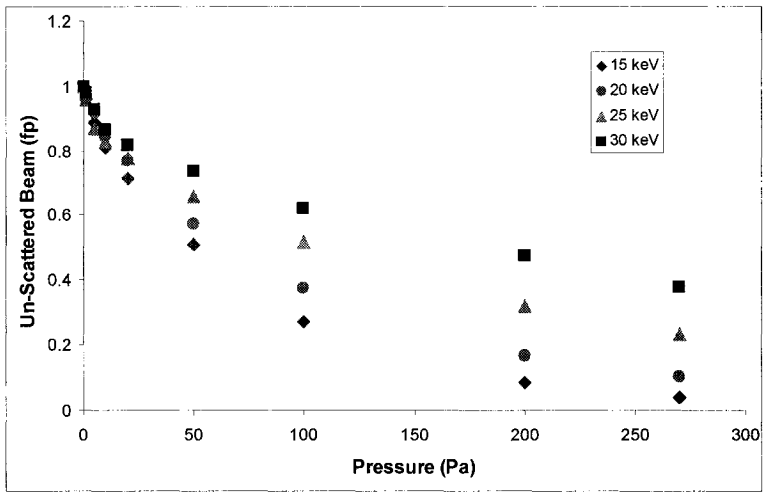

Figure 5.9: Experimental results for various accelerating voltages.

5.4 Monte Carlo – GAZ

GAZ is a program designed by R. Gauvin to model the electron scatter in the variable pressure SEM. It uses Rutherford cross-sections as a means of calculating the probability of collision. A windows interface is still in the development stages; however, results are obtainable.

Four variables are controlled in the model software. Gas pressure, gas type, gas path length and accelerating voltage can be set by the user as well as the number of electrons. The results are saved as text files which must be opened in Excel. It is important to be able to test experimentally the validity of these theoretical results.

5.4.1 Skirt Radius

Figure 5.10 provides a comparison between the theoretical and experimental results for the skirt radius. As noted, the theoretical model underestimates the radius. This may be due to the use of the Rutherford cross-sections in the model. The angles of collision may be improperly calculated which results in a deviation in the observed radius. Another discrepancy between the results may be in part due to the contribution of inelastic collisions. GAZ does not include this contribution, therefore, the overall scattering event is less than in the experimental.

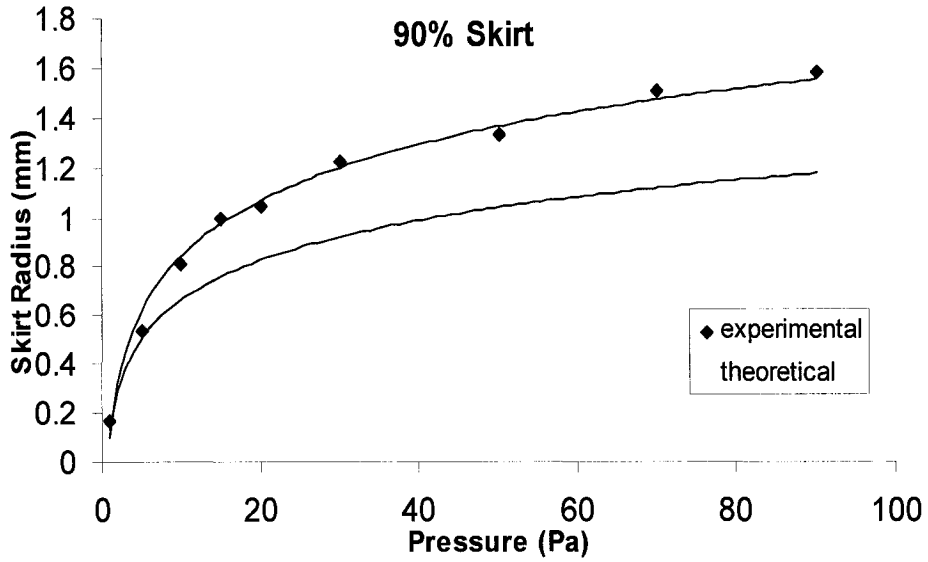

Figure 5.10: Comparison between experimental and theoretical value for skirt radius. Theoretical underestimates the size of the skirt.

5.4.2 Percent Scattering (f_p)

Considering that the theoretical radius is smaller than the experimental, one might assume that the number of scattering events is less. This corresponds to a higher theoretical fp. It appears that the experimental results consistently have increased scattering (lower f_p), as seen is Figure 5.11. Also evident is that the discrepancy between theory and experiment lessens at low pressures and high accelerating voltages (Fig. 5.12). Therefore there appears to be some consistency in the under-representation of scattering in the theoretical model.

Before it is possible to determine the cause of this discrepancy, one must examine the controlling variables. As mentioned, the factors which determine f_p are pressure, type of gas, accelerating voltage and effective gas path length and the theoretical cross-section. Therefore, the answer should lie with one of these variables.

The VP-SEM uses a pirani gauge as a means of maintaining a specific pressure in the sample chamber. A needle valve is used which maintains a pressure relatively close to what is desired. He and Joy (2003) show that the precision of this system should avoid discrepancies between theory and experiment.

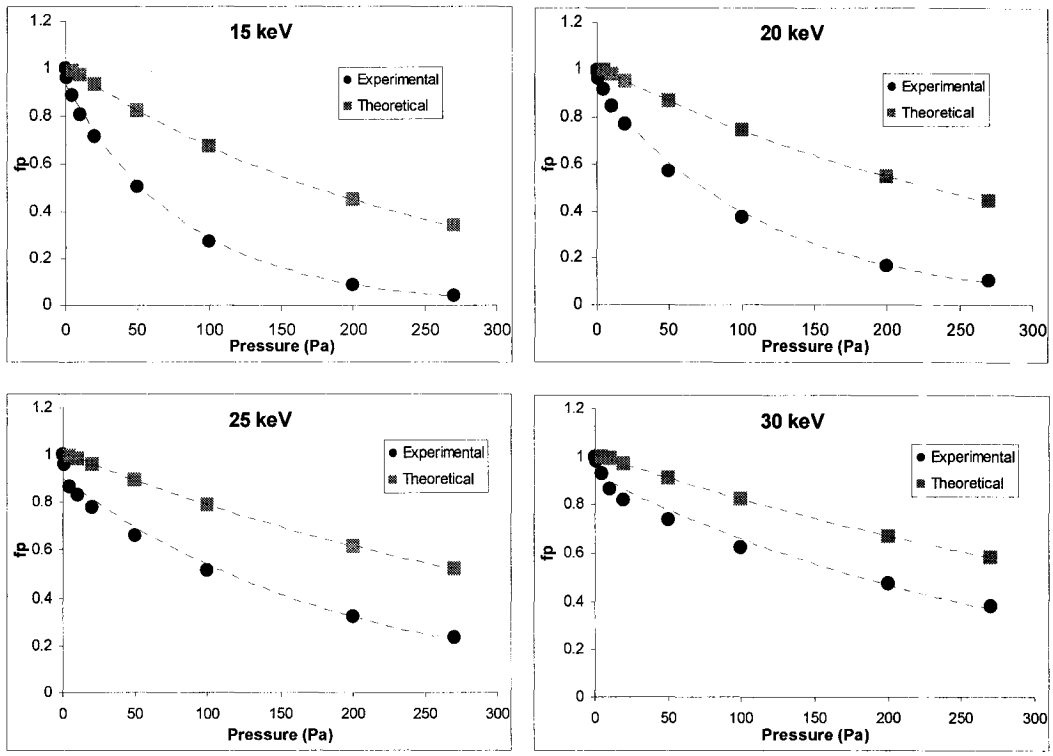

Figure 5.11: Comparison between experimental and theoretical fp for various accelerating voltages.

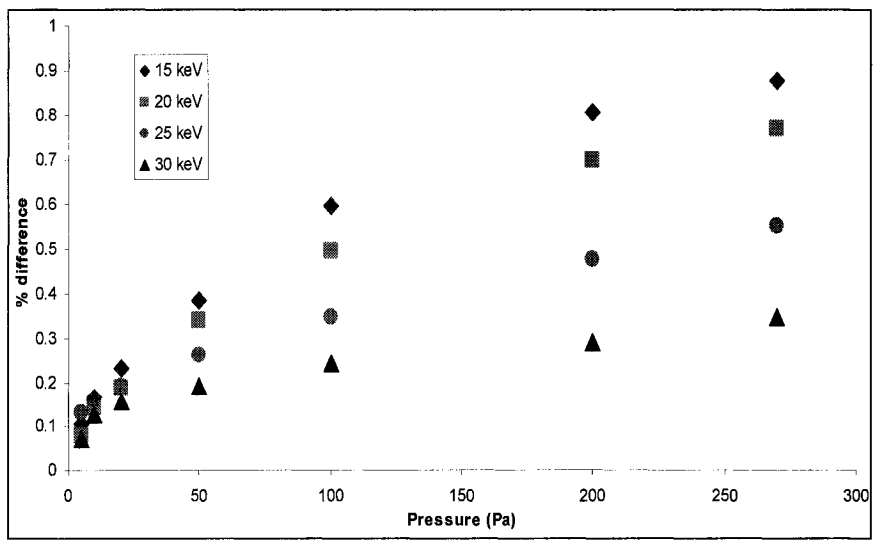

Figure 5.12: Difference between the experimental and theoretical results. Difference increases at high pressures and low accelerating voltages.

The type of gas could introduce some discrepancies, due to the values of the cross-sections being used. Using an erroneous cross-section can produce wrong f_p values in the theoretical model. At this point Rutherford cross-sections are the most accurate available. Recently, He and Joy (2003) have shown that it is possible to calculate the cross-sections, as described in section 2.5.4.3.

Another problem could arise from using an improper gas-path-length in the model. The GPL is the distance traveled by the electron through the gaseous medium. The pressure limiting apertures at the pole piece are often over 100 μm in size. Gas molecules can occasionally bleed through the aperture, creating a larger GPL than expected. This affects the percent scatter as well as the radius of scatter. If the GPL is several mm longer than what is inputted into GAZ, the skirt radius tends to be underestimated. This potentially explains the discrepancy between theoretical and experimental skirt radius values.

Equation 5.3 can be re-written to back-calculate the GPL (D) from the measured f_p, namely equation 5.4:

$$D = \frac{-303.95 E_0 \ln f_p}{P} \qquad [5.4]$$

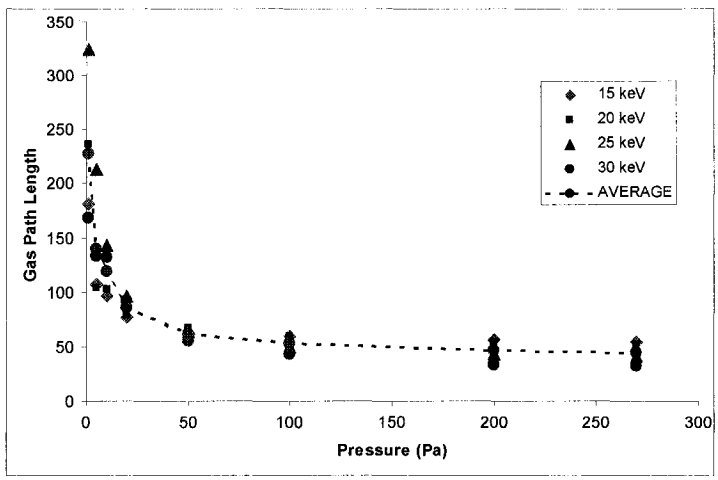

Figure 5.13: Calculated GPL from the experimental f_p values. The trend is not expected: There is a rapid decrease in GPL with a plateau at 50 mm; not only should the behaviour be reversed but the plateau is 35 mm greater than expected.

The results for the GPL were not expected (Fig. 5.13). Instead of increasing with pressure, the GPL decreases. At 100 Pa there is a plateau at around 50 mm. This is quite high when considering that the GPL for this microscope is quoted to be 15 mm. The error can be attributed to either the accelerating voltage or the measured f_p.

The sample is coated with gold-palladium; however, there still exists the possibility of sub-surface charging. If this charging occurs, the electron energy of the primary electrons would decrease, creating a large source for error in the experimental results. Figure 5.14 gives an indication that sub-surface charging is occurring. Plotting log intensity versus pressure should be log linear; however, we see that as pressure decreases, the rate of increase in intensity decreases. This hints that sub-surface charging is occurring which slows down the primary electrons, decreasing the X-ray emission intensity. Extrapolating to zero pressure using a linearized section over the high pressure region should produce a more accurate result.

Figure 5.15 is log intensity as a function of pressure. Trend lines have been added to extrapolate to the intensity at 0 Pa. Corrected f_p values were calculated by dividing the intensity into the corrected intensity at 0 Pa. This should yield appropriate results for pressure above 100 Pa because we assume that there is no charging above this pressure.

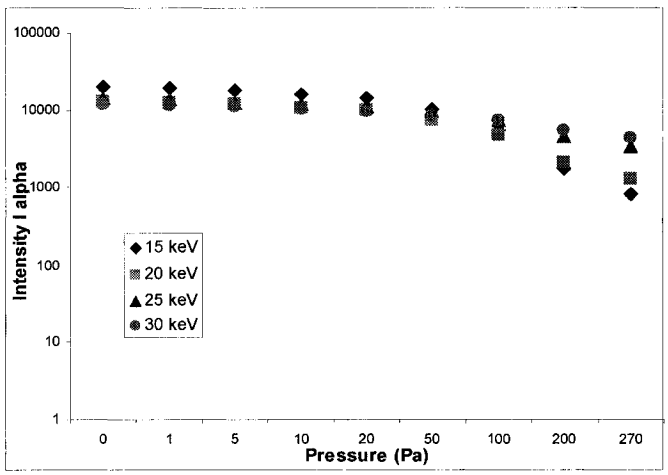

Figure 5.14: Log of Copper L alpha Intensity as a function of pressure. It is seen that the plot deviates from linear around 50 Pa. This deviation indicates that some sub-surface charging occurs.

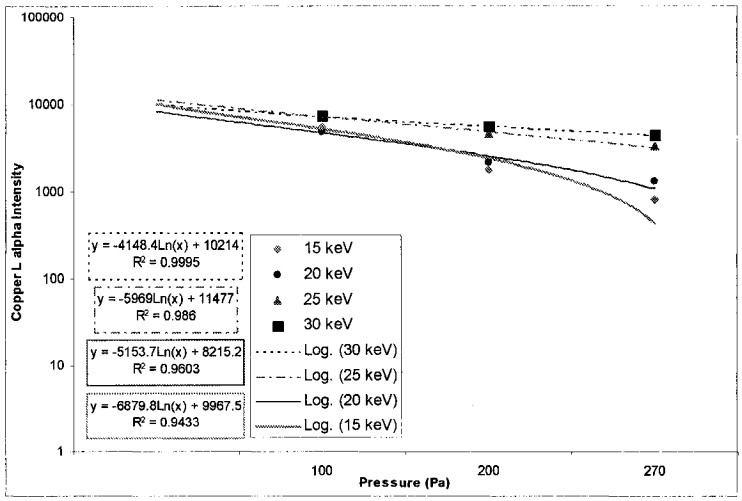

Figure 5.15: Plot of log intensity vs Pressure. Extrapolating along trendlines to a pressure of 0 Pa should yield the true copper intensity without the effect of charging.

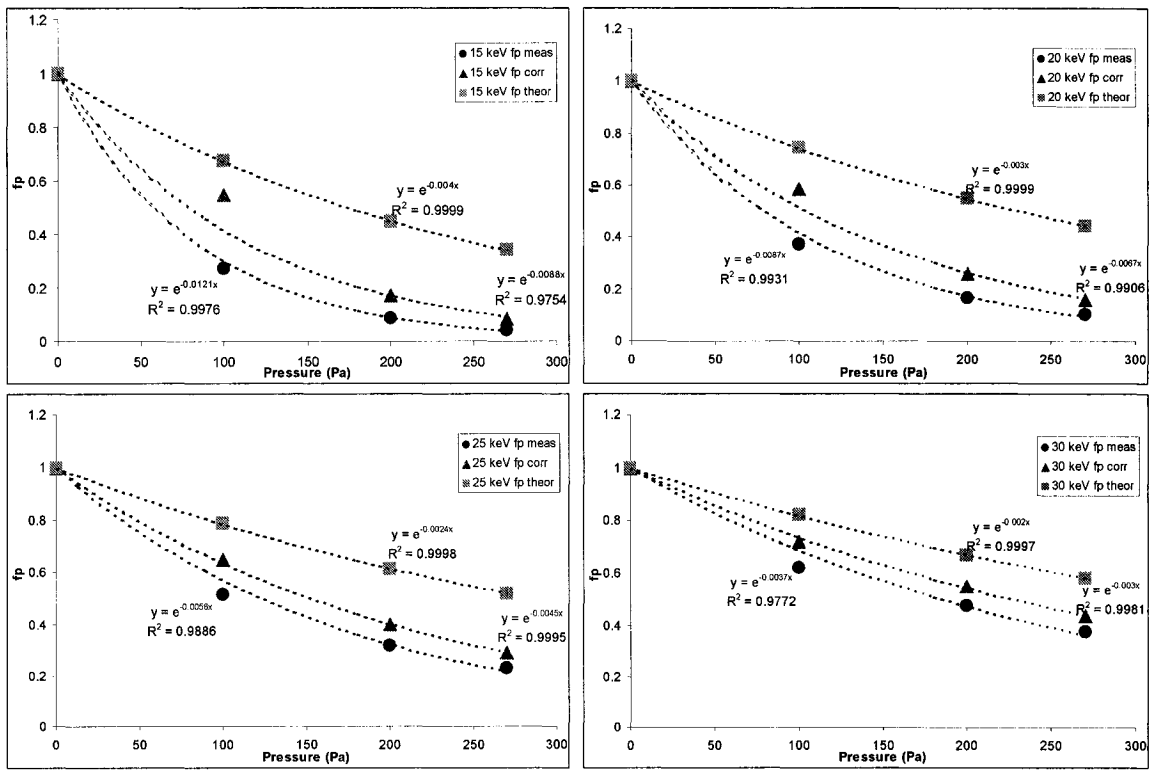

Figure 5.16: Comparison of theoretical, measured and corrected fp results. There is a minor improvement however the difference is still quite large. The conclusion is that there is a problem with charging of the sample or the Rutherford cross-section is incorrect.

Figure 5.16 is a comparison of the measured f_p, corrected f_p and theoretical f_p values. It is observed that there is an increase in the f_p values, however they are still notably lower than the theoretical values. We see that even with a correction for the charging, the theoretical model still underestimates the degree of scatter in the chamber.

The reason for this discrepancy may be due in part by problems associated with using Rutherford cross-sections. It may also be caused by an increase in inelastic scattering at low pressures and accelerating voltages. He and Joy (2003) show that calculating cross-sections for molecular gas is not as simple as the sum of the atomic cross-sections.

He and Joy (2003) proposed a method for experimentally measuring the cross-section using Eqs. 2.11 and 2.12. Using this cross-section, the corresponding f_p values were calculated using Eq. 2.20. Fig. 5.17 shows that the fp values are more comparable to the experimentally measured f_p values. It is evident that Rutherford cross-sections may not be appropriate for modelling the skirt behaviour.

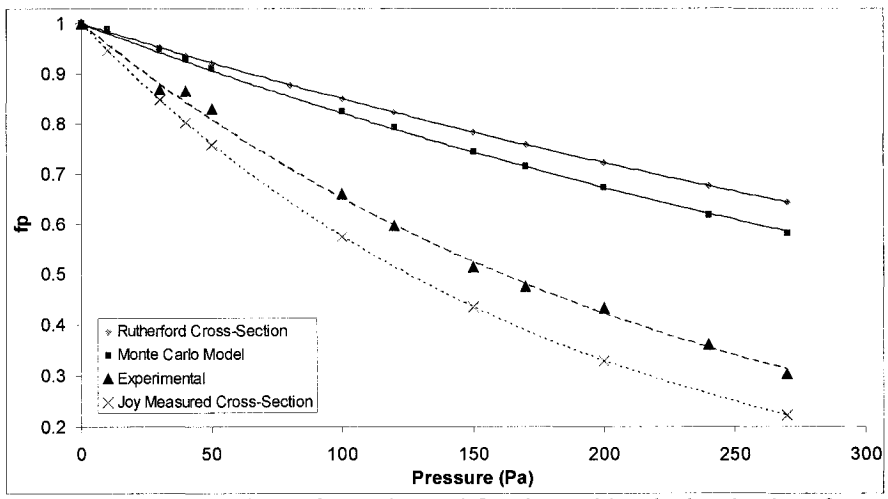

Figure 5.17: Comparison of experimental f_p values with calculated values from Rutherford, Monte Carlo and Joy cross-sections. Using the Cross-sections established from joy provided more consistent results with the experimental value.

Calculation of the cross-section form corrected and uncorrected f_p values were performed with Eq. 2.20. The experimental uncorrected values gave a cross-section of 2.6E-17 cm^2/atom while the corrected value was 5.67E-18 cm^2/atom. The values for the uncorrected cross-section are similar to that of the values obtained from He and Joy (2003). The corrected cross-section was much smaller than expected however. From these results it indicates that the sample charging is not a great source of error, whereas the use of the Rutherford cross-section is.

At low pressures and low accelerating voltages, inelastic scattering dominates, which is not accounted for. Atomic clustering is also not included in the model which can provide a source for error. Another problem associate with this technique is the value used for GPL. For all modelling, a GPL of 15 mm was used which is the effective working distance. The actual value is most likely larger than this, however, attempts to calculate the GPL were unsuccessful.

In order to resolve, more effort must be made in determining when charging no longer exists on the sample. It is also beneficial to use a sample that is more dedicated to this type of fundamental analysis. Gauvin et al. (2002) describe a process whereby aluminium is precipitated onto a conductive material of different composition. This method eliminates the problem of charging as well as the possibility of skirt electrons detecting the target element. Samples of this type seem more appropriate to perform fundamental experiments. Once the f_p is known to be accurate, various correction techniques can be applied to non-conductive materials.

CHAPTER 6

NICKEL SLUDGE ANALYSIS

6.1 Introduction

This chapter presents the results for the analysis of the nickel sludge sampled from the INCO operation in Sudbury, Ontario. There are two sections, general sludge analysis using imaging techniques and X-ray microanalysis, and one on the results of progressive leaching of sludge. It appears that nickel is not only present as hydroxides in the AMD treatment sludge. Nickel exists as sulfide and oxide material which is more resistant to leaching. Further, nickel appears to complex with aluminum, silicon and sulfur as colloidal size material which also is resistant to leaching. In order to have complete nickel extraction, these materials must be targeted.

6.2 X-Ray Microanalysis of Hydroxide Sludge

There are three main components to the fresh AMD treatment sludge from INCO. The first comprises the neutralization products, the metal hydroxides and gypsum. These are generally colloidal in nature. These products are important because they contain a large portion of the nickel. The second component is detrital material occurring as inclusions in the dried sludge particles. This material is most likely picked up from the river bed as well as the tailings impoundment. The third component is the liquid, which contains dissolved calcium ($CaCO_3$) and ($CaSO_4$) and unreacted lime (CaO). Drying leaves a layer of precipitated calcium on the surface of the dried sludge.

The component of main interest is the neutralization products because this is representative of the lime treatment process where the soluble metals are reacted to form hydroxides.

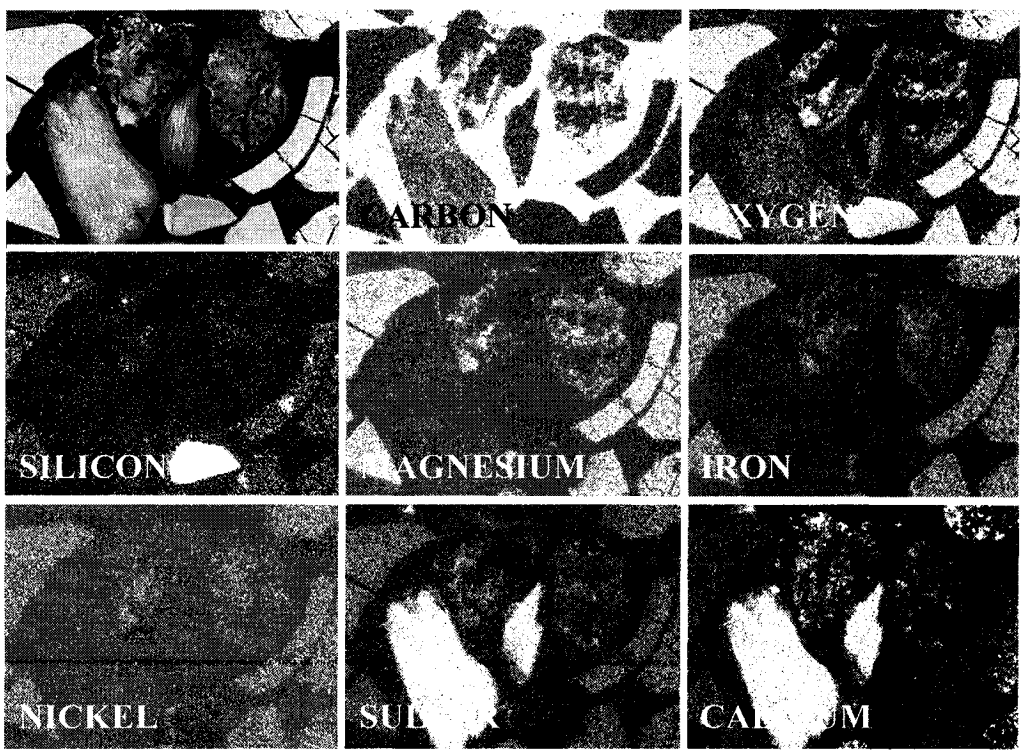

Figure 6.1: X-ray map of a group of particles in the air dried sludge. It shows the three different components present in sludge: The neutralization products, gypsum and Mg, Fe, and Ni hydroxides; the detrital inclusions, seen in the Si map; and the dried liquid component, identified by the cluster of calcium bearing particles.

Figure 6.1 is an X-ray map of a group of particles in the air dried sludge. This image shows quite clearly the three components. Among the neutralization products, the gypsum is identified by the sulfur and calcium in the X-ray maps, while the hydroxides include magnesium, iron and nickel. One type of detrital inclusion is a silicate, seen in the Si and O maps, and the cluster of calcium bearing particles in the Ca and O maps is representative of the dried liquid. This use of X-ray maps with the VP-SEM is very informative, enabling different particles to be readily identified. Once a particle has been identified at low magnification, further analysis can be performed at a higher magnification. This approach was used for most of the analysis on the sludge because the skirt effect. For this reason, only a qualitative analysis is presented in this section.

6.2.1 Analysis of Detrital Material

As shown in Figs. 6.2 and 6.3, the detrital material is easily identified in optical as well as using electron microscopy. This material appears as large inclusions in the matrix. Figure 6.2 is a series of images taken on the optical microscope which clearly show the inclusions. They have a crystalline morphology that suggests they are not part of the neutralization process. Their size is also an indication, considering that at this operation, a basic lime treatment is used, with little control over the neutralization making it unlikely that such large crystalline materials could be precipitated.

Figure 6.3 is a high and low magnification image of a sludge particle on the VP-SEM. The presence of these detrital materials as inclusions in the matrix is quite obvious. In order to perform an analysis on this material, physical

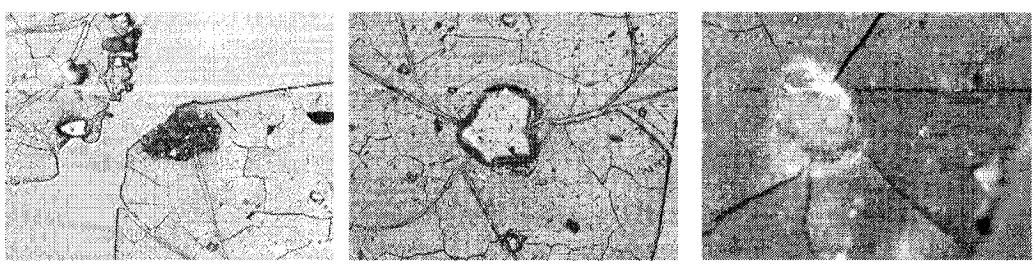

Figure 6.2: Optical microscopy images of the hydroxide sludge and inclusions. Inclusions are large and crystalline in comparison to the amorphous hydroxide matrix.

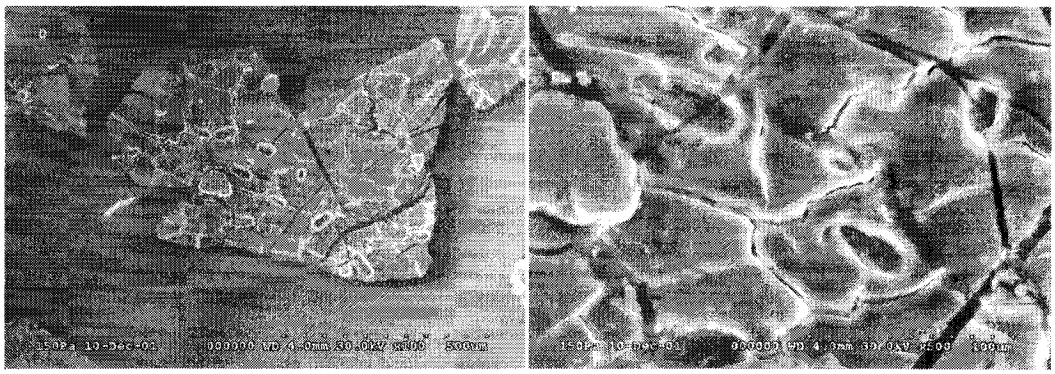

Figure 6.3: High and low magnification of a sludge particle. Inclusions are quite prominent as well as the development of charge contrast which allows differentiation between hydroxide particles.

separation was first necessary. Segregation of these larger particles from the hydroxide sludge was easily performed with a centrifuge. Removal of the slimy hydroxide sludge leaves the inclusions behind for easy analysis.

Figure 6.4 is an example of the types of particles present as the detrital material in the hydroxide sludge. The particles have been numbered one to nine. The associated X-ray maps are presented in Appendix C. Table 6.1 is a list of the particles in Fig. 6.4 with their associated elements and the most likely mineral suggested. It can be seen that the majority of these particles are silicates and clays with some sulfides and oxides. The complete list of all the particles analyzed along with their associated X-ray maps are included in Appendix C.

Table 6.1: List of particles in Figure 6.4. with associated elements and most likely mineral group

	Associated Elements	Mineral Group
Particle 1	Si,O	Quartz
Particle 2	Fe,S	Pyrrhotite
Particle 3	Si,Na,Ca,Al,O	Phyllosilicate
Particle 4	Si,Fe,Al,O	Phyllosilicate
Particle 5	Si,K,Ca,Al,O	Phyllosilicate
Particle 6	Fe,Ni,Al,Mg,S,O	Phyllosilicate
Particle 7	Si,Mg,Ca,Fe,Al,O	Phyllosilicate
Particle 8	Si,Al,O	Phyllosilicate
Particle 9	Cu,Na,O	

Figure 6.4: Image of detrital material segregated from the neutralization products. The numbers denote specific minerals found in the sludge. 1- SiO 2-FeS 3-SiNaCaAlO 4-SiFeAlO 5-SiKCaAlO 6-FeNiAlMgSO 7-SiMgCaFeAlO 8-SiNaAlO 9-CuNaO. These are the elements present in these particles as shown by the X-ray maps in Appendix C.

It can be inferred from the size, morphology and the mineralogy of these particles that they likely derive from the river bed. Ranging from 10 μm to over 100 μm, the particles are too large to have been formed in an uncontrolled neutralization process. The morphology appears crystalline as seen from the optical images, which again is unlikely through an uncontrolled neutralization reaction. Finally, the elemental composition is indicative of volcanic material that has been weathered into smaller sedimentary particles. The river bed is the probable source of this detrital material given the flowsheet (Fig. 3.1).

6.2.2 Analysis of Liquid

Lime neutralization at the INCO operation involves a substantial quantity of lime, added to ensure the pH is high enough to precipitate all the metals. This results in excess unreacted lime as well as solubilized Ca creating a calcium rich liquid.

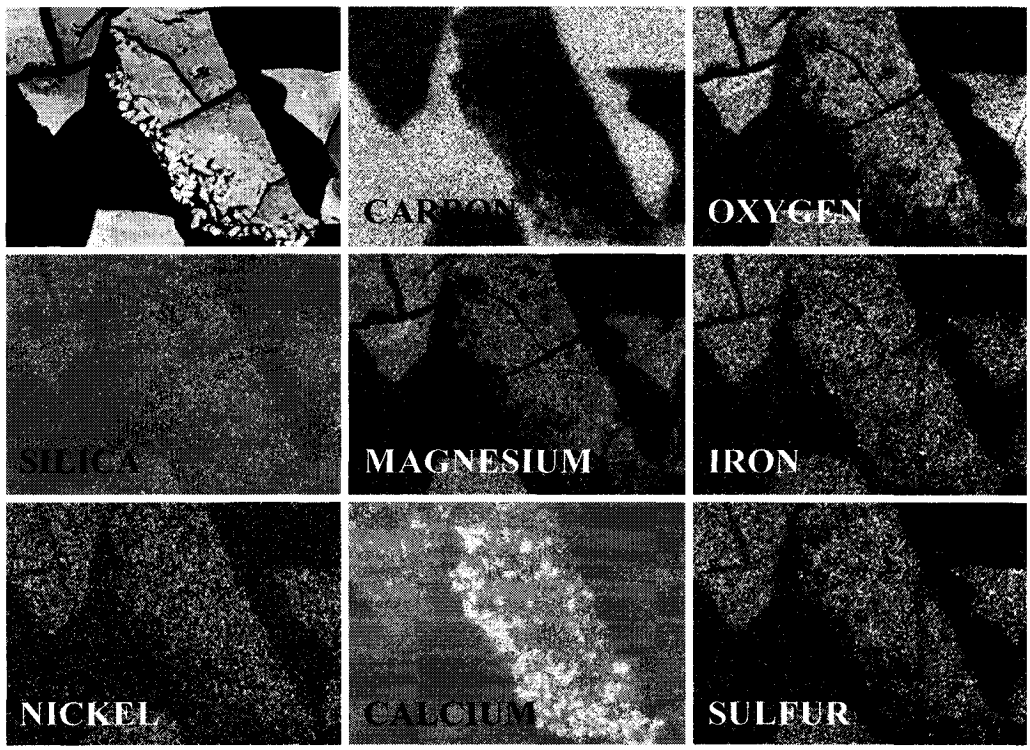

Figure 6.5: X-ray map of the 'calcium crust' that has precipitated on a hydroxide sludge particle. The crust consists of small oval shaped particles which are clearly composed of calcium.

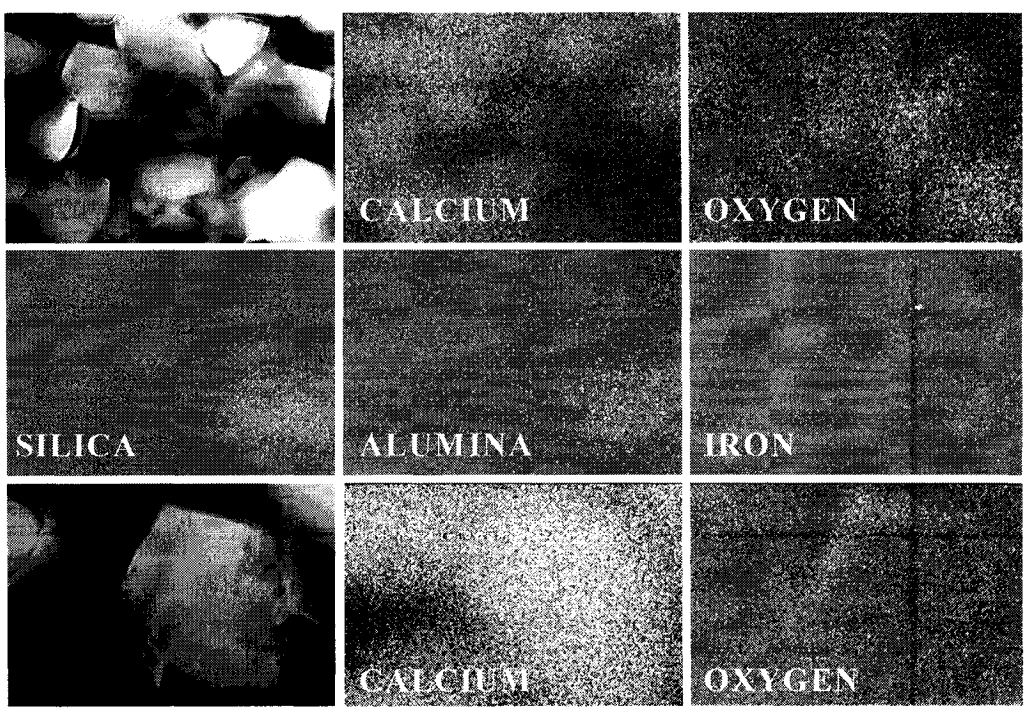

Figure 6.6: X-ray map of the particles precipitated from the liquid separately from the hydroxide sludge at low and high magnification, they clearly contain calcium.

The drying process in sample preparation precipitates the calcium in the liquid. Precipitation occurs primarily as crust, however there also exist minor amounts in the neutralization matrix. Figure 6.5 is an image (upper left) and X-ray map of a sludge particle with a calcium crust down the left side. The crust is seen as small oval shaped particles along the edge of the sludge particle. The X-ray map shows that these particles are made of calcium and oxygen suggesting calcium carbonate (or calcium oxide).

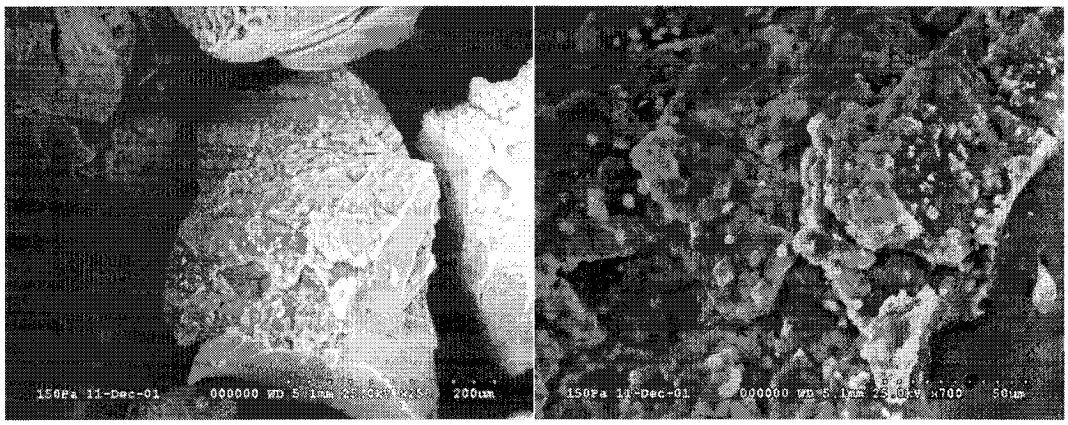

Figure 6.7: SEM micrograph of a hydroxide particle at two different magnifications. There appears to be crust of precipitate on the surface of the hydroxide aggregate, X-ray analysis indicates that this is calcium bearing.

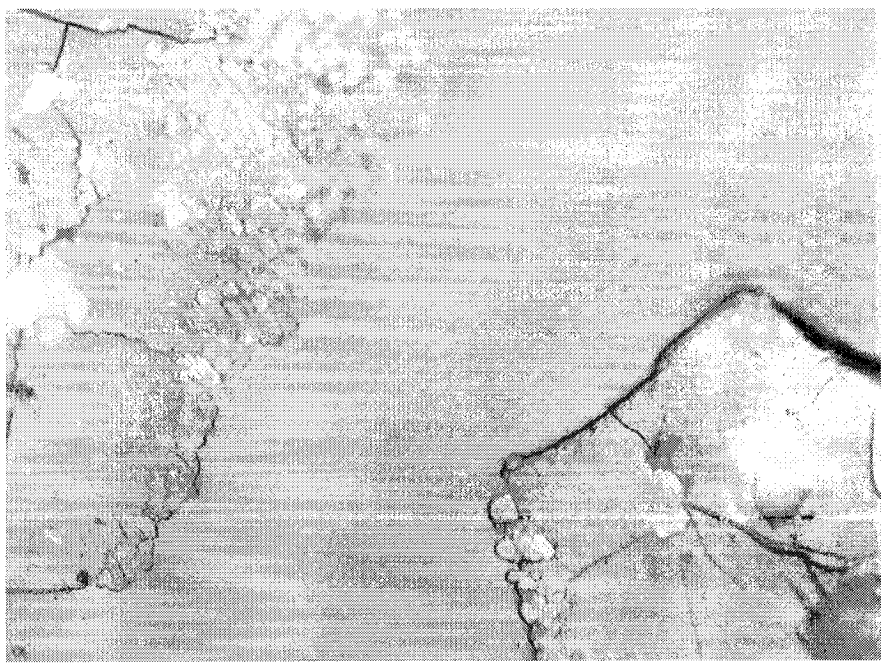

Figure 6.8: Image of the hydroxide matrix with the calcium carbonate particles along the edge. The calcium in the water coats these hydroxide aggregates upon drying. The calcium particles are also found sporadically throughout the hydroxide matrix.

Figure 6.6 is an X-ray map for calcium-bearing particles precipitated separately from the hydroxide sludge. This sample only consists of the calcium bearing material because it was precipitated separately from the sludge. The particles are hexagonal in shape and appear to have some oxygen present as well, supportive of calcium carbonate ($CaCO_3$). The X-ray maps do not show any sulfur present. These particles are not important in terms of the mineralogy associated with the nickel; however, it is important to identify these particles to aid in the interpretation of the components.

The precipitation of the calcium coats the sludge particles creating a crust of calcium carbonate/oxide as seen in Fig. 6.7. The first image was taken at a magnification of 250 X and the crust is clearly observable. The second image was taken at a higher magnification to emphasis that the crust is composed of individual particles which have aggregated.

Figure 6.8 is an image taken with an optical microscope. The sample imaged is a polished mount containing sludge particles with the 'calcium crust'. These particles, when polished, show cross-sections which is why the crust appears along the edges. The optical microscope was useful for imaging this crust because calcium carbonate appears translucent compared to the opaque hydroxide sludge. It was quite easy to determine that this was derived from solution and was not detrital material.

6.2.3 Analysis of Neutralization Products

The neutralization products consist of gypsum and colloidal sized metal hydroxides. The gypsum particles tend to be 50-100 μm. It appears that minor amounts of nickel can become incorporated into the gypsum, as seen in Fig, 6.9. Figure 6.10 is a gypsum map where no nickel (or iron) could be detected. It was observed that the majority of the gypsum analyzed did not contain any nickel, and those that did, had concentrations that were not significant. A safe assumption derived from the analysis is that nickel does not occur in the gypsum to any material extent.

The metal hydroxide matrix is the most important component of the sludge in terms of locating the nickel. Figure 6.11 is an X-ray map of the sludge sample. This large particle consists of detrital material as well as the metal

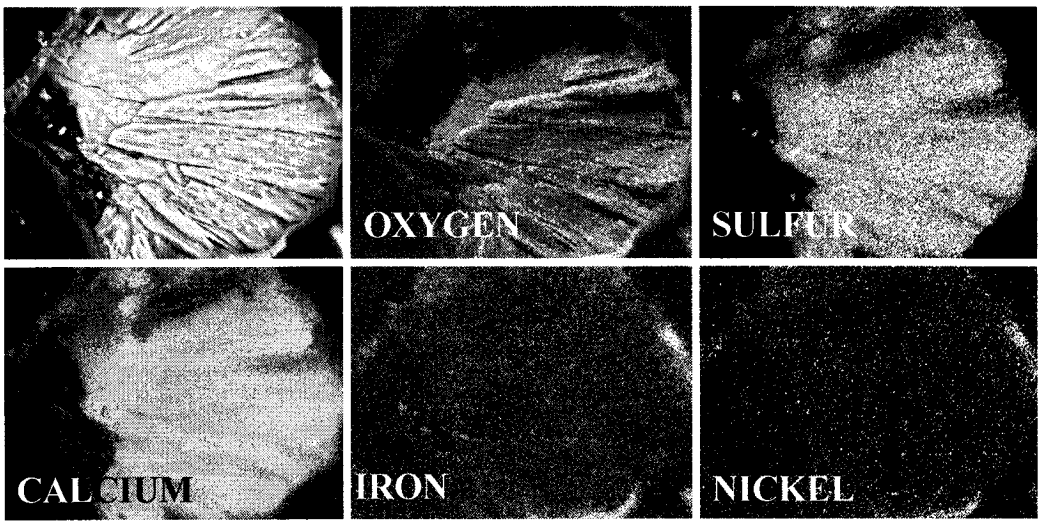

Figure 6.9: X-ray map of a gypsum particle with iron and nickel present as impurities.

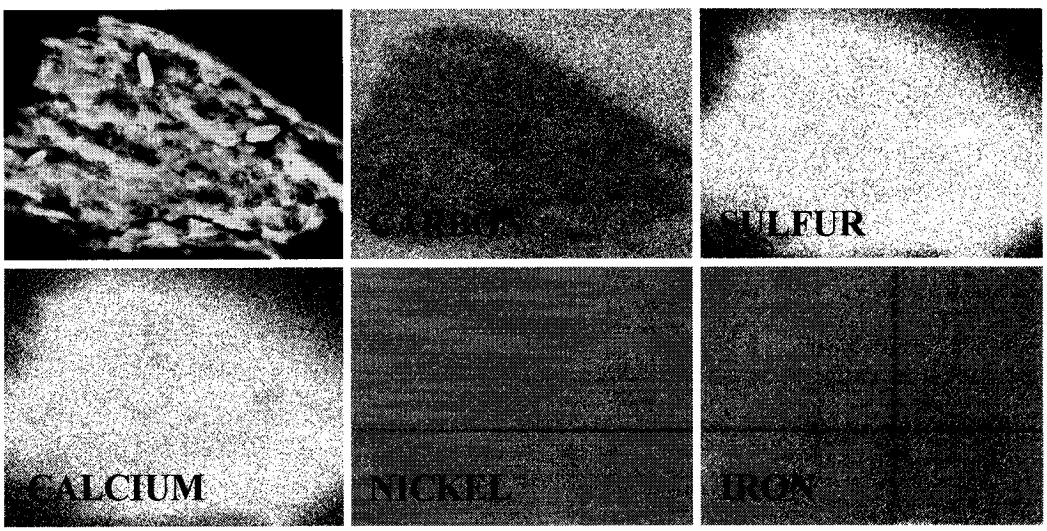

Figure 6.10: Example of a gypsum particle with no iron or nickel.

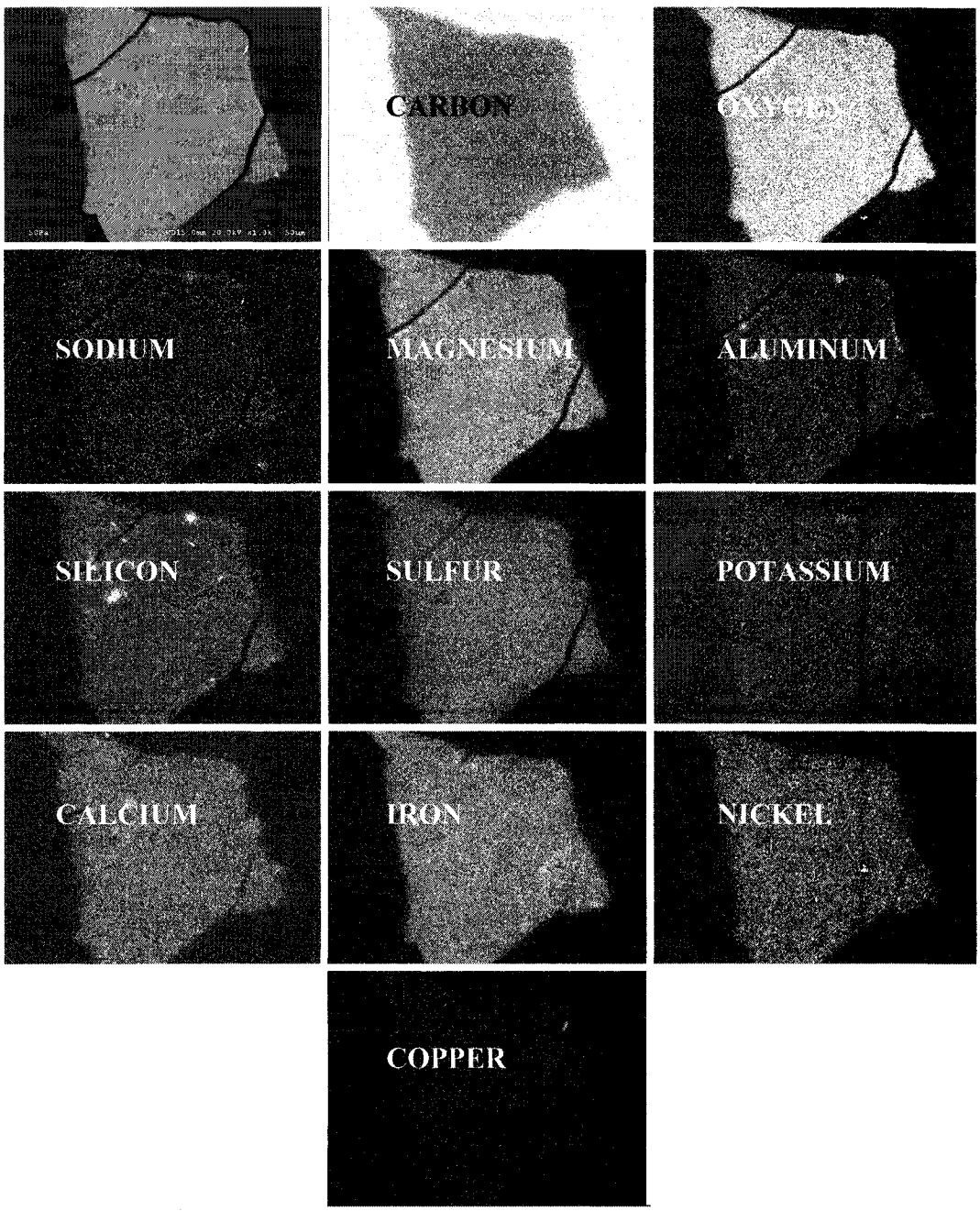

Figure 6.11: Complete X-ray maps for a hydroxide sludge particle. All elements are present. The maps clearly show that the hydroxide "matrix" is more complex than simply containing metal hydroxides. Along with Fe, Mg, Ni and Cu, there are large quantities of Si, Al, S and Ca. This indicates that there are other colloidal sized materials in the "matrix".

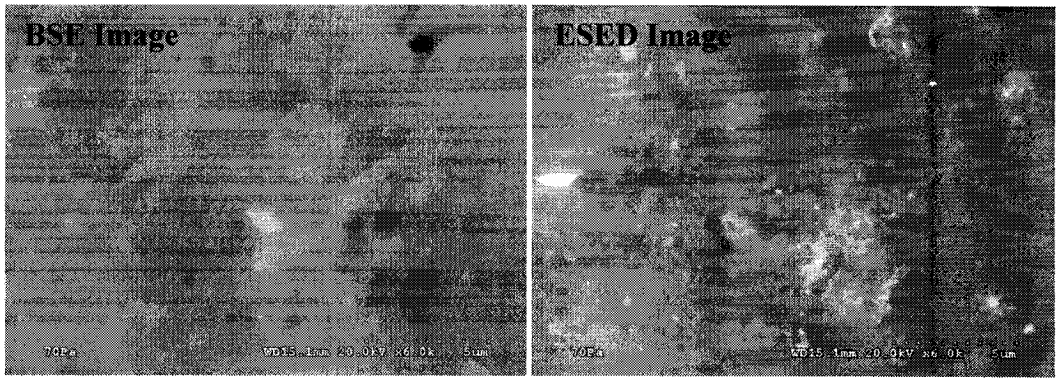

Figure 6.12: Comparison of BSE and ESED detectors of the hydroxide matrix at a higher magnification. The ESED image clearly shows greater contrast. Isolated particles can be distinguished from the background. It is still speculation, however, as to whether this is charge contrast.

hydroxide matrix. The matrix, as shown by the maps, is evidently more complicated than an aggregation of sub- micron sized metal hydroxides. Along with the Fe, Mg, Ni and Cu, is the presence of large quantities of Si, Al, Ca, and S. These phases are also sub-micron in size because regular imaging cannot locate the grain boundaries.

The matrix is assumed to be an aggregate of the metal hydroxides and other sub-micron particles. However, according to the low magnification X-ray maps, the matrix appears to be quite homogeneous. For this reason, higher magnification X-ray maps are desirable to try to differentiate among these colloidal sized particles. Using the techniques described in chapter 4, a high magnification image of the sludge matrix was taken with the BSE detector and ESED detector, in order to use charge contrast as a means of distinguishing the grain boundaries. An X-ray map of the same area was taken to see if the grain boundaries matched the boundaries from the maps.

Figure 6.12 is a comparison of the two detectors. The same high magnification region is depicted in both images. The ESED image clearly shows greater contrast than the BSE image. There appear to be isolated particles segregated from the background. This may be due to the charge contrast, but further studies must be made to confirm this.

An X-ray map of the same area was taken in order to establish boundaries between Ni and Fe particles in the matrix and to see if they matched the boundaries indicated by the ESED image. Figure 6.13 is the associated X-ray map for this area of the sludge particle. For this specific map, six million counts were accumulated to ensure there was enough signal for particle differentiation. The results were not conclusive. It can be seen in the map that there is some variation in the distribution of the elements but no easy match to grain boundaries was found.

Specifically, Fe, Ca and S appear to be enriched in the same location indicating the presence of a particle, as marked by the circle in Fig. 6.13. The stippled circle shows that there is a deficiency of Mg and Ni in this area, which corresponds with a particle in the original ESED image. A region enriched in Si is located to the right of the original particle.

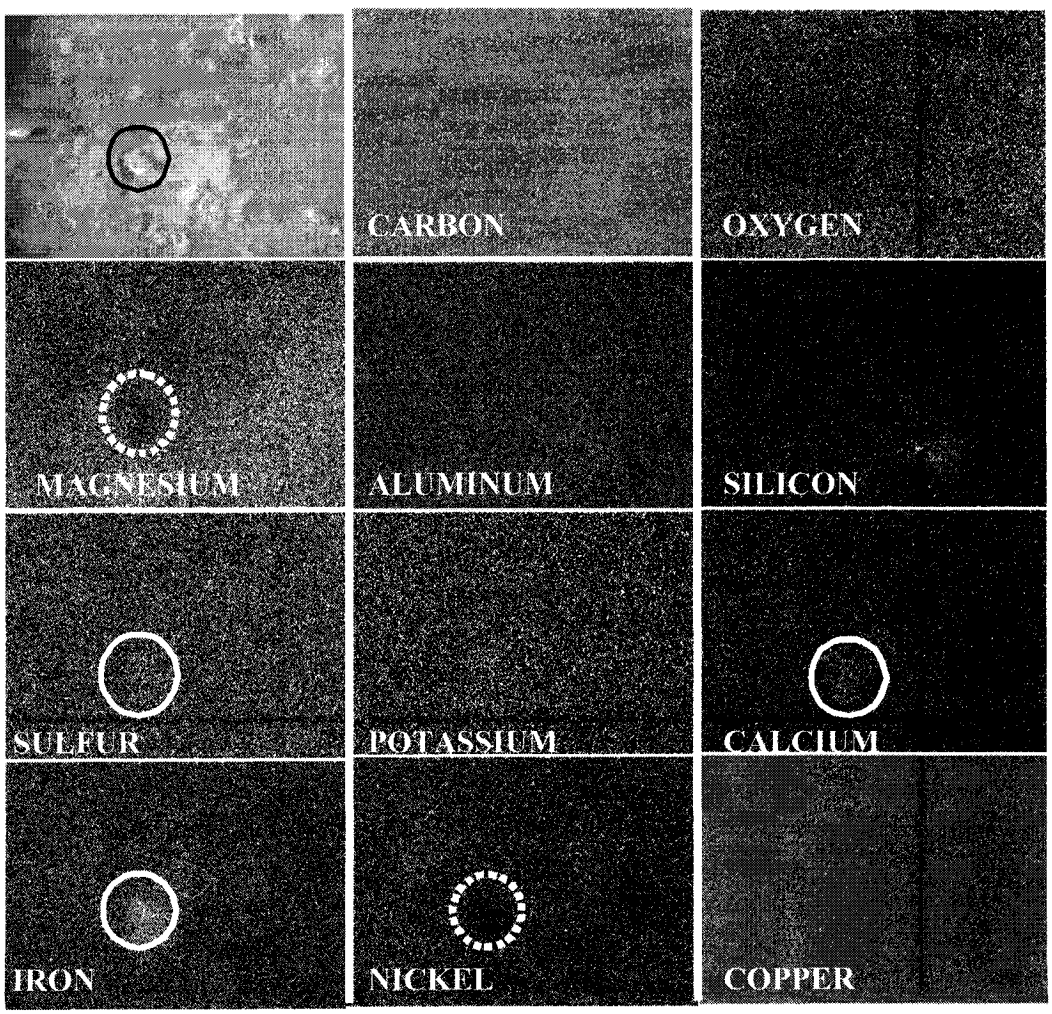

Figure 6.13: X-ray map of hydroxide matrix at a magnification of 6000 X. Full circles indicate location where an element is present, the dashed circle shows that these elements are absent in this area. Therefore, the particle is seen to contain S, Fe, and Ca but contains no Ni

This technique for high magnification colloidal particle size differentiation seems promising but requires further refinement. Image processing techniques may be better able to differentiate between subtle changes in the X-ray map contrast than the human eye.

Even without the high magnification maps, however, it is evident that the hydroxide matrix is more complex than a simple aggregation of the metal hydroxides. The presence of Si, Al, Ca, and S in the matrix indicates that there are other complexes present which may complicate the mineralogical assessment and certainly will affect leaching the nickel. The next section presents progressive sludge leaching experiments in an attempt to locate the Ni.

6.3 Hydroxide Sludge Leach Tests

Analysis of fresh sludge showed nickel was not only present as hydroxides, as a minor amount of nickel was incorporated in the crystal lattice of some gypsum particles. In order to obtain a more detailed understanding of the distribution of nickel mineralogy, sludge leach tests were employed, to fractionate and concentrate progressively more refractory nickel.

Figure 6.14 represents the results for Ni composition in the sludge leach residues. At pH 4, less nickel is extracted than at lower pHs, but it increases over time compared to pH 3.5 and pH 3. The nickel leaching can be attributed to the dissolution of hydroxides and other non-refractory nickel complexes. At the lower pH, the majority of hydroxides are presumably leached, therefore the remaining Ni concentration can be attributed to other more refractory metal-bearing complexes. The leach was not taken below pH 3 as this would dissolve the iron hydroxides.

The presence of Ni in the residue at pH 3 indicates that a nickel component still remains; most likely not nickel hydroxide. To analyze the residue mineralogy, X-ray mapping was again used on the VP-SEM. A systematic analysis of the residues at all leach conditions (pH/time) was performed to locate the refractory nickel components.

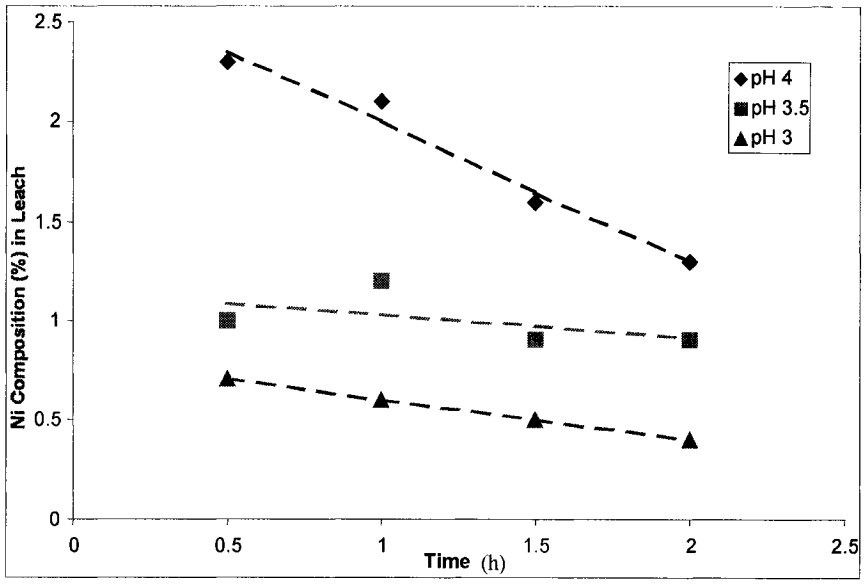

Figure 6.14: Nickel composition in the leach residues at pH 4, 3.5 and 3. Majority of the nickel is leached at pH 4 while slower nickel extraction occurs at lower pH's. Even at a pH of 3, some nickel remains in the residue.

The presence of the electron skirt, as described in chapters 2 and 5, hampers quantitative analysis. Interaction of skirt electrons outside of the target area results in erroneous and potentially misleading results. X-ray mapping, however, enables subtle changes in elemental composition to be seen in heterogeneous materials. This provides insight into the distribution of nickel in the predominantly iron hydroxide matrix which remains after leaching.

Mapping was performed on all 12 samples, the four timed samples at pH 4, 3.5 and 3. In addition to trying to differentiate between the hydroxide matrix and any nickel particles, an attempt was made to determine the relative abundance of these particles.

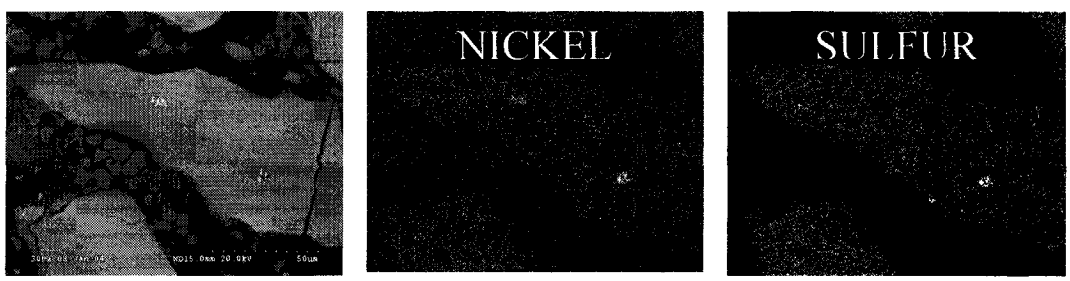

Figure 6.15: X-ray map results for hydroxide matrix at pH 3.5. Matrix contains Fe, Mg, Ni, S, Si, Al. In the matrix, there are two Ni particles present as well as a sulfur bearing particle

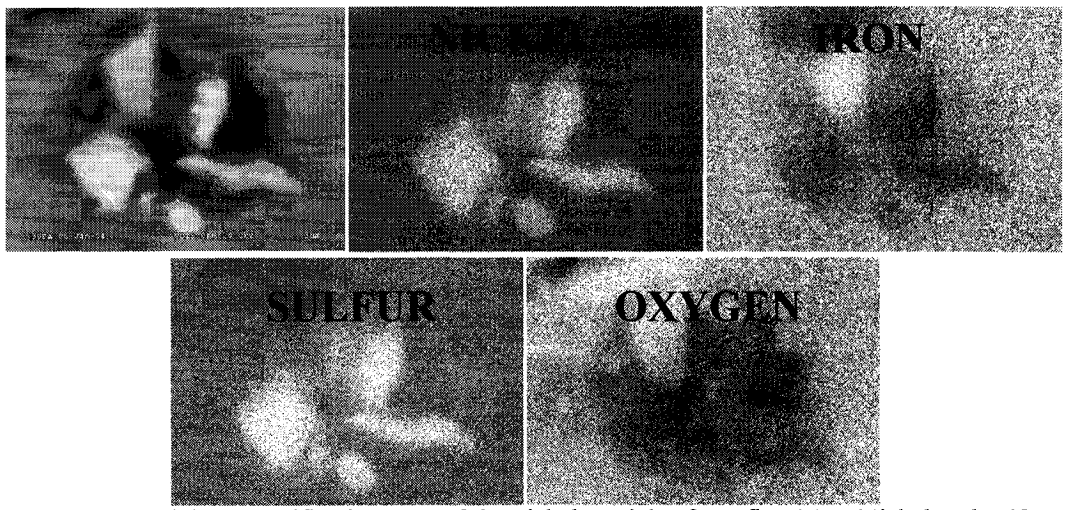

Figure 6.16: Higher magnification map of the nickel particles from fig. 6.15. Nickel and sulfur are dominant in several particles in this cluster which includes an iron oxide particle.

Figure 6.15 presents X-ray mapping results for a hydroxide sludge aggregate. Nickel and sulfur maps are shown to illustrate the efficiency of differentiating specific particles from a background. There appear to be two nickel particles, one of which contains sulfur. The Ni/S particle is further analyzed in Fig. 6.16. On higher magnification of Fig 6.15 the Ni/S particle is actually seen as a cluster of particles. There appears to be four Ni/S particles and one Fe/O particle enclosed in the hydroxide matrix. The oxygen map clearly shows the absence of oxygen in the nickel-bearing particles.

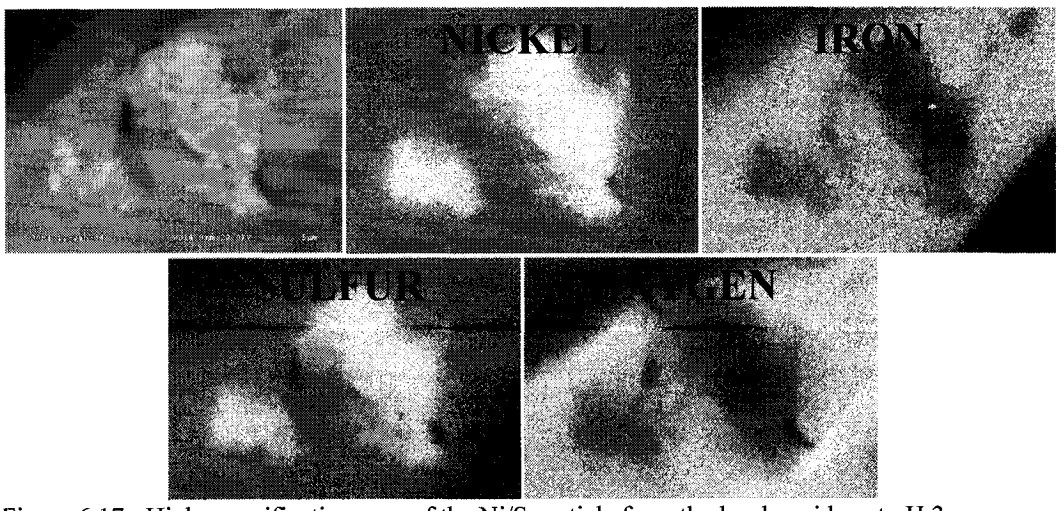

Figure 6.17: High magnification map of the Ni/S particle from the leach residue at pH 3.

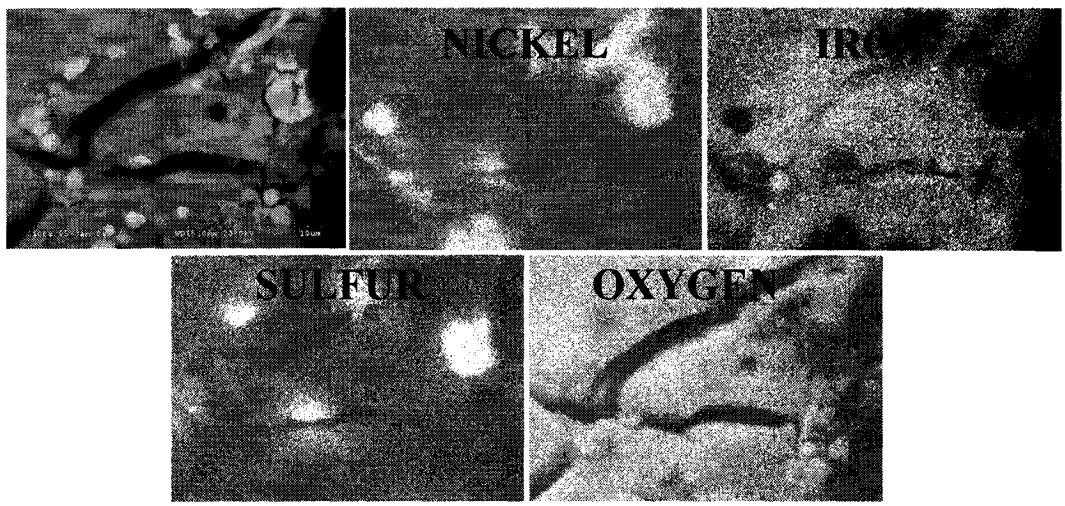

Figure 6.18: High magnification map of a cluster of nickel particles from the leach residue at pH 4. There is the presence of Ni/S particles as well as nickel oxide particles.

Figures 6.17 and 6.18 show Ni/S particles at pH 3 and pH 4, respectively. It was observed that the overall abundance of Ni/S particles did not significantly decrease with decreasing pH. This means that these sulfide particles are resistant to leaching (as expected) under the applied conditions.

There are also present nickel particles that do not contain sulfur, but do have elevated levels of oxygen (Figures 6.19, 6.20, and 6.21). They have been dubbed Ni/O to facilitate discussion; however, it is uncertain as to whether or not they were originally present as such, or represent oxidized elemental nickel, or dehydrated nickel hydroxides. These Ni/O were uniformly distributed throughout the products of all leach conditions; however, their overall abundance compared to the nickel sulfides was much less.

Along with the nickel particles, there are a significant number of Fe/S and Fe/O. These are much more abundant than the nickel particles, which is no surprise considering the iron content in the sludge. In much less abundance are the particles shown in Fig. 6.22. These represent Fe/Ni/S, Ni/Cu/O, Zn/S and Cu/S. These various particles are present in all the leach residues; however, they do not appear to represent any significant amount.

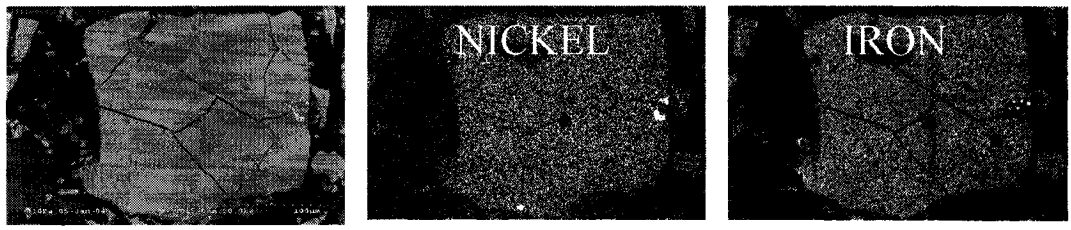

Figure 6.19: Low magnification map of a hydroxide matrix particle from the leach residue at pH 4. There is a presence of nickel oxides particles in the bottom and right hand side of the larger particle.

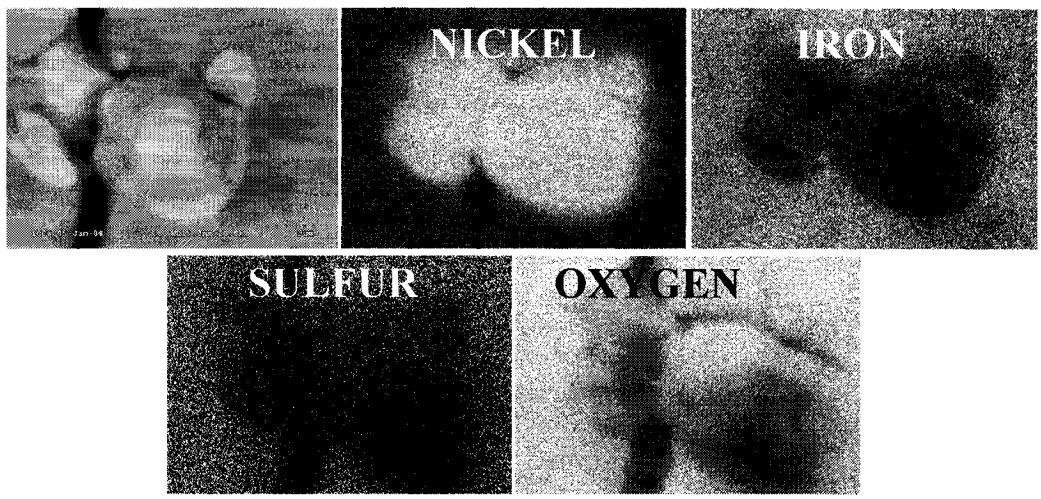

Figure 6.20: High magnification map of a nickel oxide material at pH 4. This is the nickel particle located in the bottom of Fig. 6.3.5.

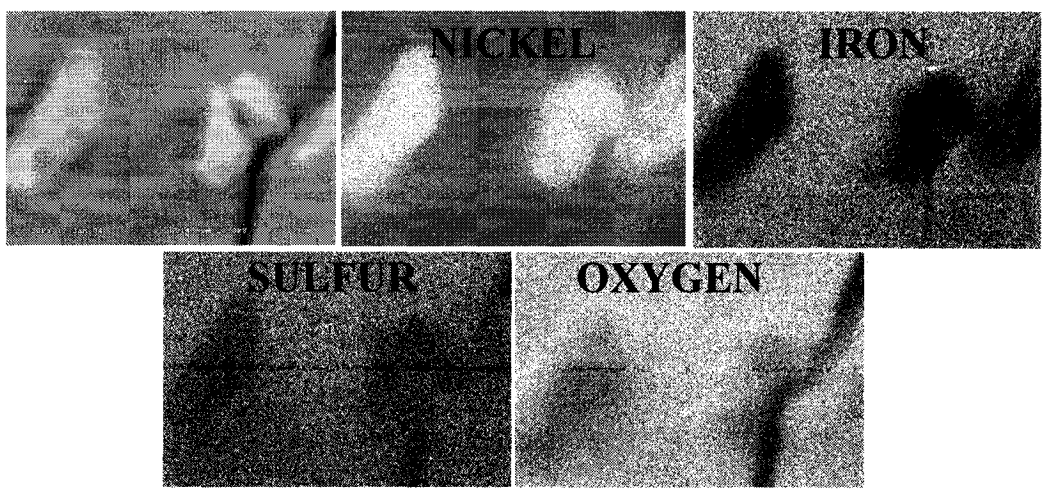

Figure 6.21: High magnification map of a nickel oxide material at pH 3.

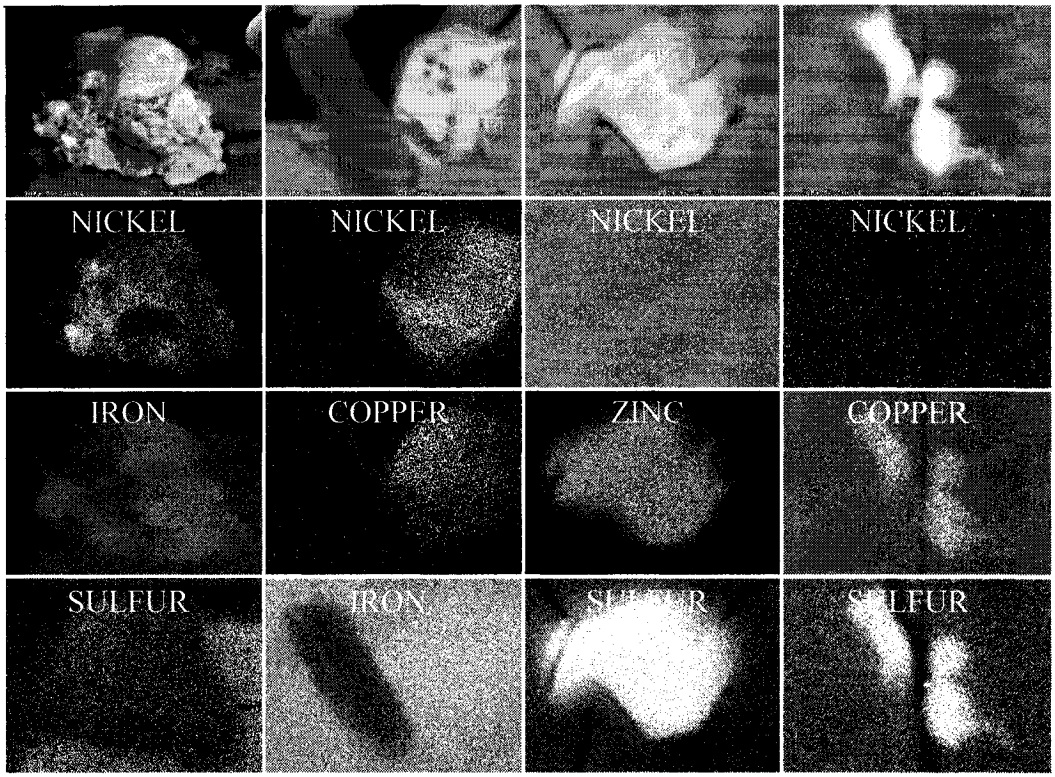

Figure 6.22: Various particles at all leach conditions. Most abundant particles in this group are the copper and zinc sulfides/sulphates.

Figures 6.15 and 6.19 present the X-ray map results for large hydroxide particles. Iron is clearly the dominant element in the matrix, however there is also a significant contribution from nickel, sulfur, aluminum and silicon. The nickel in the matrix is dispersed and most likely not a hydroxide due to the low leach pH. This form of nickel in the matrix indicates that there is a source of refractory nickel-bearing compounds other than sulfides and oxides. It is suggested that nickel-bearing complexes form, which are more stable than the hydroxides.

Figure 6.23 shows that aluminum, silicon and sulfur are present in the matrix. Their presence suggests the complexes form between nickel, aluminum, silicon, and sulfur.

Three spectra were collected under high vacuum to determine the overall composition. The spectra were collected at 15 000, 50 000, and 150 000 times magnification as seen in Fig. 6.23 by the sequence of boxes. This procedure results in an X-ray analysis which assesses the local homogeneity of the particle.

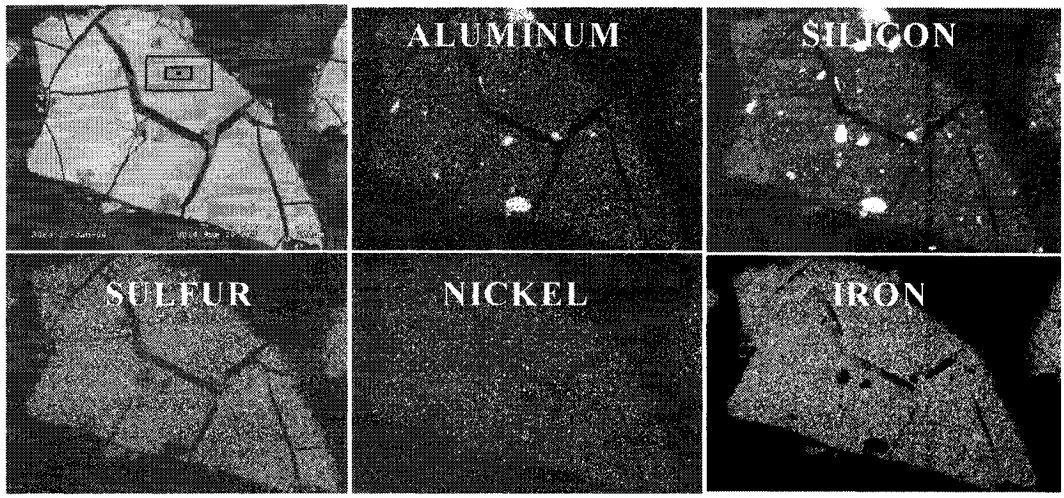

Figure 6.23: X-ray map of a matrix particle at high vacuum. Sample is coated with gold/palladium in order to minimize charging. Skirt effect is not present because of high vacuum conditions. Al and Si are present in the matrix. The location of the spectra acquisition are also indicated on the first image.

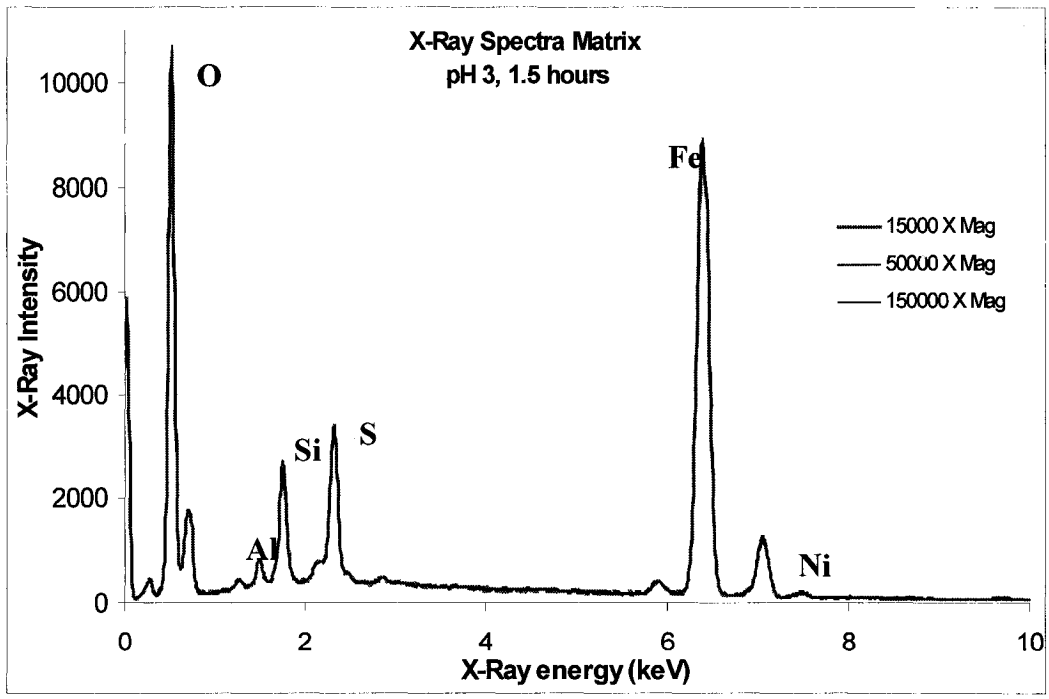

Figure 6.24: Superposition of spectra at 15 000, 50 000, and 150 000 times magnification of the matrix. Spectra were taken in an area where there were no nickel, iron, aluminum, or silicon particles. Therefore the spectra are representative of only the matrix. We see that there is a significant Si, S and Al component in the matrix.

The three spectra are superimposed in Fig. 6.24. It can be seen that they are identical, which indicates there is the same proportion of elements regardless of the size of the area being analyzed; i.e., there is homogeneity of the elemental distributions within the matrix.

Three spectra were also collected on four separate particles at a magnification of 15 000 X for a total of 12 spectra. Figure 6.25 shows all 12 spectra on the same plot. It is again observed that they are all very similar, confirming the homogeneity. Figure 6.26 is the Fe k α line; it can be seen that there is some variation in the peak value for the twelve spectra, however, the standard deviations are not very large. It is possible to calculate the degree of homogeneity using equation 6.1:

$$\pm \frac{3\sqrt{\bar{N}}}{\bar{N}} \bullet 100\% \qquad [6.1]$$

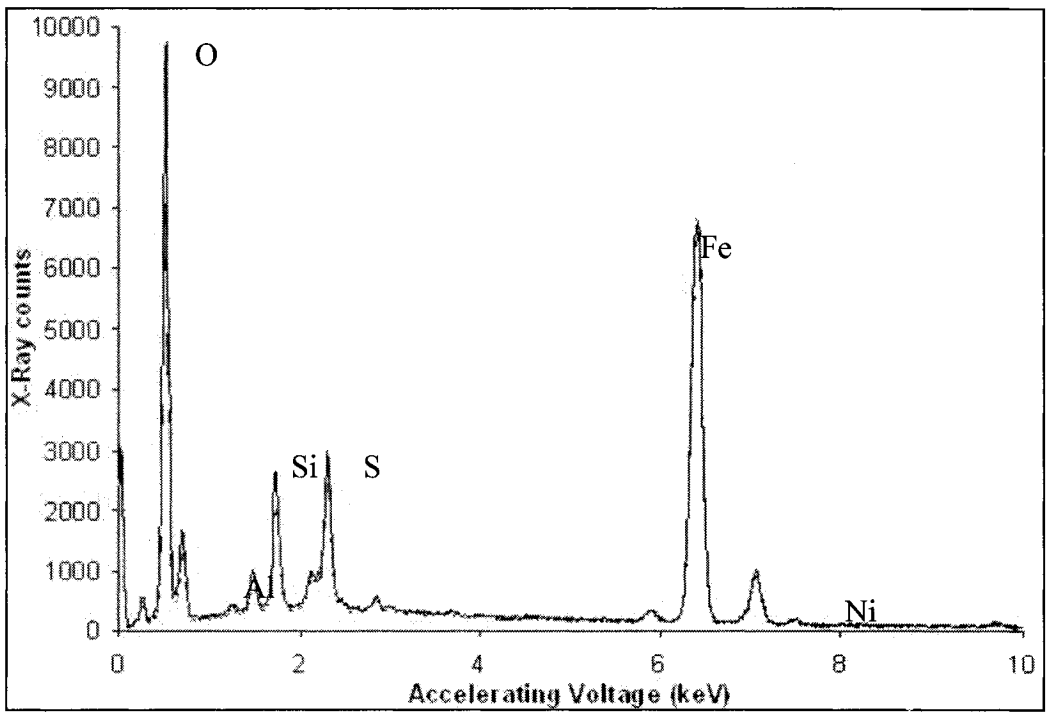

Figure 6.25: Superposition of 12 spectra. Three spectra were taken on four separate particles at pH 3. Areas were chosen where there was no detrital material. A magnification of 15 000 was used for all spectra.

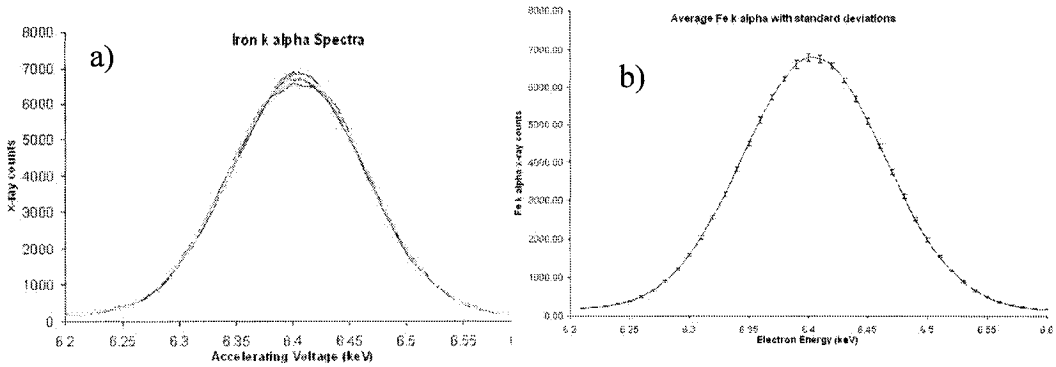

Figure 6.26: a) Superposition of the 12 spectra for the Fe k alpha peak. b) The mean X-ray intensity for the 12 spectra along with corresponding standard deviation. There is a good level of homogeneity apparent among the 12 spectra.

where $\overline{N}$ is the mean number of counts from all the spectra. Table 6.2 shows the mean, standard deviation and level of homogeneity for the 12 spectra. Fe, Si and S are close to $\pm$ 1% indicating that there is a high degree of homogeneity in the matrix. The nickel example shows a level of homogeneity of lower, $\pm$ 7%. The reason may be the generally lower peak to background ratio for this element which reflects the relatively low Ni content in the matrix.

Table 6.2: Mean, standard deviation and level of homogeneity for Fe, Si, S and Ni for 12 spectra.

Spectra #	IRON	SILICON	SULFUR	NICKEL
1	60347	21373	29707	1792
2	61407	20214	30549	1965
3	60593	19585	28803	1718
4	59835	22414	28742	1711
5	60585	20628	29091	1805
6	59438	19618	29336	1721
7	60995	20490	29200	1721
8	61600	20535	31088	1806
9	61208	22583	31715	1871
10	61098	20454	30943	1845
11	61122	20340	31545	1809
12	61277	23060	31629	1883
Mean	60792.08	20941.17	30195.67	1803.92
St.Dev.	654.55	1156.99	1164.05	78.81
% Homo.	**1.22**	**2.07**	**1.73**	**7.06**

The spectra confirm a significant amount of Si, Al and S in the matrix, supporting the conclusion that complexes form. The presence of such materials appears to hinder nickel leaching for, although the Ni content is low, the material is abundant. The origin of the complexes is open. It is unlikely that these leach resistant complexes would form homogeneously through out the sludge after it was formed; rather, these complexes apparently form during the neutralization process.

Taking advantage of the apparent homogeneity of the matrix particles, a semi quantitative analysis of the nickel and iron was performed at 30 Pa in the VP-SEM. Four spectra were taken on different particles for each leach condition. The relative peak heights nickel to iron were calculated and averaged. Particles were chosen which had limited detrital inclusions, in an attempt to classify only the matrix. The relative peak heights for iron and nickel were compared to the assay results for the bulk material (Fig 6.25). The trends for the two assay procedures are similar and at the lower pH, the values themselves are comparable.

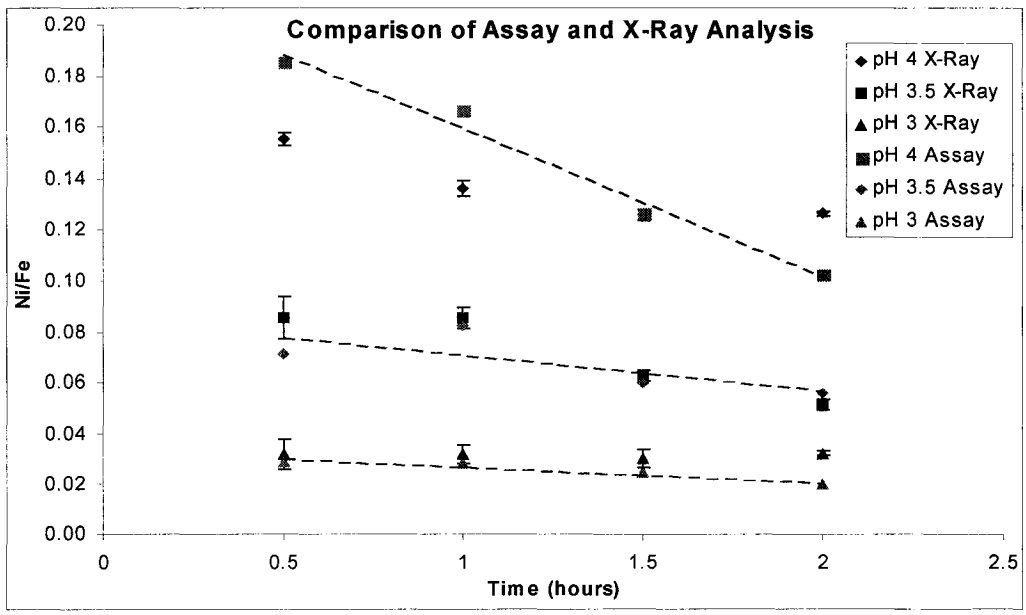

Figure 6.27: Comparison of the Ni/Fe relative peak heights for the X-ray spectra with the Ni/Fe ratio from the assay results.

There are two reasons why this semi-quantitative X-ray analysis works. First, it can be assumed that the iron concentration stays constant throughout the leaching. Iron as ferric-hydroxide does not leach above pH 3, therefore any change in the ratios of the relative peak heights can be attributed to a change in the nickel concentration. The second reason is the matrix homogeneity. Thus, even though X-ray analysis can only be of certain restricted areas several microns in size on a relatively few particles, the assay is essentially that of the bulk. Alternatively, the success can be taken as further evidence of the homogeneity of the sample.

Analysis of the products of the progressive leach showed that there are two sources for refractory nickel in the sludge. Ni/S and Ni/O become entrained in the sludge from the tailings impoundment as well as from other process waters (e.g., deriving from the smelter complex). The absence of carbon in the X-ray maps indicates that these are not carbonates. These materials were easily located with X-ray mapping because the elevated levels of nickel are revealed by very bright areas in the maps. These materials, however, appear not to represent the bulk of the refractory material.

A more important refractory material seems to be the nickel dispersed in the matrix. The leach tests were performed and the pH values were maintained constant throughout therefore, at pH 3 this nickel source is not hydroxide. They are most likely the result of complexes formed with colloidal aluminum and silicon which are resistant to leaching. Where and how these complexes form is not entirely clear. However, the overall homogeneity indicates they form before the samples are dried i.e., they form during the neutralization step. This colloidal nickel appears everywhere in the matrix, therefore, statistically, it represents the greater portion of the refractory nickel component in the sludge.

CHAPTER 7

CONCLUSIONS AND FUTURE WORK

7.1 Conclusions

7.1.1. Charge Contrast Imaging

Charge contrast is a dynamic charging effect that occurs in non-conductors and semi-conductors. It appears that differences in charge trap defect densities are imaged due to optimum charge compensation from the ion flux. The ion flux is dependant on variables such as pressure, bias, gas path lenght, and scan speed; therefore these variables ultimately control the charge contrast

The ion flux is best represented by the current that flows though the ESED detector (specimen current). Monitoring the specimen current through the ESED detector has shown that maximum charge contrast occurs at an optimum specimen current. In the gibbsite case, a specimen current around 3 nA appears to be the most beneficial for obtaining good charge contrast. There is, unfortunately, a high

degree of variability in the contrast achieved due to differences between dielectric properties in samples as well as differences in the day-to-day operation of the microscope.

Once the general parameters have been established for maximum charge contrast, there is a certain level of variability that can be applied by the user. Changing operating parameters while maintaining the optimum specimen current allows for continuous observation of charge contrast. As was seen by the low pressure analysis of gibbsite, a pressure of 30 Pa and an accelerating voltage of 5 keV yielded good charge contrast.

Nickel hydroxides show moderate charge contrast. Comparison of ESED and BSED images of nickel hydroxide sludge shows better differentiation of particles in the former. Contrast features appear in the ESED image that are not observable in the BSED image. Whether this increase in contrast is due to charging is not completely clear at this time.

Analysis of recycled nickel hydroxides gave some indication of charge contrast on these particles however it was not well defined. One drawback is that these particles were much smaller than the gibbsite. Charge contrast has been shown to be less prominent at high magnifications because the electron dose becomes too high. This tends to mask the subtle charge contrast effect.

7.1.2. Skirt Modeling

Measurement of skirt radius yielded a maximum radius of 2 mm at a pressure of 270 Pa. This is quite a large radius when considering that microanalysis of materials is on the order of microns. X-ray analysis must be performed with great caution to avoid misinterpretation of data.

Comparisons with the Monte Carlo results show that experimental skirts are greater. The theoretical results appear to underestimate the amount of scatter that occurs in the sample chamber. One reason for the theory underpredicting is that inelastic scattering is not incorporated into the model. This added component may increase the number of scattered electrons as well as the angle with which they are scattered.

Calculation of the fraction of non-scattered electrons (f_p) in this study yielded a large deviation from the theoretical results as well. Theoretical results yielded larger fp results, indicating that the model underestimates the amount of scattering events. There is some experimental error caused through sample charging, however, correcting this still yields inconsistent results. This error could be attributed to problems with the Rutherford cross-section. This parameter does not include inelastic collisions and does not consider molecular clusters. A more suitable sample is required however, to measure the scattering as a function of pressure whereby all charging is eliminated.

7.1.3. Nickel Sludge Analysis

Analysis of the acid mine drainage (AMD) lime treatment sludge showed that it was more complex than an agglomeration of gypsum and metal hydroxides. Three different components were established including the neutralization products, the detrital material and calcium deposited as the liquid dried. The use of X-ray maps allowed quick differentiation of elemental distributions in heterogeneous materials.

The detrital material consisted of particles around 50 μm, which is large compared to the colloidal sized neutralization products. The material also appeared to be crystalline. The X-ray maps showed that the particles were generally rich in silicon, aluminum and oxygen which indicates clay minerals such as montmorillinite and kaolinite. Silicates and sulfides were also quite common in this component. The large size, the crystalline nature and the composition all indicate that this material did not originate in the neutralization reaction and was most likely carried over from the tailings area and/or dredged from the river bottom as the sludge was pumped into the waste water treatment plant.

The neutralization products include the gypsum as well as the metal hydroxide particles. These hydroxides are fluffy and extremely small when observed in fresh sludge. Based on general observation they do not exhibit any significant settleability. Upon drying they form aggregates which become

extremely difficult to image with the microscope. Grain boundaries are almost invisible.

X-ray analysis showed the hydroxide "matrix" contains high levels of aluminum, silicon, and sulfur. The origin of these elements is unknown as well as how they become incorporated into the hydroxide aggregates.

An attempt to correlate the hydroxide grain boundaries from charge contrast with X-ray mapping proved moderately successful. High X-ray counts were needed in order to distinguish between individual hydroxide particles. The resultant map showed a concentration of iron which could be associated with a feature in the ESED image, however, the contrast in the map was poor. Longer counting times as well as the development of image processing techniques may enhance the subtle variation on elemental concentrations.

Progressive sludge leaching was performed in order to identify the leach resistant form of nickel. The bulk of the nickel remaining was associated with colloidal nickel in the "matrix", with minor contributions from nickel sulfides and oxides.

Mapping clearly showed that the Ni/S and Ni/O were ubiquitous through out all leach conditions. It is believed that the Ni/S (nickel sulfide) are from the tailings plant. It is possible that the Ni/S is nickel sulfate and these would have formed during the neutralization reaction. The Ni/O are believed to be oxidized elemental nickel originating from smelter process water.

The larger portion of unleachable nickel was located in the "matrix" in association with aluminum and silicon. These elements most likely are complexing and generating a leach resistant material.

The matrix was shown to exhibit a large degree of homogeneity by comparing X-ray spectra from three different areas and sizes of area. The spectra were all virtually homogeneous. Comparing the relative peak height of nickel versus iron with the general bulk assay showed similar trends. This shows there is significant sample homogeneity.

7.2 Future Work

1. Understand the mechanism that drives charge contrast. A new technique for measuring the ion flux is needed as well as a method to map charge trap sites on the sample surface.
2. Image gibbsite under the FEG-SEM using the upper detector at various biases. This detector images SE1, therefore, if the CCI is created through enhancement of SE1 at charge traps, the FEG SEM should observe them.
3. Precipitate larger nickel hydroxide particles to avoid overdosage from the electron beam at high magnification. One should then be able to see the growth rings to a much greater extent.
4. Develop a sample that is more dedicated to the measuring of the percent scattering of electrons. A conductive sample with a rod of aluminum or copper less than 25 μm is suggested. This would eliminate charging effects as well as the problem of detecting the target element in the skirt electrons.
5. Perform a mass balance on the sludge in order to account for all of the nickel present. Compare the nickel recovered from leach tests with nickel unleached.
6. Develop strategies for removal of the "unleachable" nickel component.
7. Develop image processing techniques to increase the effectiveness of high magnification X-ray maps.

REFERENCES

[1] Kuyucak, N. (2002) CIM Bulletin, 95 (1060), 96-102.

[2] MEND, 2000. 5.4.2e Treatment.

[3] Evangelou, V.P., "Pyrite Oxidation and It's Control". CRC Press, New York, (1995).

[4] Younger, P.L., Banwart, S.A., amd Hedin, R.S., "Mine Water: Hydrology, Pollution, and Remediation". Kluwer Academic Publishers, Dordrecht, (2002).

[5] Zinck, J.M., Aubé, B.C., (2000) CIM Bulletin, 93 (1043), 98-105.

[6] Omelon, S., Demopoulos, G.P., (1995) Production of High Density Gypsum by Controlled Neutralization of Simulated Zinc Plant Wastewaters, "Waste Processing and Recycling III, The Metallurgical Society of CIM".

[7] Aubé, B.C., Zinck, J.M., Comparison of AMD Treatment Processes and Their Impact on Sludge Characteristics. Proceedings for Sudbury '99, Mining and the Environment II.

[8] Zinck, J.M., Griffith, W.F., An Assessment of HDS-Type Lime Treatment Processes-Efficiency and Environmental Impact. 5th international conference on Acid Rock Drainage, Denver Colorado 1027-1034. (2000).

[9] Demopoulos, G.P., Zinck, J.M., Kondos, P.D., (1995) Production of Super Dense Sludges with a Novel Neutralization Process. Proc. Int'l Symp. Waste Processing and Recycling, R. Rao et al., (Eds.), CIM, Montreal, QC, pp. 401-412.

[10] Verbaan, C.M., Omelon, S.J., Demopolous, G.P., The Effect of Staging and Seeding/Recycling on the Density and Cleanliness of Gypsum Produced in Simulated Zinc Plant Wastewater Treatment Circuits.

[11] MEND, (1997). 3.42.2 Characterization and Stability of Acid Mine Drainage Treatment Sludges.

[12] MEND, (1997). 3.42.2b The Effect of Process Parameters and Aging on Lime Sludge Density and Stability.

[13] Goldstein, J.I., Newbury, D.E., Echlin, P., Joy, D.C., Romig, A.D., Lyman, C.E. and Lifshin, E., 1992. *Scanning Electron Miroscopy and X-Ray Microanalysis,* Plenum Press, New York.

[14] Baroni, T.C. (2001) PhD Thesis, A microstructural investigation of gibbsite crystallization in bayer liquors. University of Western Australia.

[15] Cazaux, J. (1999) Some considerations on the secondary electron emission from e^- irradiated insulators. Journal of Applied Physics, 85, 1137-1147.

[16] Farley, A.N., and Shah, J.S. (1991) High-Pressure scanning electron microscopy of insulating materials: a new approach. Journal of Microscopy, 164, 107-126.

[17] Mohan, A., Khanna, J., Hwu, and J., Joy, D.C. (1998) Secondary electron imaging in the Variable Pressure Scanning Electron Microscope. Scanning, 20, 436-441.

[18] Meridith, P., Donald, A.M., and Thiel, B. (1996) Electron-gas interactions in the environmental scanning electron microscopes gaseous detector

[19] FEI (2000) Introduction to the ESEM.

[20] Farley, A.N., and Shah, J.S. (1990) Primary considerations for image enhancement in high pressure scanning electron microscopy. Journal of Microscopy, 158, 379-388.

[21] Danilatos, G.D. (1990) Mechanisms of detection and imaging in the ESEM. Journal of Microscopy, 160, 9-19.

[22] Farley, A.N., and Shah, J.S. (1990) Primary considerations for image enhancement in high pressure scanning electron microscopy. Journal of Microscopy, 158, 389-401.

[23] Toth, M., and Phillips, M.R., (2000) The Effects of Space Charge in Images Obtained Using the Environmental Scanning Electron Microscope. Scanning, 22, 319-325.

[24] Fletcher, A.L., Thiel, B.L., and Donald, A.M. (1997) Amplification measurements of alternative imaging gases in the environmental SEM. J. Phys. D: Appl. Phys., 30, 2249-2257.

[25] Fletcher, A.L., Thiel, B.L., and Donald, A.M. (1999) Signal Components in the Environmental Scanning Electron Microscope. Journal of Microscopy, 196, 26-34.

[26] Toth, M., Daniels, D.R., Thiel, B.L., Donald, A.M. (2002) Quantification of Electron-Ion Recombination in an Electron-Beam-Irradiated Gas Capacitor. J. Phys. D: Appl. Phys., 35, 1796-1804.

[27] Toth, M., Thiel, B.L., Donald, A.M., (2003) Interpretation of Secondary Electron Images Obtained Using the Low Vacuum SEM. Ultramicroscopy, 94, 71-87.

[28] Danilatos, G.D., (1988). Foundations of ESEM. Advances in Electronics and Electron Physics, 71, 110-248.

[29] Mathieu, C., (1999) The Beam-Gas and Signal-Gas Interactions in the Variable Pressure Scanning Electron Microscope. Scanning Microscopy, 13, 23-41.

[30] Craven, J.P., Baker, F.S., Thiel, B.L., and Donald, A.M. (2002) Consequences of positive ions upon imaging in low vacuum scanning electron microscopy. Journal of Microscopy, 205, 96-105.

[31] Toth, M., Thiel, B.L., and Donald, A.M. (2002) On the role of electron-ion recombination in low vacuum scanning electron microscopy. Journal of Microscopy, 205, 86-95.

[32] Moncrieff, D.A., Robinson, V.N.E., Harris, L.B., (1978) Charge neutralisation of insulating surfaces in the SEM by gas ionization. J. Phys. D: Appl. Phys., 11, 2315-2325.

[33] Durkin, R., Shah, J.S. (1993) Amplification and Noise in High-Pressure Scanning Electron Microscopy. Journal of Microscopy, 169, 33-51.

[34] von Engel Ionized Gases (Oxford:Clarendon) (1965).

[35] Thiel, B.L., Bache, I.C., Fletcher, A.L., Meredith, P. and Donald, A.M. (1997) An improved model for gaseous amplification in the environmental SEM. Journal of Microscopy, 187, 143-157.

[36] Moncrieff, D.A., Barker, P.R., Robinson, V.N.E., (1979) Electron Scattering by Gas in the Scanning Electron Microscope. J. Phys. D: Appl. Phys., 12, 481-488.

[37] He, J., Joy, D.C., (2003) Measurement of Total Gas Scattering Cross-Section. In Publication.

[38] Gauvin, R., (1999) Some Theoretical Considerations on X-Ray Microanalysis in the Environmental or Variable Pressure Scanning Electron Microscope. Scanning, 21, 388-393.

[39] Hovington, P., Drouin, D., Gauvin, R. (1997) Casino: A new era of monte carlo in C language for electron beam interation. Scanning, 19, 1-35.

[40] Gauvin, R., and Joy, D.C. (2000) On the measurement of the total elastic cross-section in the ESEM or VP-SEM using X-ray microanalysis, Microscopy and Microanalysis 6 (Suppl. 2), 788-789

[41] Wight, S.A. (2001) Experimental Data and Model Simulations of Beam Spread in the Environmental Scanning Electron Microscope. Scanning, 23, 320-327.

[42] Gilpen, C., Sigee, D.C. (1995) X-Ray Microanalysis of Wet Biological Specimens in the Environmental Scanning Electron Microscope. 1. Reduction of Specimen Distance Under Different Atmospheric Conditions. Journal of Microscopy, 179, 22-28.

[43] Kadoun, A., Belkorissat, R., Mathieu, C., Khelifa, B. (2003) Computation and Experiments on the Beam Spread in the VP-SEM : Application to X-Ray Microanalysis. Journal of Trace and Microprobe Techniques, 21, [2], 229-238.

[44] Gauvin, R., Griffin, B., Nockolds, C., Phillips, M., Joy, D.C. (2002) A Method to Measure the Effective Gas Path Length in the Environmental or Variable Pressure Scanning Electron Microscope. Scanning, 24, 171-174.

[45] Griffin, B.J. (1992) Effects of chamber pressure and accelerating voltage of x-ray resolution in the ESEM Proc 50th annual meeting EMSA (eds. Bailey G.W., Bentley J, Small J.A.) San Francisco Press. San Francisco 1324-1325.

[46] Carlton, R.A. (1997) The Effect of Some Instrument Operating Conditions on the X-Ray Microanalysis of Particles in the Environmental Scanning Electron Microscope. Scanning, 19, 85-91.

[47] Joy, D.C. and Joy, C.S. (1996) Low voltage scanning electron microscopy. Micron, 27, 247-263.

[48] Mansfield, J.F. (2000) X-Ray Microanalysis in the Environmental SEM: A Challenge or a Contradiction? Mikrochim. Acta, 132, 137-143.

[49] Doehne, E. (1997) A New Correction Method for High-Resolution Energy-Dispersive X-Ray Analyses in the Environmental Scanning Electron Microscope. Scanning, 19, 75-78.

[50] Griffin, B.J. (1997) A new mechanism for the imaging of crystal structure in non-conductive materials: An application of charge-induced contrast in

the environmental scanning electron microscope (ESEM). Microsc Microanal 3 (S2), 1197-1198.

[51] Griffen, B.J. (2000) Charge contrast imaging of material growth and defects in ESEM-linking electron emission and cathodoluminescence. Scanning, 22, 234.

[52] Watt,G.R., Griffin, B.J., and Kinny P.D.(2000) Charge contrast imaging of geological materials in the environmental scanning electron microscope. American Mineralogist, 85, 1784-1794.

[53] Toth, M., Phillips, M.R., Thiel, B.L., and Donald, A.M. (2002) Electron imaging of dielectrics under simultaneous electron-ion irradiation. Journal of Applied Physics, 91, 4479-4491.

[54] Griffin, B.J., Suvorova, A.A. (2003) Charge Related Problems Associated with X-Ray Microanalysis in the Variable Pressure Scanning Electron Microscope at Low Pressures. Microscopy and Microanalysis, 9, 155-165.

APPENDIX A

GIBBSITE IMAGES

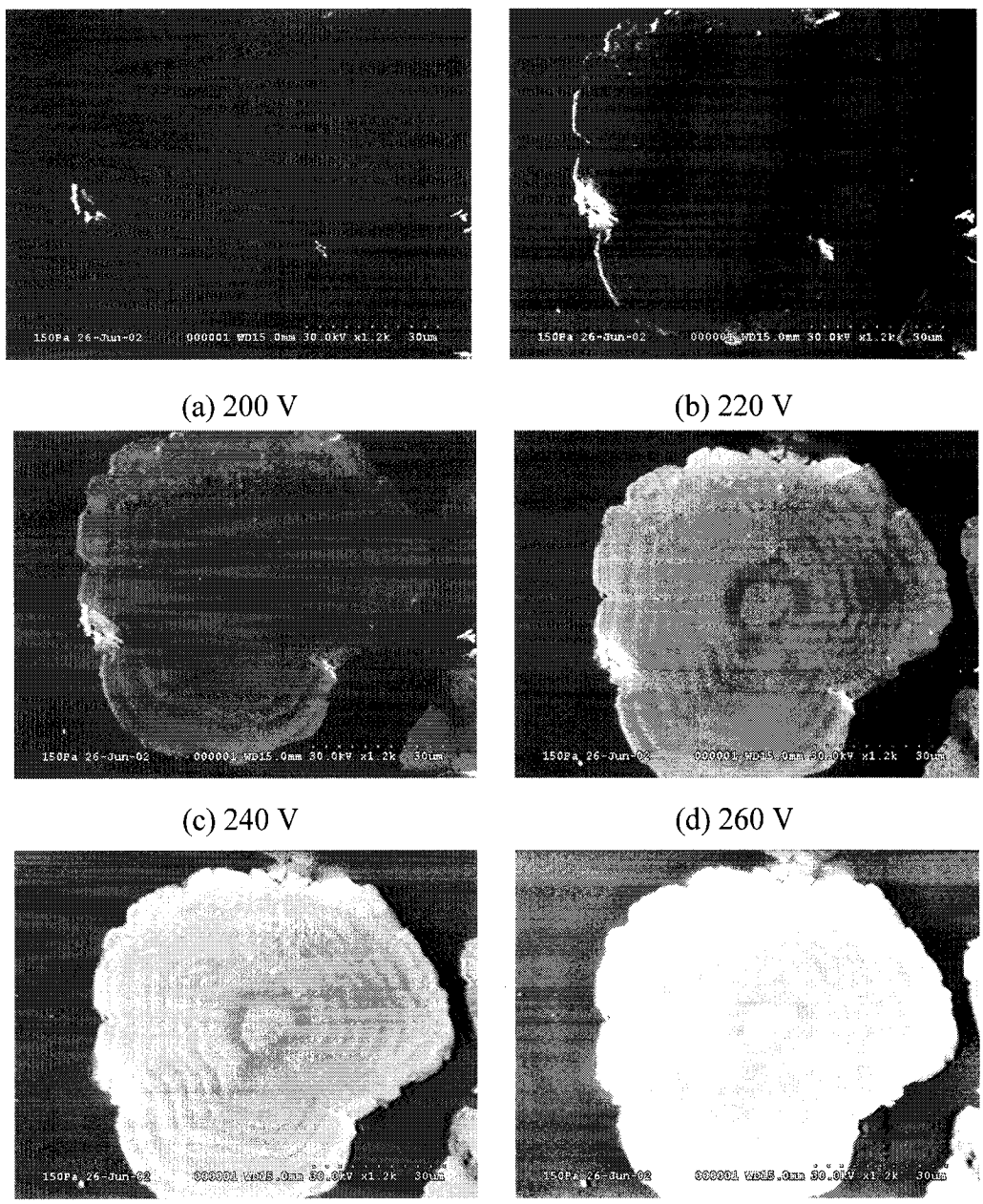

(a) 200 V (b) 220 V

(c) 240 V (d) 260 V

(e) 280 V (f) 300 V

Figure A.1: Bias is altered while maintaining all other variables constant. Increasing bias increases amplification of secondary electrons resulting in brighter images. Normalizing the linescans removes this effect.

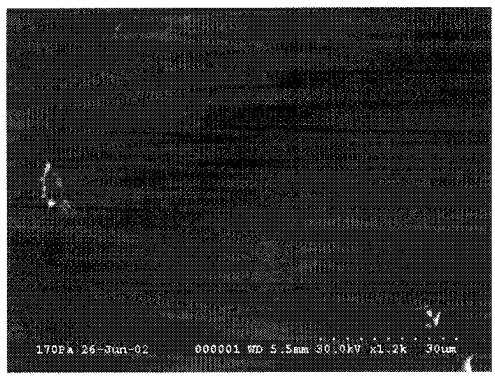

(a) 5.5 mm

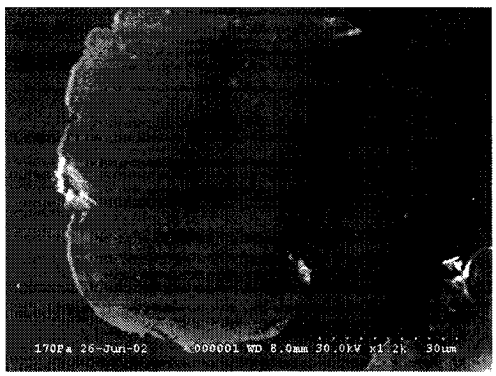

(b) 8 mm

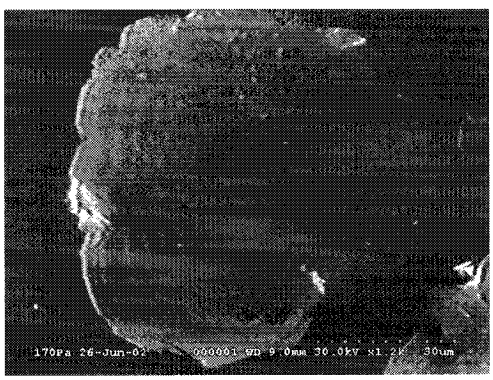

(c) 9 mm

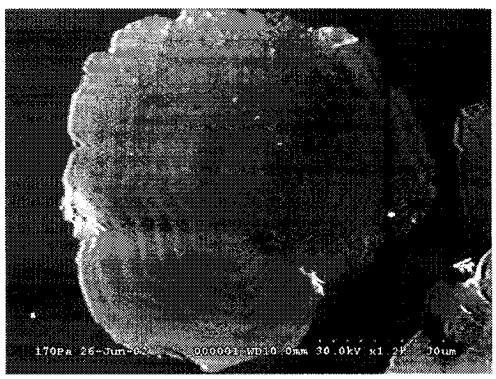

(d) 10 mm

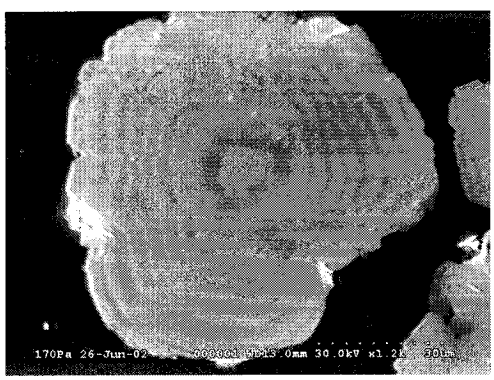

(e) 13 mm

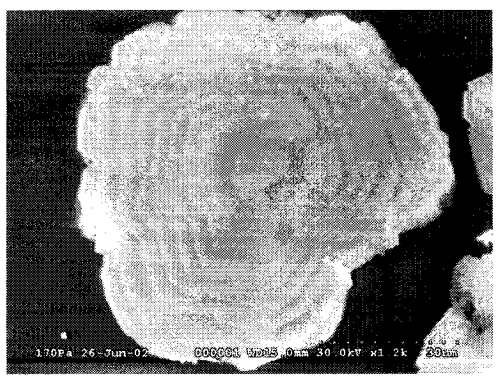

(f) 15 mm

Figure A.2: Working distance (WD) is varied maintaining all other variables constant. Increasing WD increases the overall amplification of the secondary electrons.

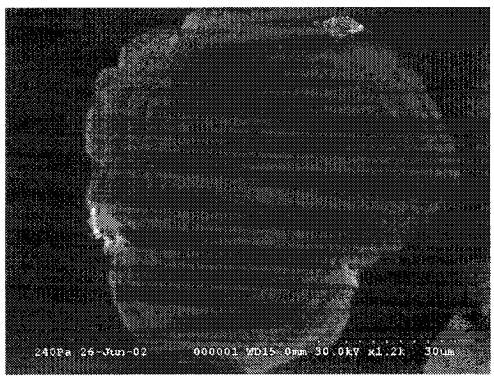

(a) 240 Pa

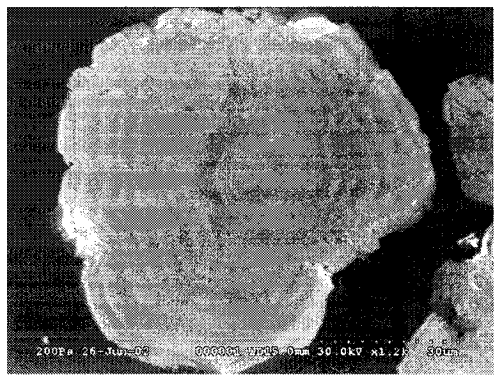

(b) 200 Pa

(c) 170 Pa

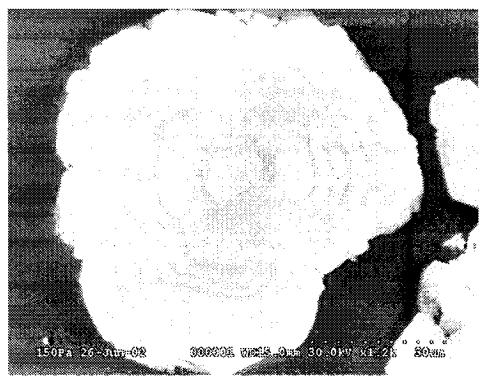

(d) 150 Pa

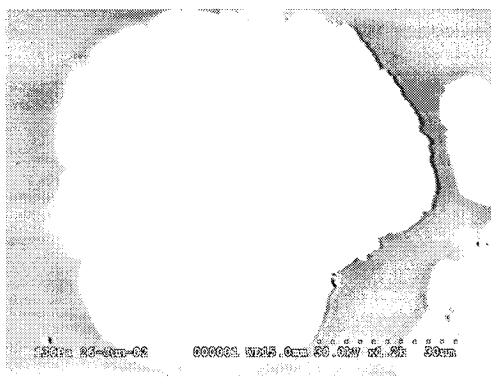

(e) 130 Pa

Figure A.3: Pressure is varied at the same operating conditions as Figure A.2. As pressure decreases, amplification decreases due to a decrease in the probability of collisions. Normalization of linescans was used to eliminate the amplification effect.

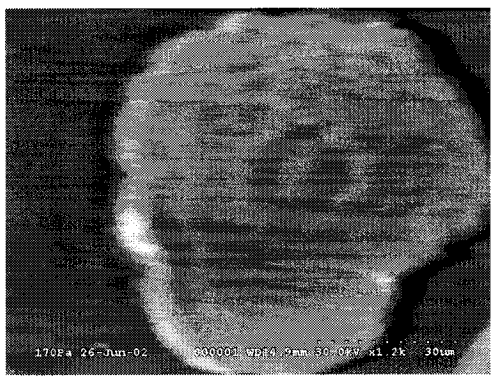

(a) slow 1

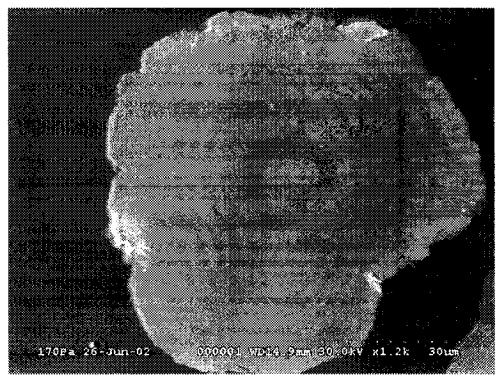

(b) slow 2

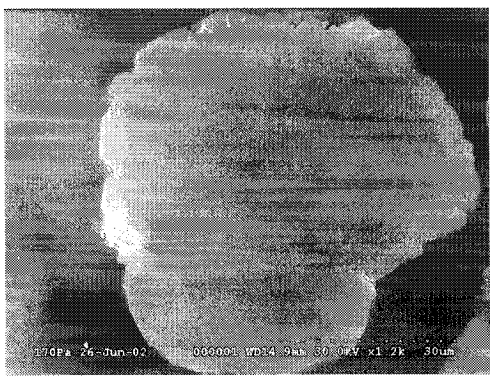

(c) slow 3

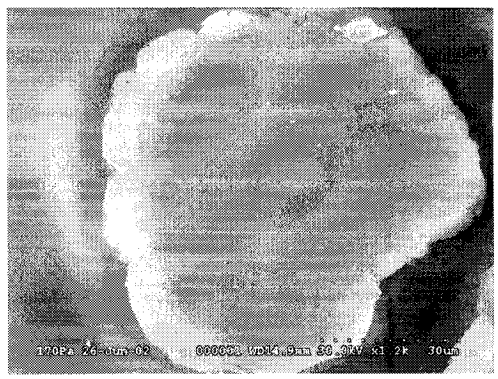

(d) slow 4

Figure A.4: The scan rate was varied while maintaining the same operating conditions. Values for scan rates (frames/second) are not available on this microscope however four distinct rates are available. Slow 1 is the fastest and slow 4 is the slowest. As scan rate decreases, the beam dwells longer on individual pixels increasing the SE emission which increases amplification and overall resolution.

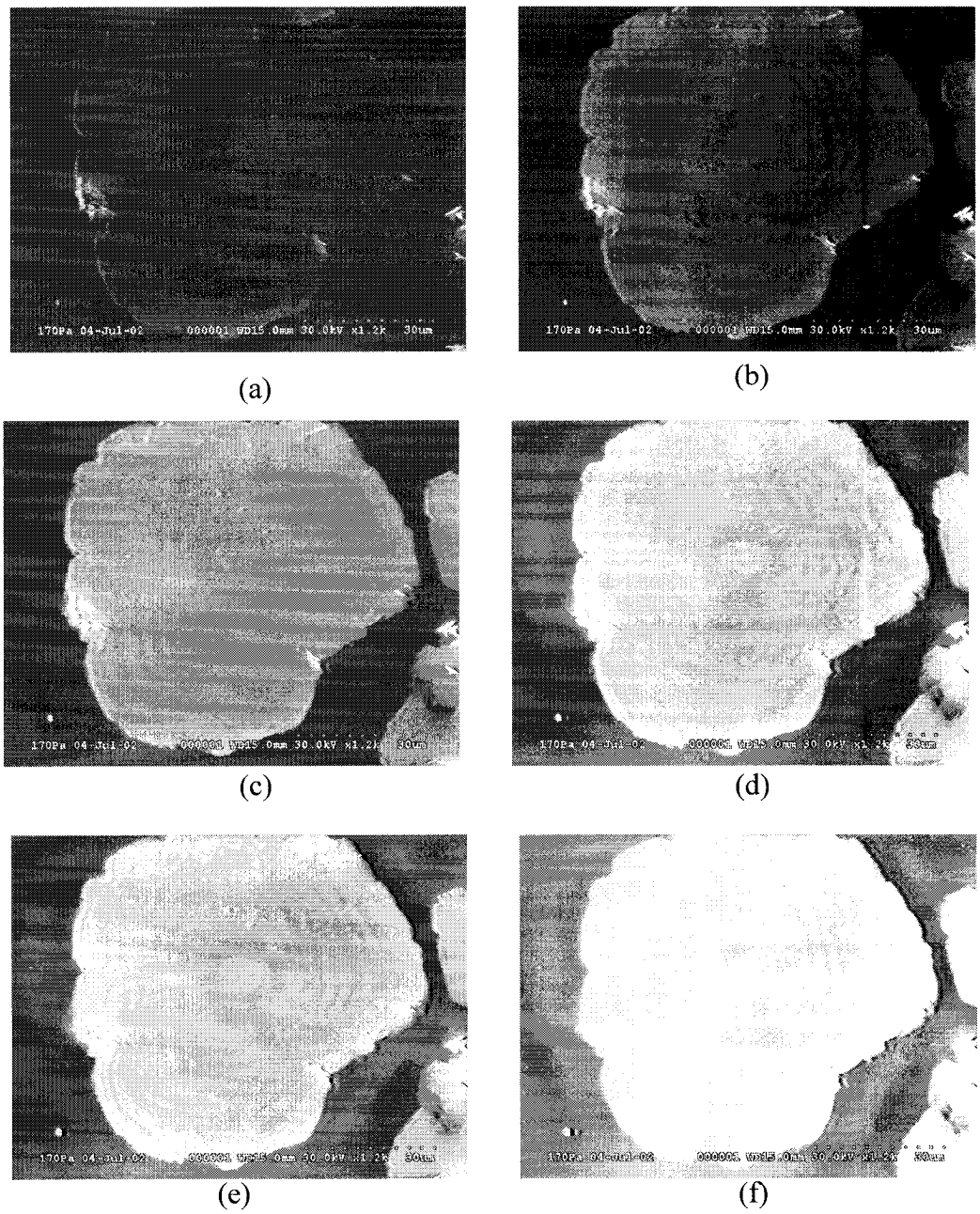

Figure A.5: The beam current is varied for conditions at 30 keV, 150 Pa, and 300 V. As the beam current increases, more secondary electrons are generated thereby increasing the overall amplification. Beam current affects the amplification due to an increase in the SE emission, not from any intrinsic affect on the amplification behaviour.

APPENDIX B

DETRITAL MATERIAL X-RAY MAPS

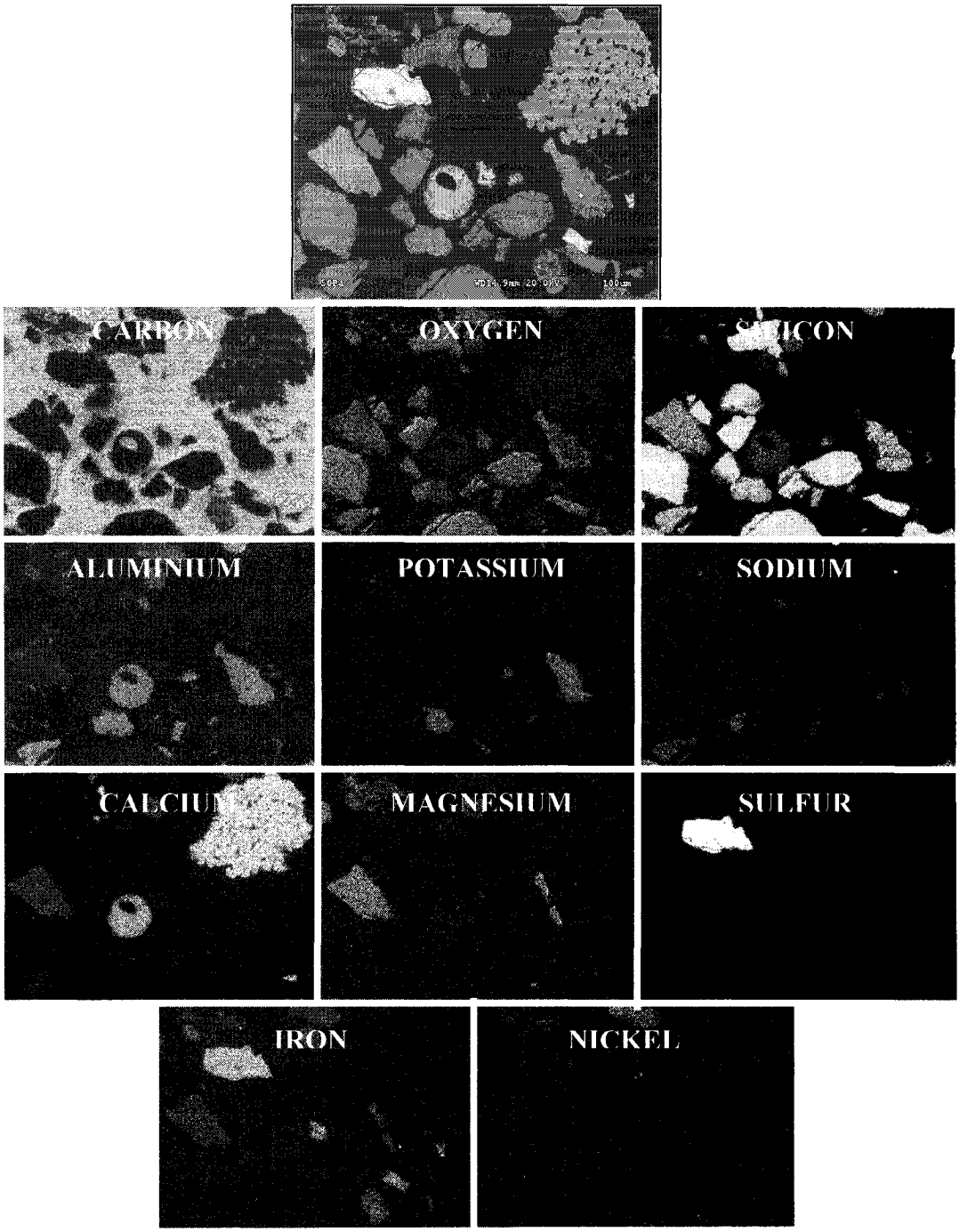

Figure B.1: X-ray map of a cluster of detrital particles. Quartz appears to be the dominant mineral. A large cluster of calcium oxide particles are present, along with an iron sulfide. Aluminosilicates; consisting of aluminum, potassium, sodium and magnesium are also noted.

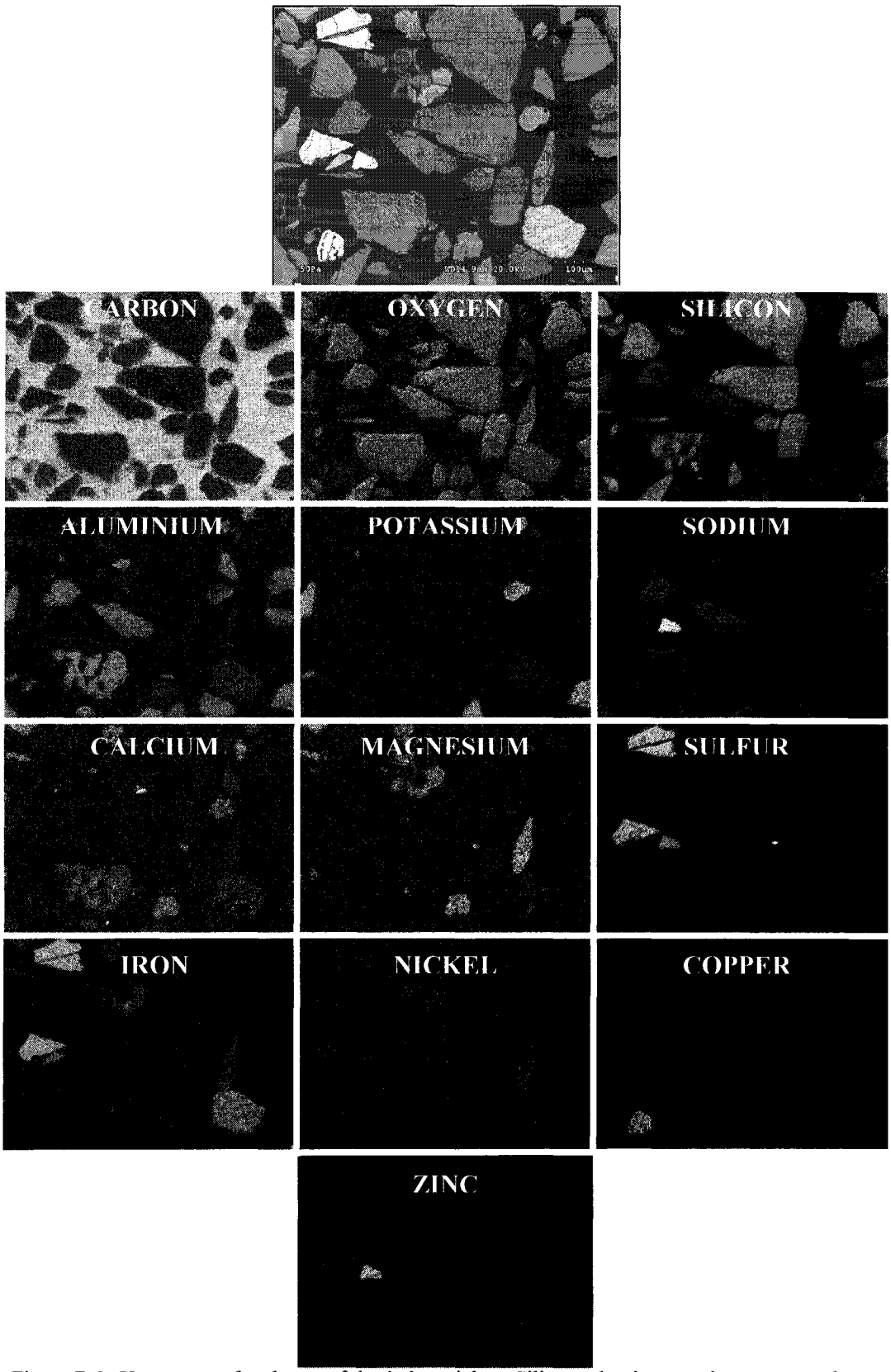

Figure B.2: X-ray map of a cluster of detrital particles. Silicon, aluminum and oxygen are the predominant elements forming silicates and aluminosilicates, followed by potassium, sodium, calcium and magnesium. Iron sulfides are present along with nickel , copper and zinc.

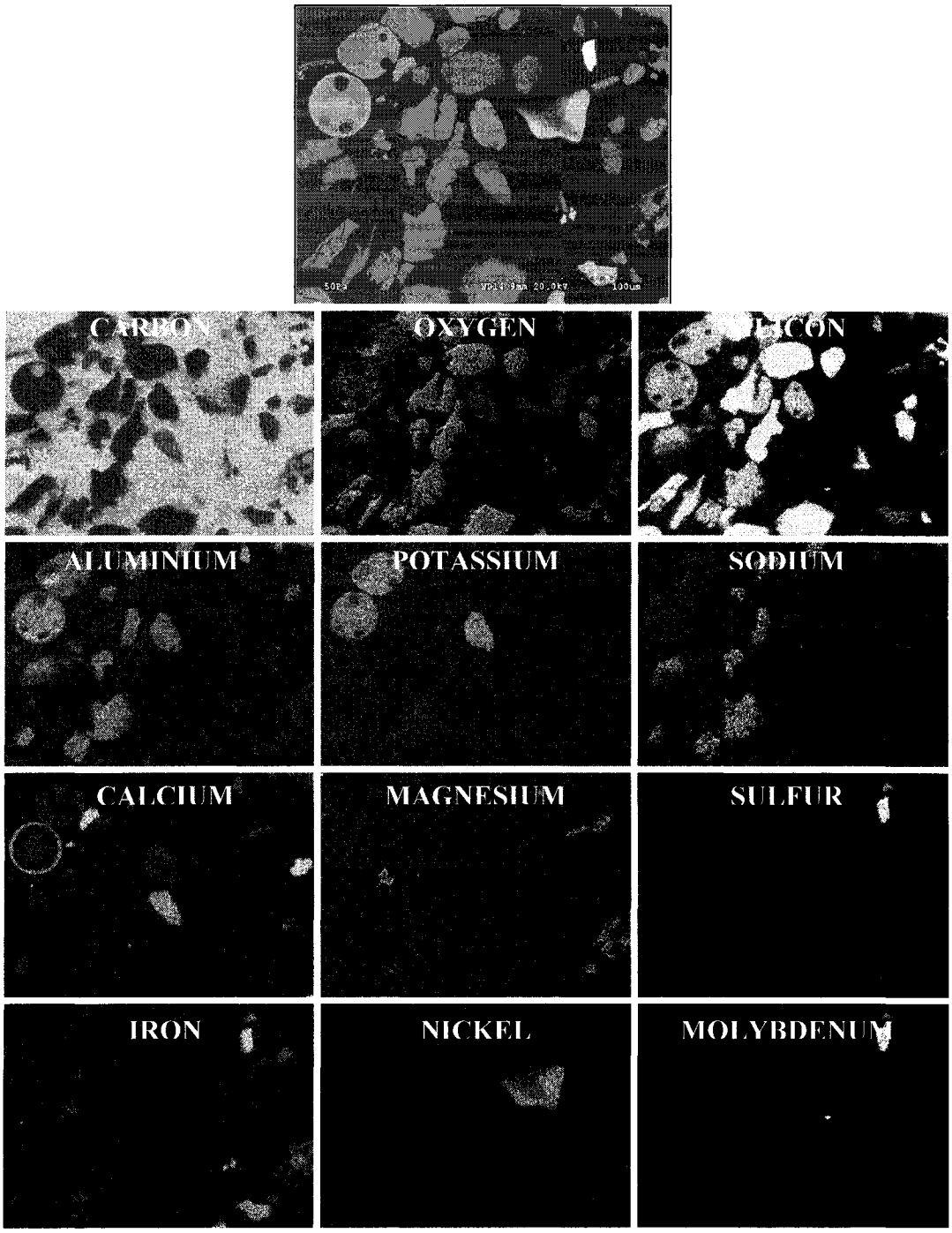

Figure B.3: X-ray map of a cluster of detrital particles. Again, quartz is the predominant material, followed by various aluminosilicates containing Al, Si, K, and Na. An iron sulfide is identified which also contains molybdenum. A large nickel particle is identified with no associated element, indicating it is elemental nickel.

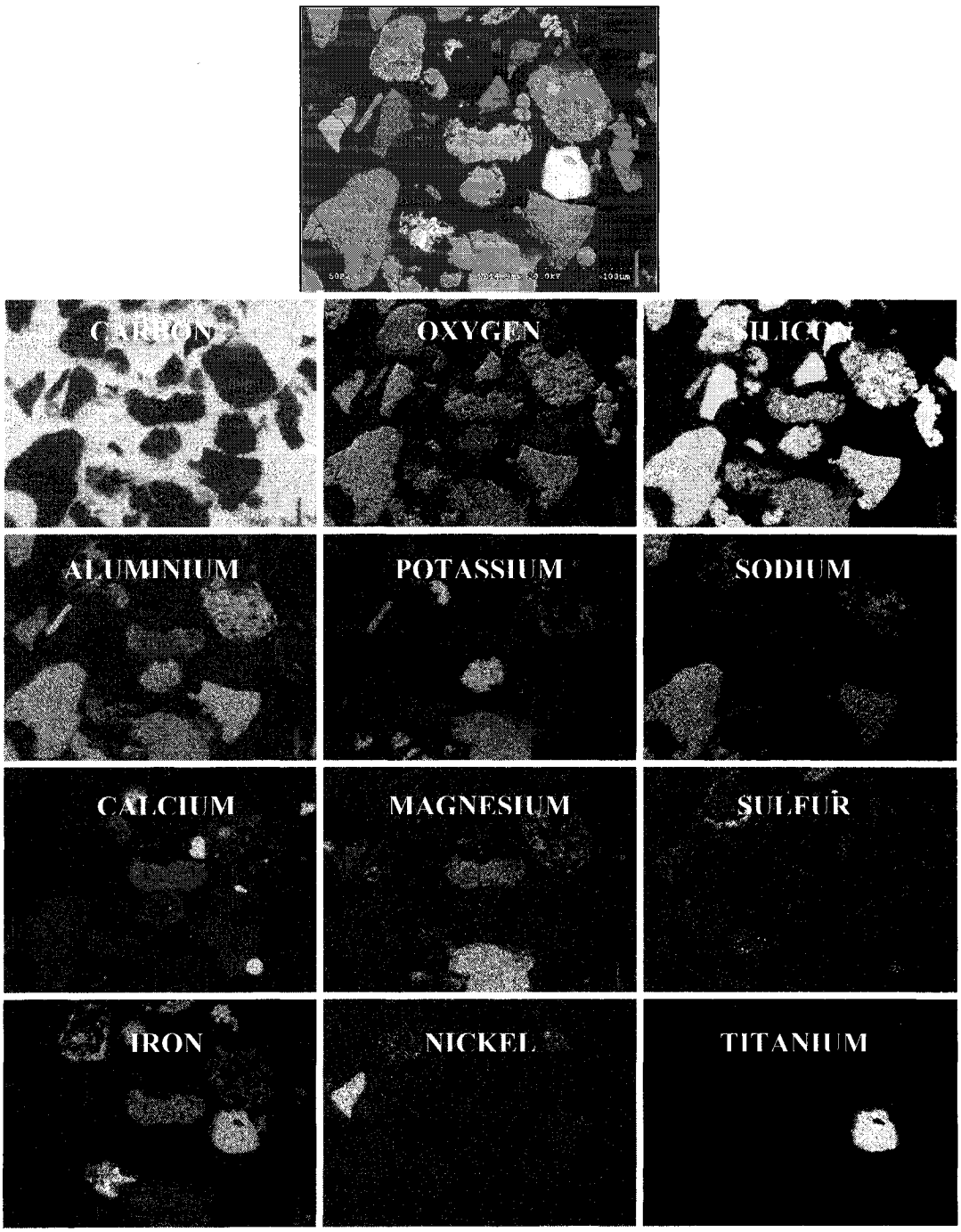

Figure B.4: X-ray map of a cluster of detrital particles. This cluster of particles has a high proportion of aluminosilicates. There are elevated levels of potassium and sodium. A nickel sulfide is identified as well as an iron-titanium mineral.

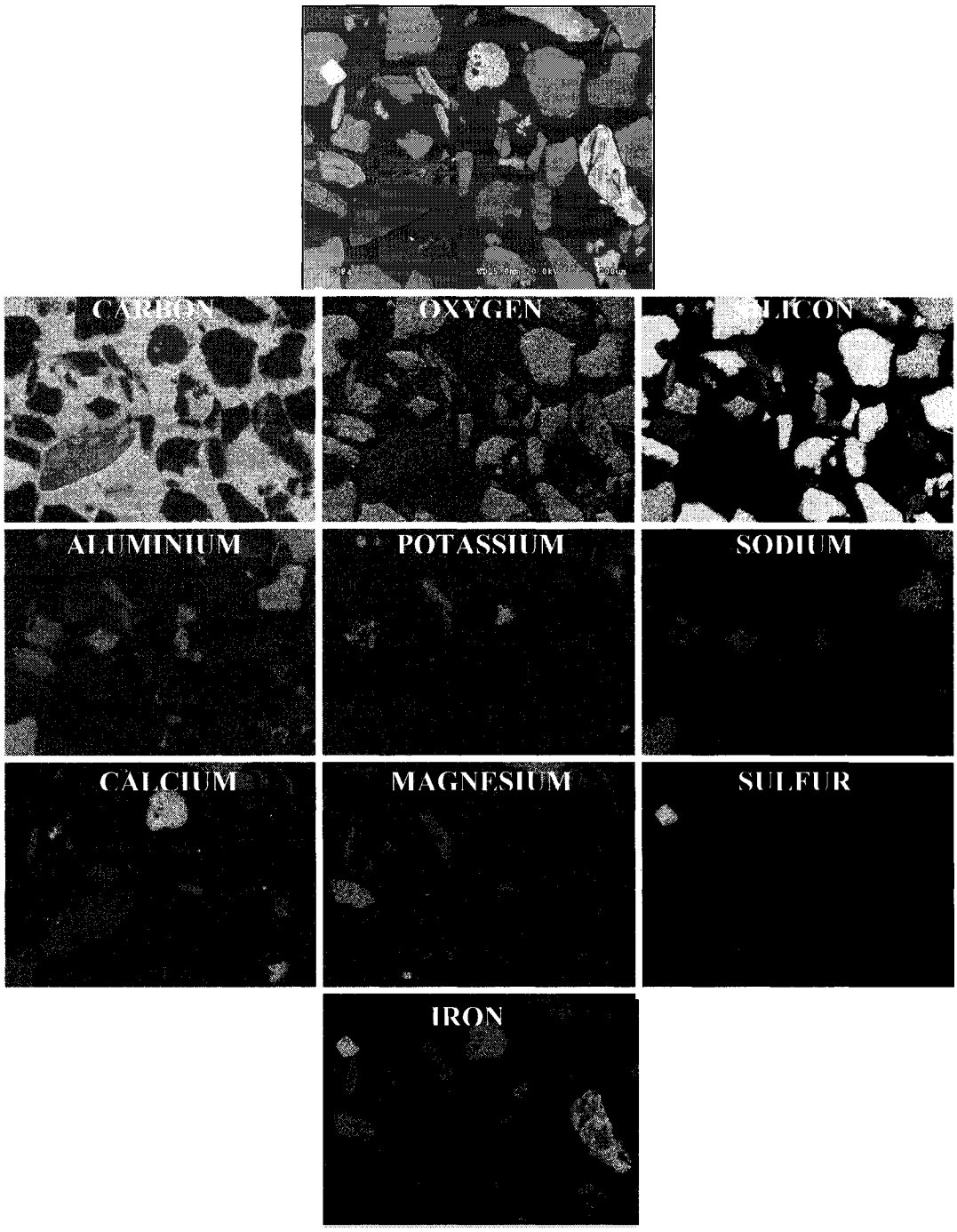

Figure B.5: X-ray map of a cluster of detrital particles. Quartz is the dominant mineral in this group, along with various aluminosilicates. An iron oxide is identified along with a calcium oxide and iron sulfide.

APPENDIX C

NICKEL PARTICLE X-RAY MAPS

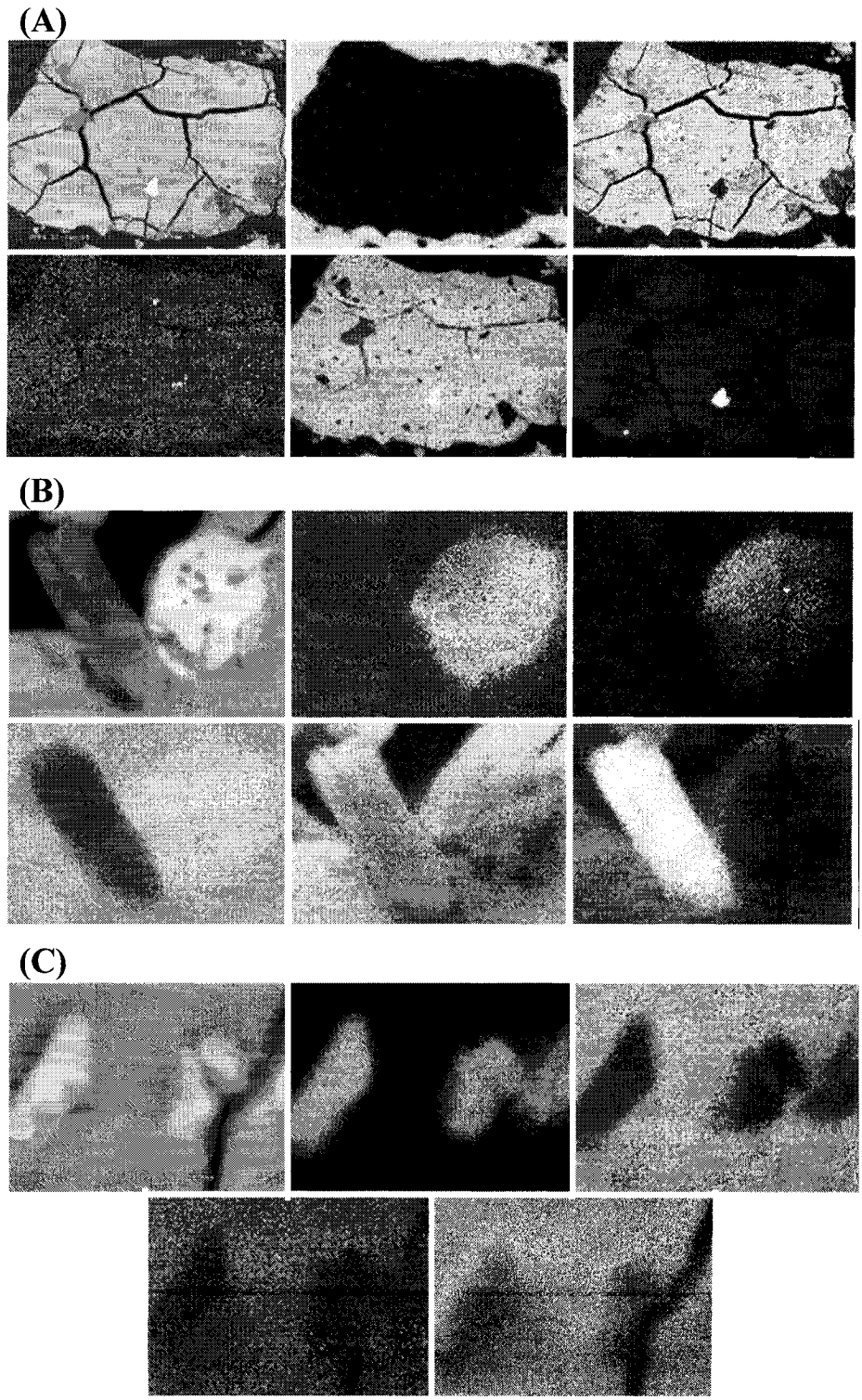

Figure C1: X-ray maps of sludge at pH 3 after 0.5 hours of leaching.

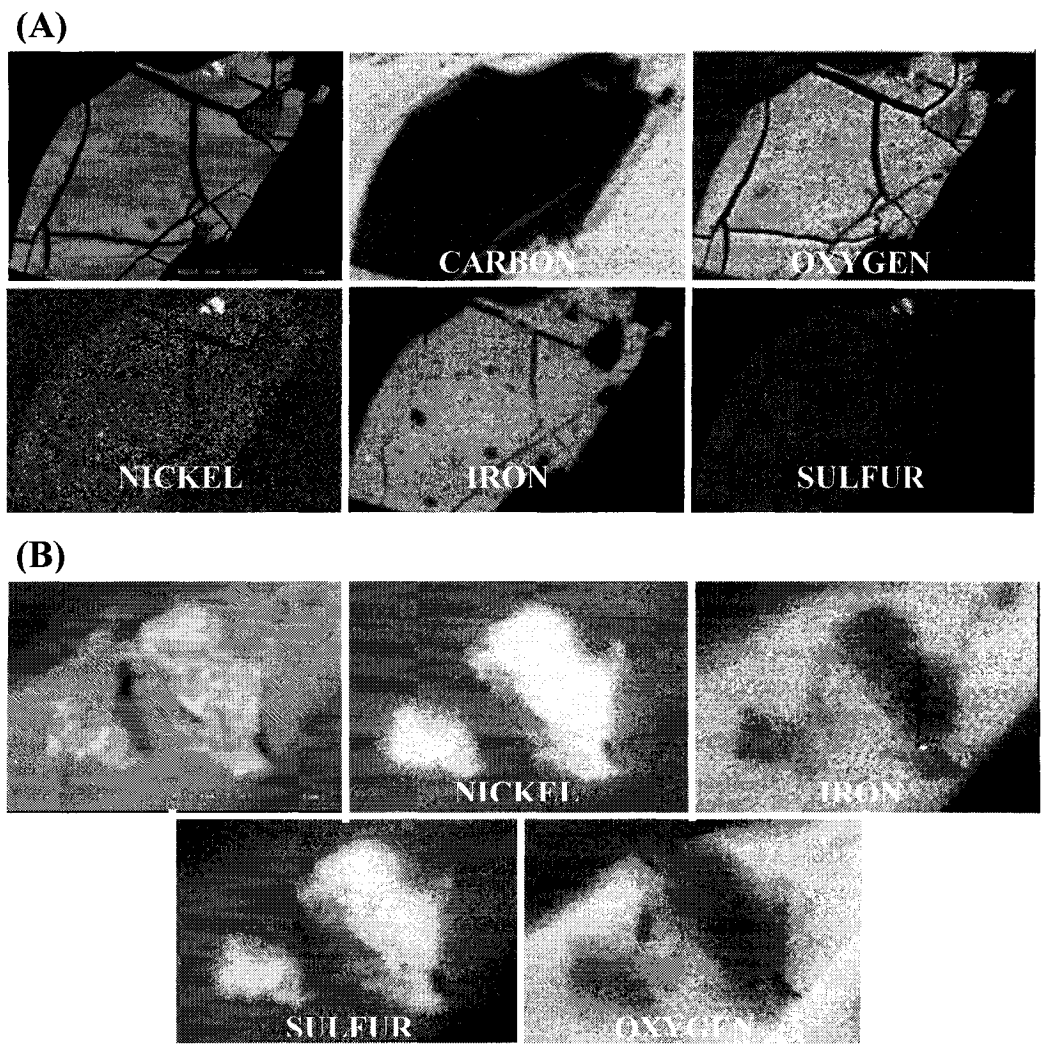

Figure C2: X-ray maps of sludge at pH 3 after 0.5 hours of leaching.

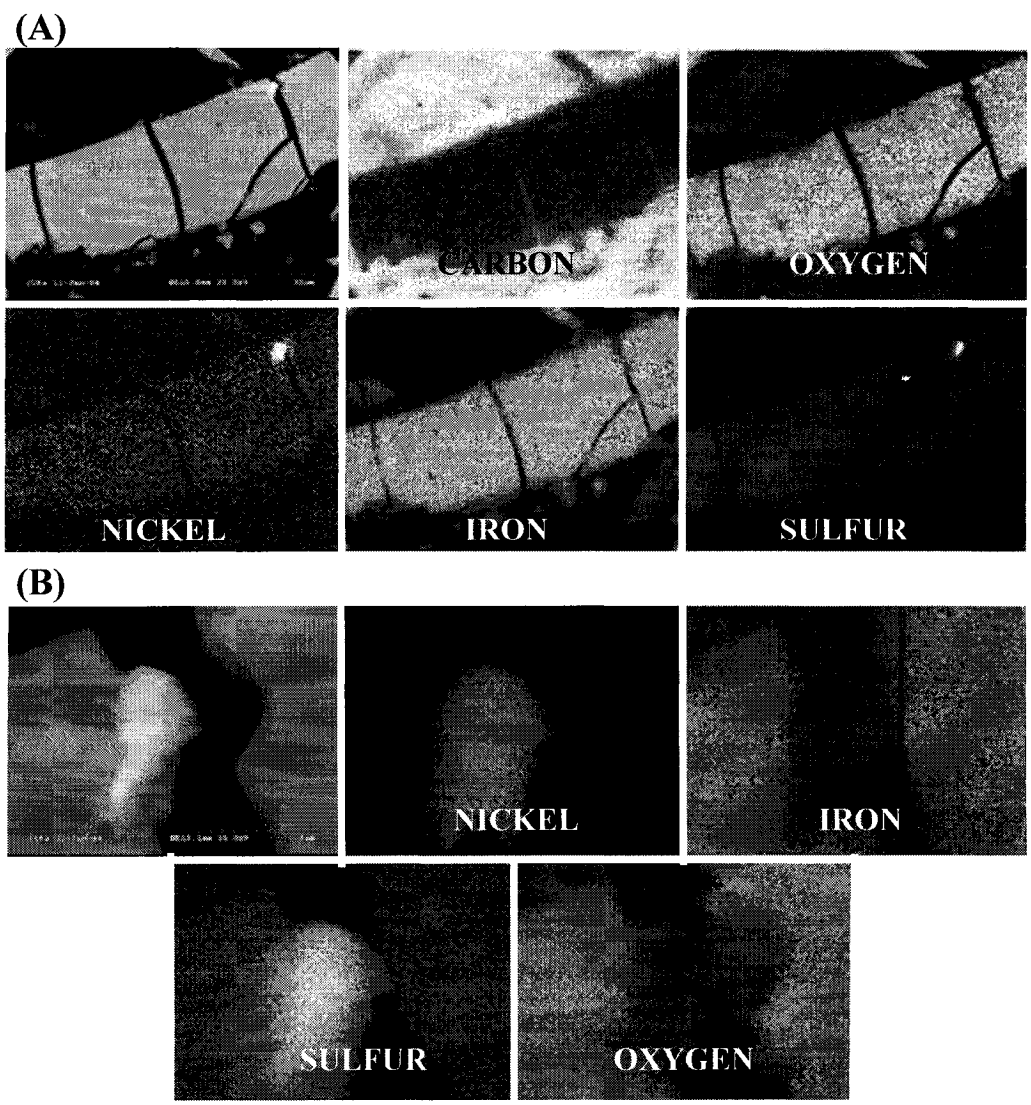

Figure C3: X-ray maps of sludge at pH 3 after 1.0 hours of leaching.

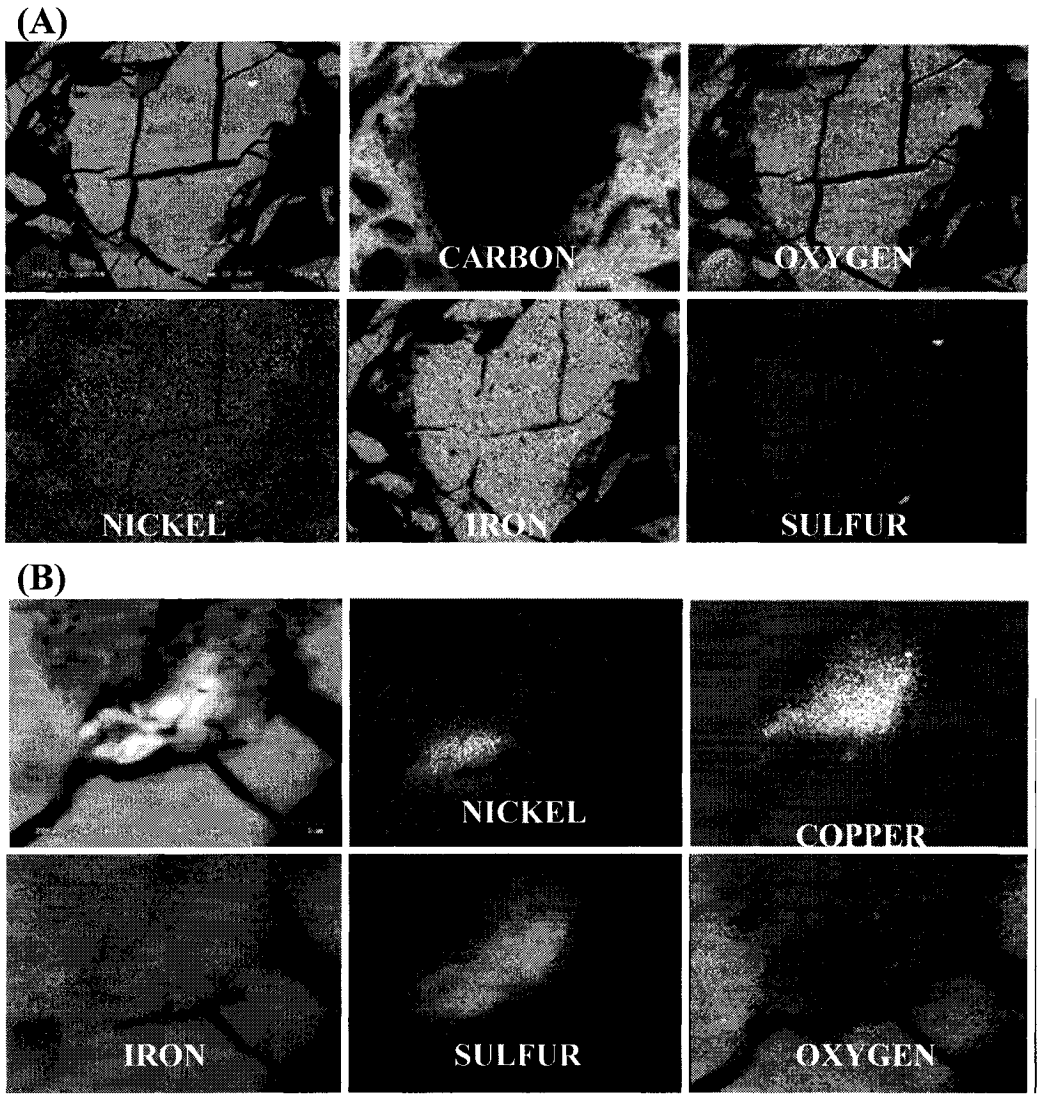

Figure C4: X-ray maps of sludge at pH 3 after 1.0 hours of leaching.

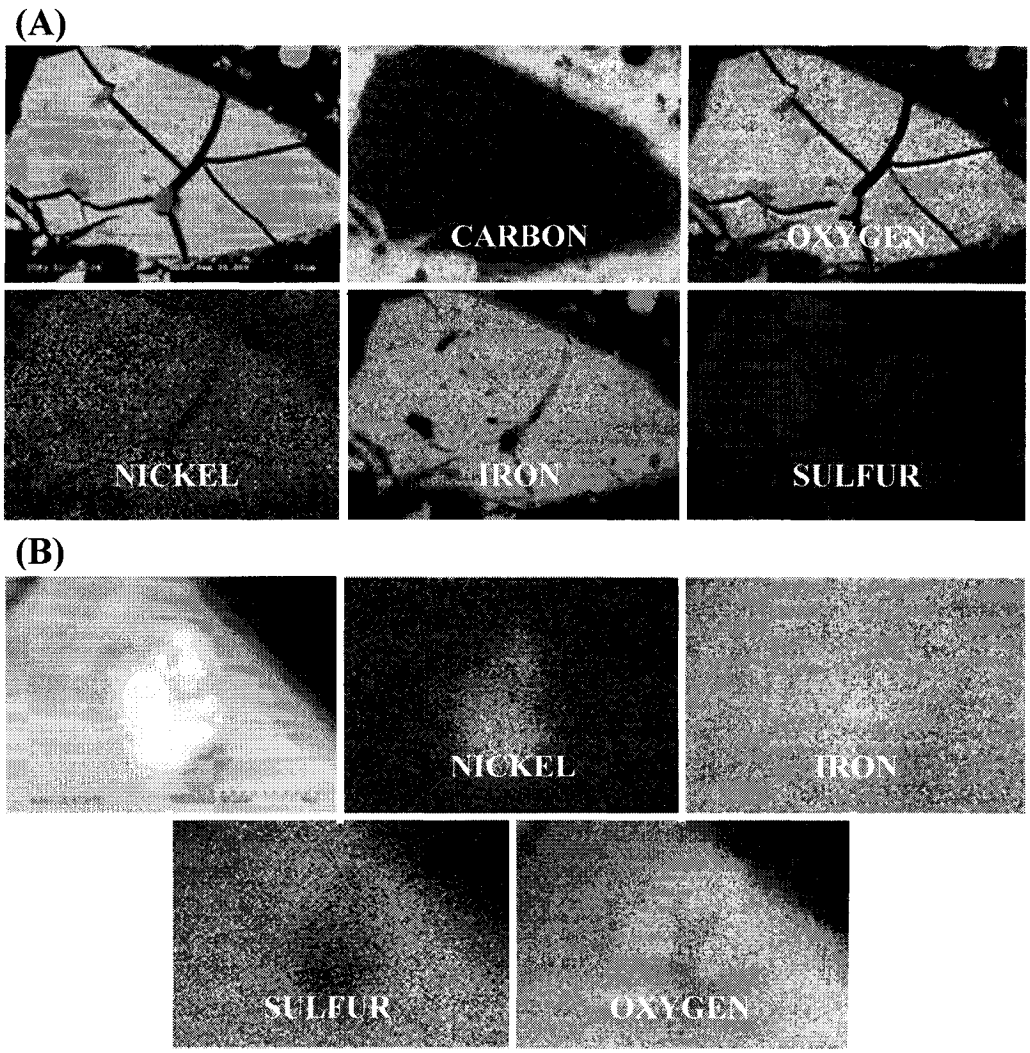

Figure C5: X-ray maps of sludge at pH 3 after 1.5 hours of leaching.

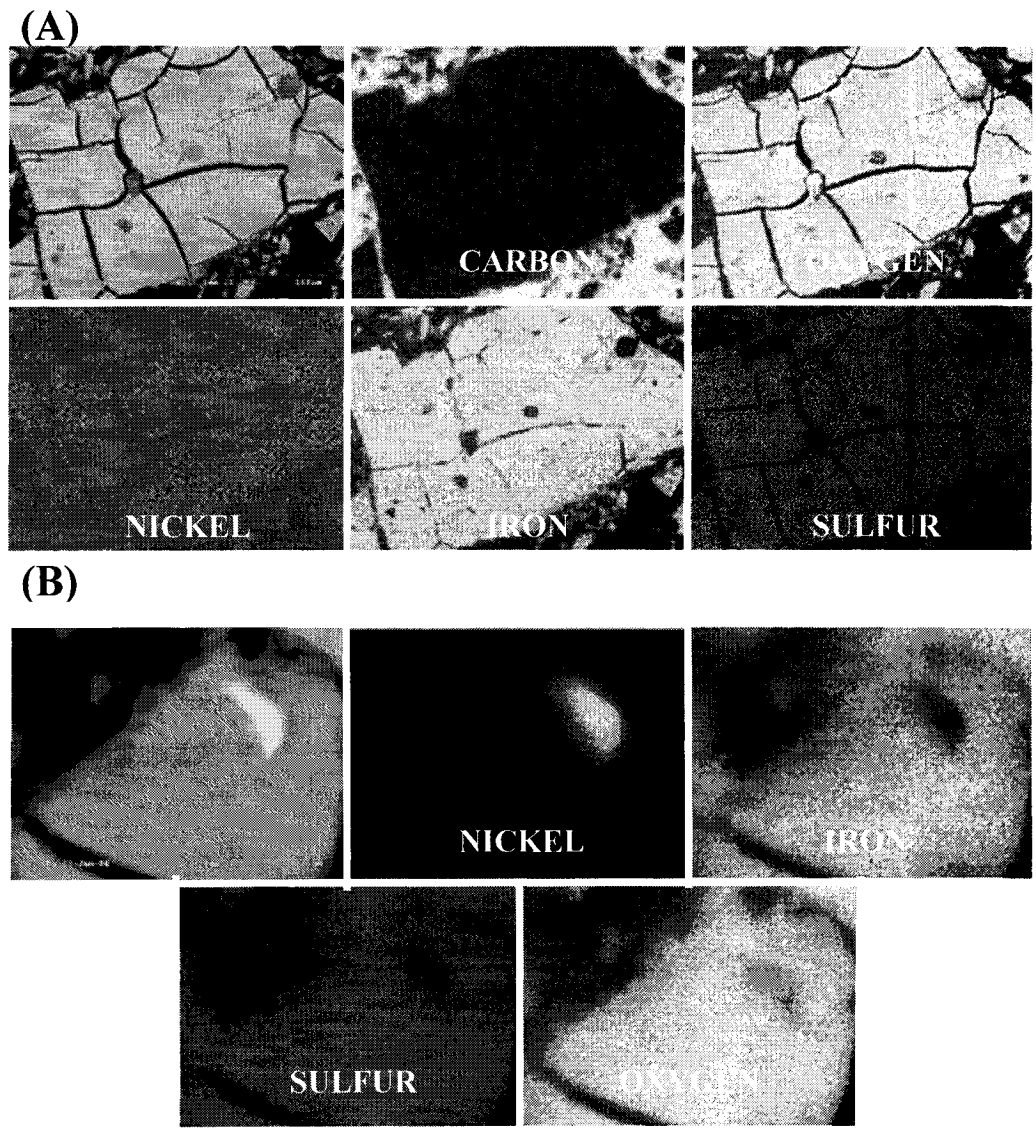

Figure C6: X-ray maps of sludge at pH 3 after 1.5 hours of leaching.

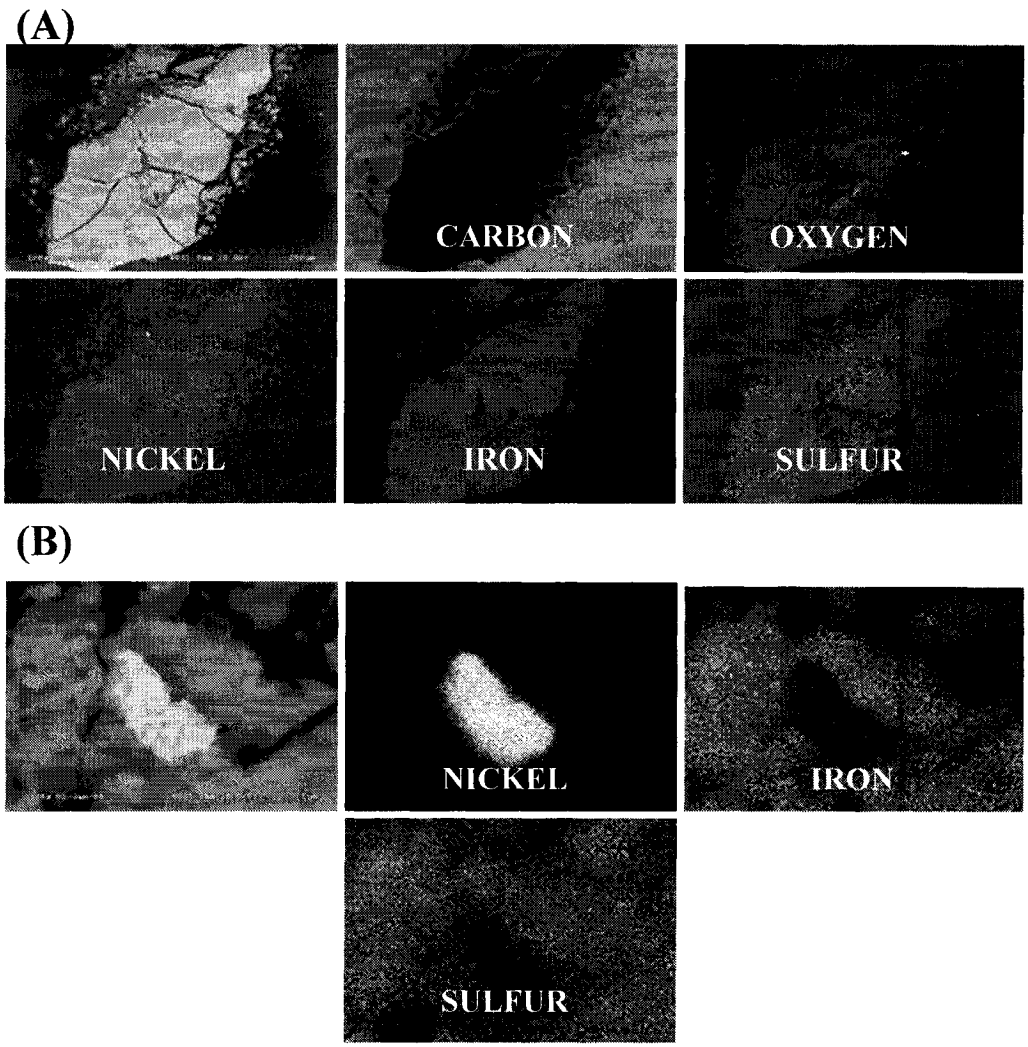

Figure C7: X-ray maps of sludge at pH 4 after 0.5 hours of leaching.

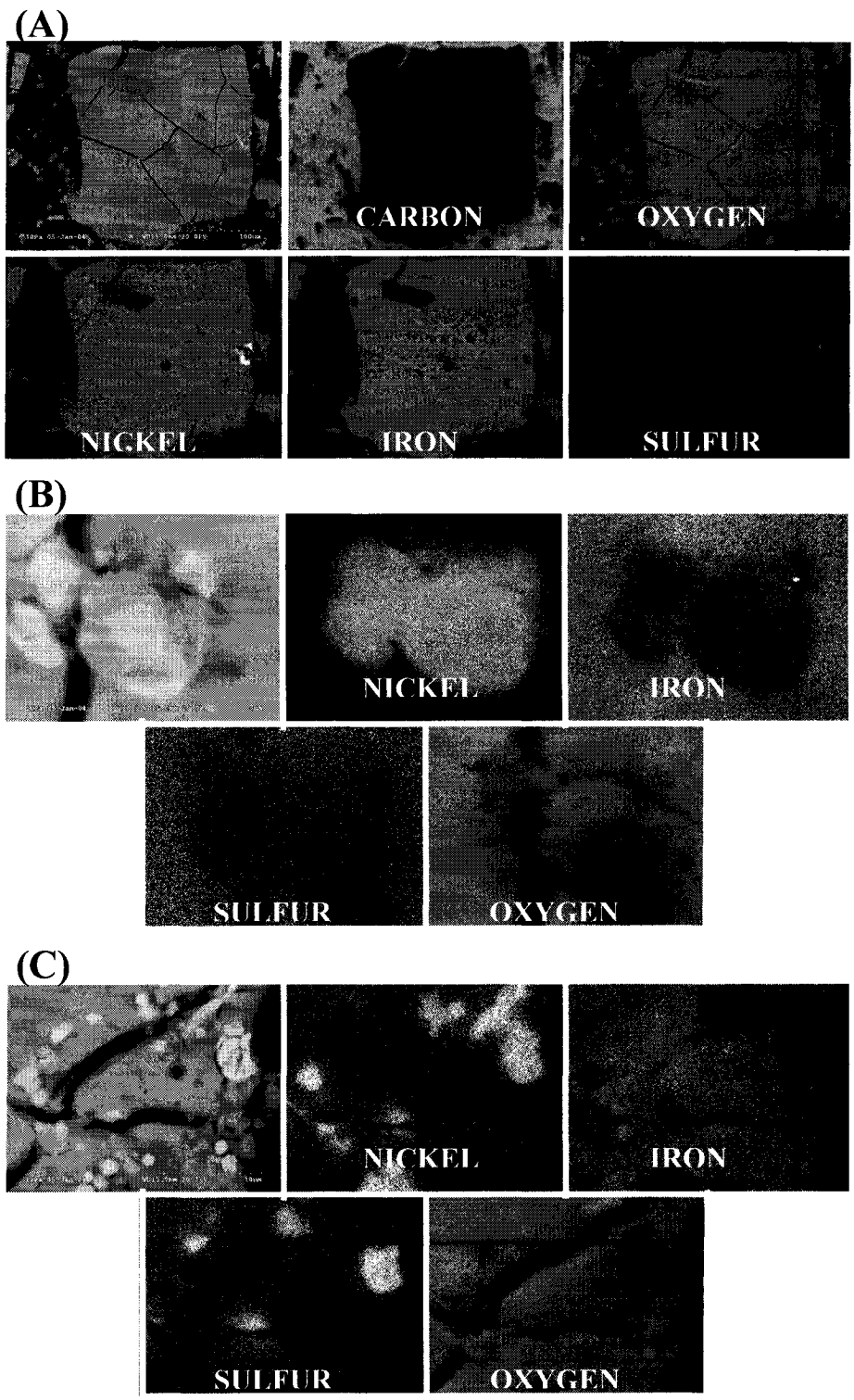

Figure C8: X-ray maps of sludge at pH 4 after 1.0 hours of leaching.

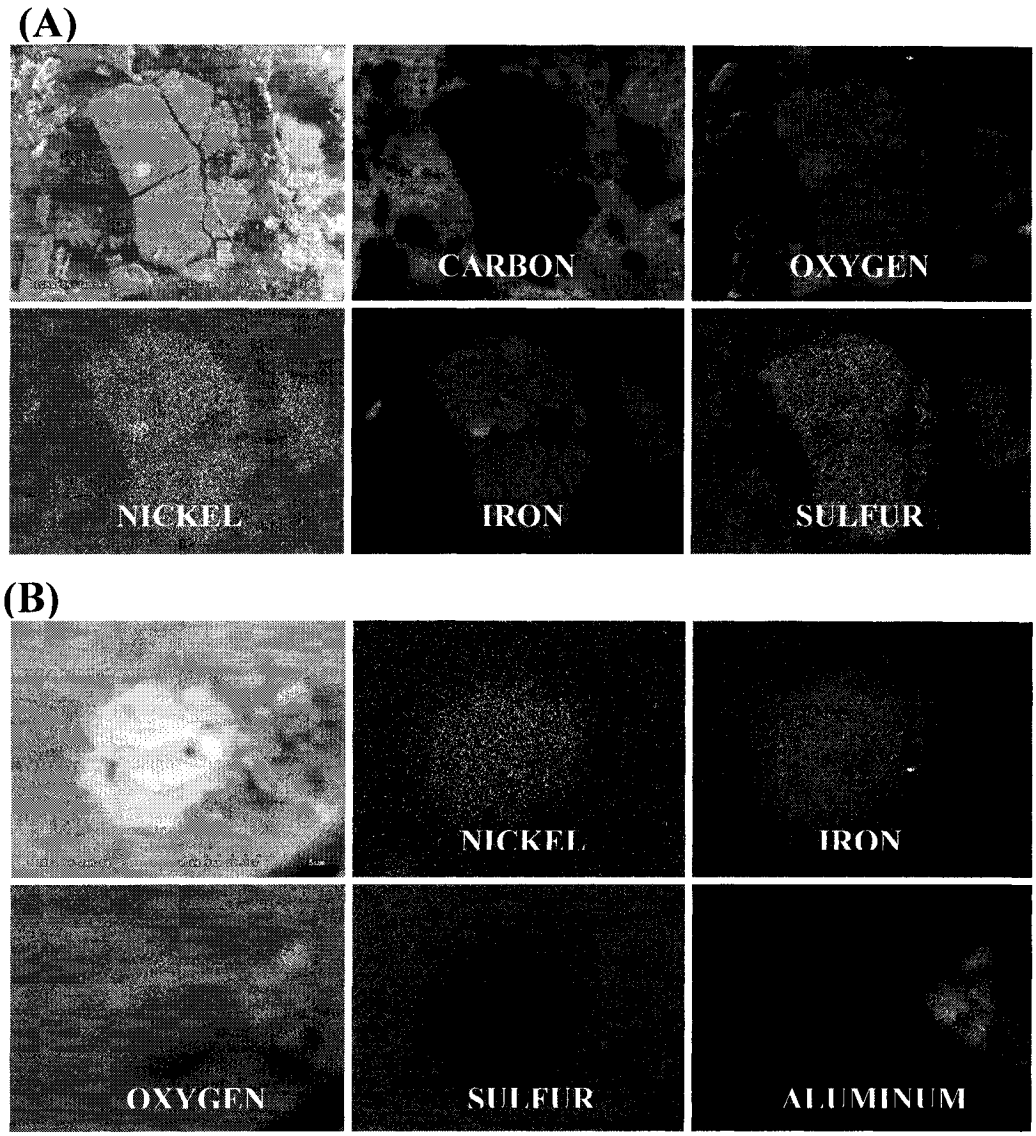

Figure C9: X-ray maps of sludge at pH 4 after 1.5 hours of leaching.

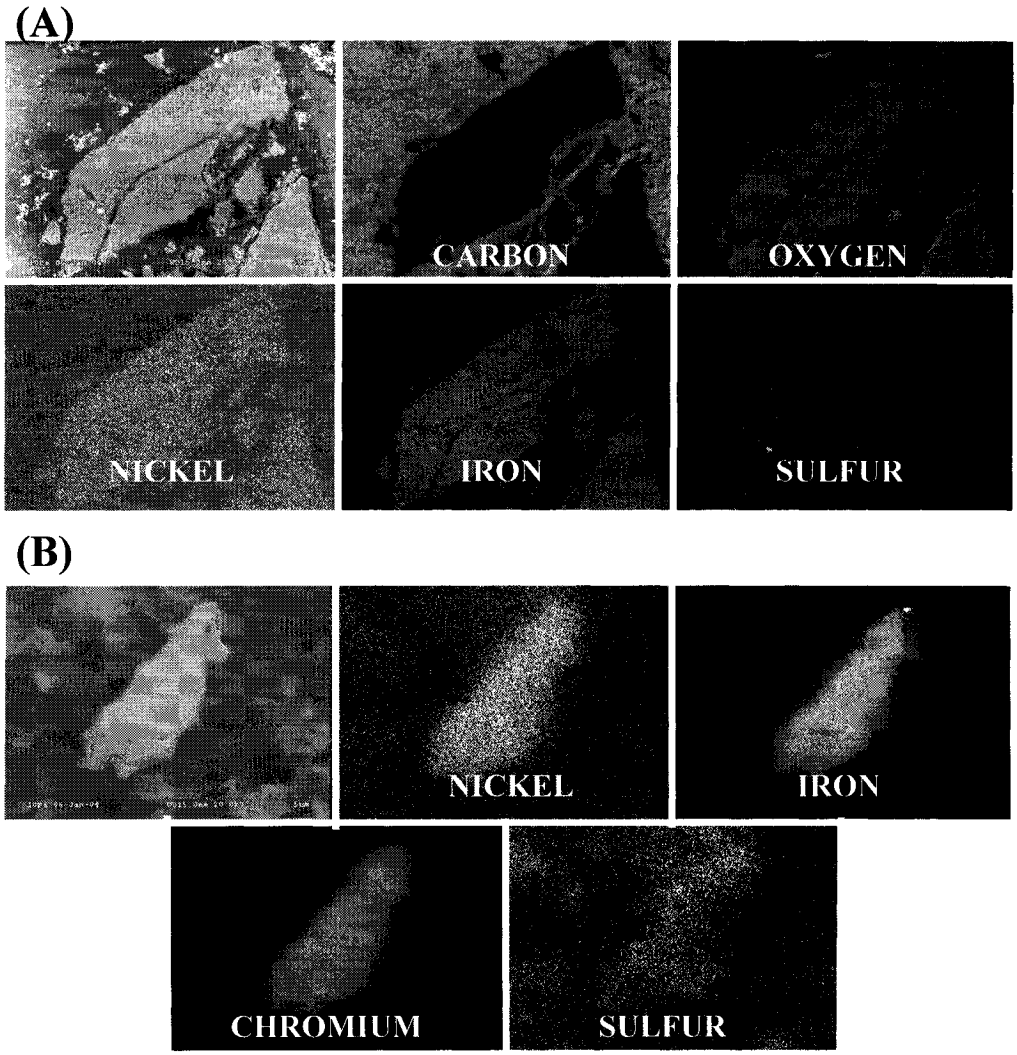

Figure C10: X-ray maps of sludge at pH 4 after 1.5 hours of leaching.

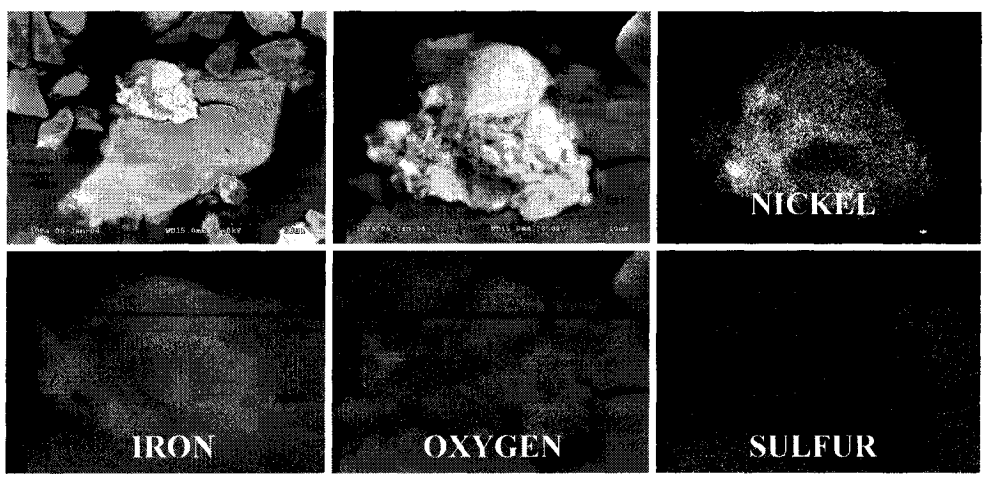

Figure C11: X-ray maps of sludge at pH 4 after 2.0 hours of leaching.

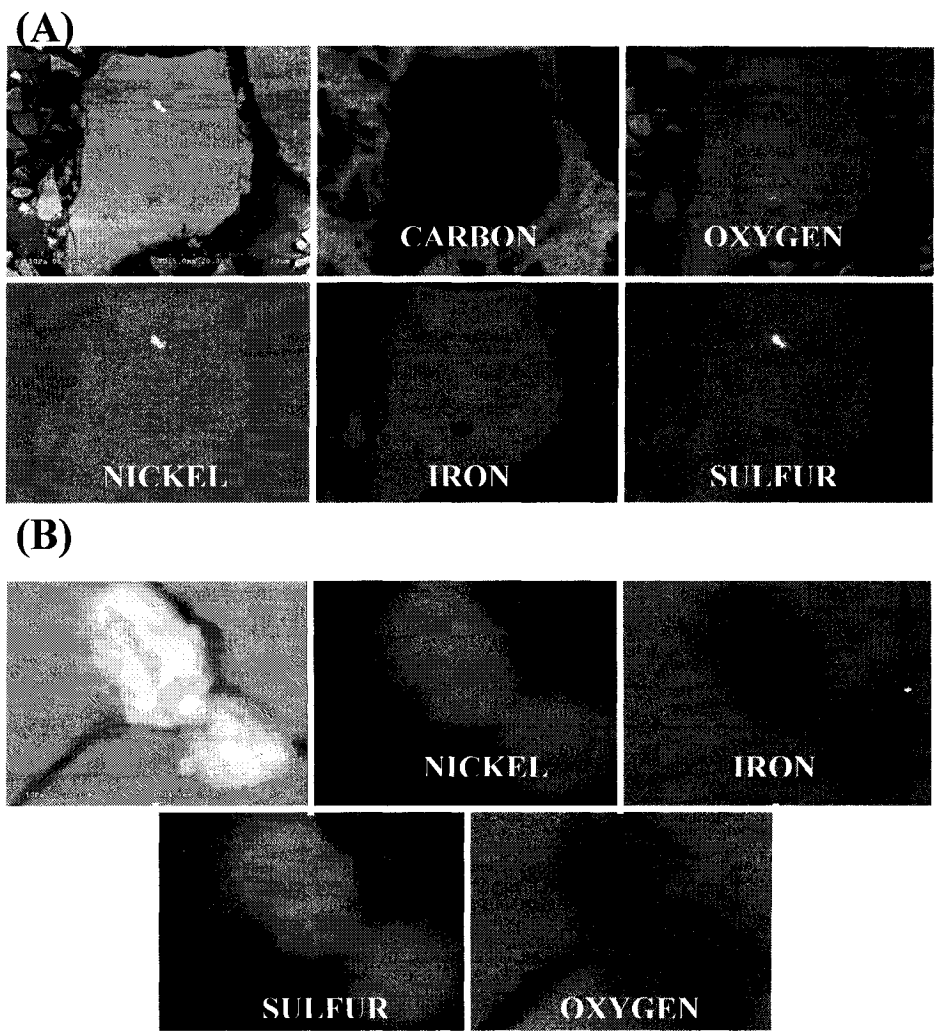

Figure C12: X-ray maps of sludge at pH 4 after 2.0 hours of leaching.

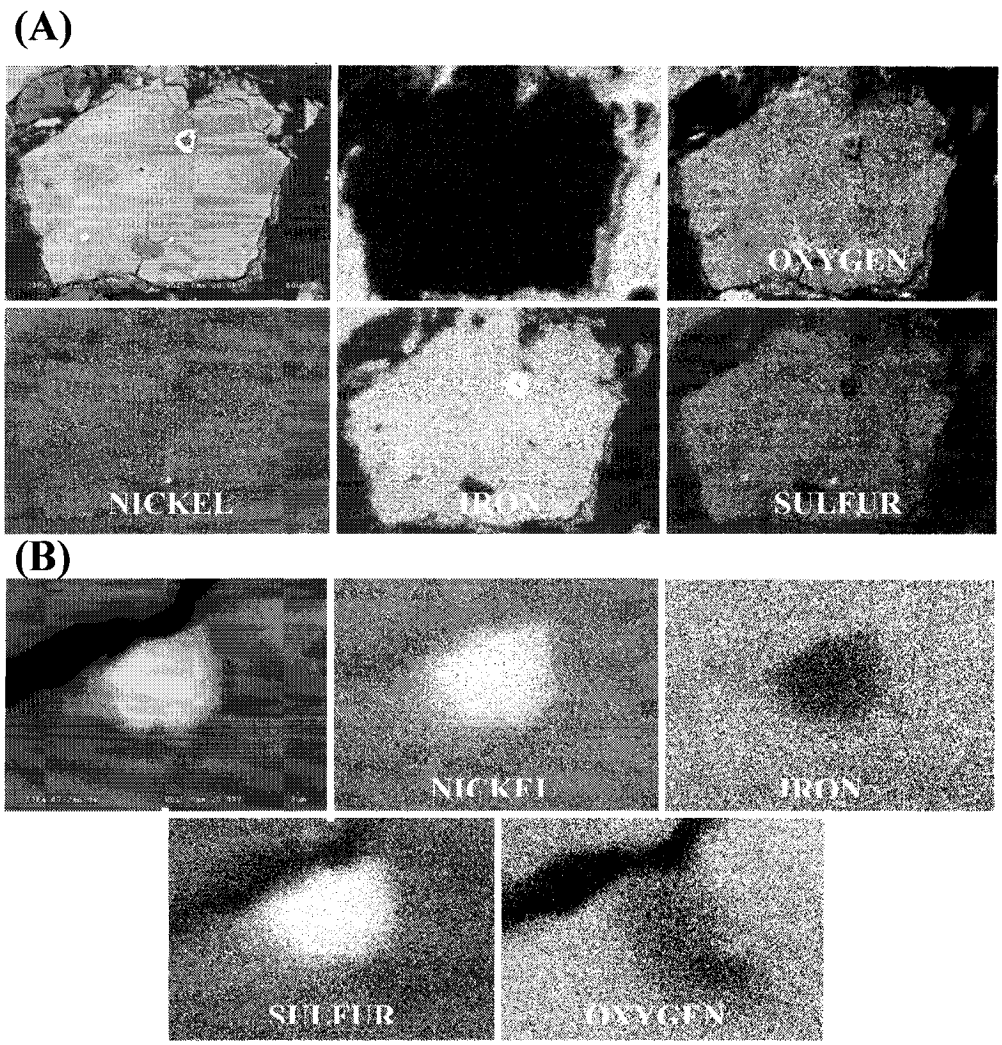

Figure C13: X-ray maps of sludge at pH 3.5 after 0.5 hours of leaching.

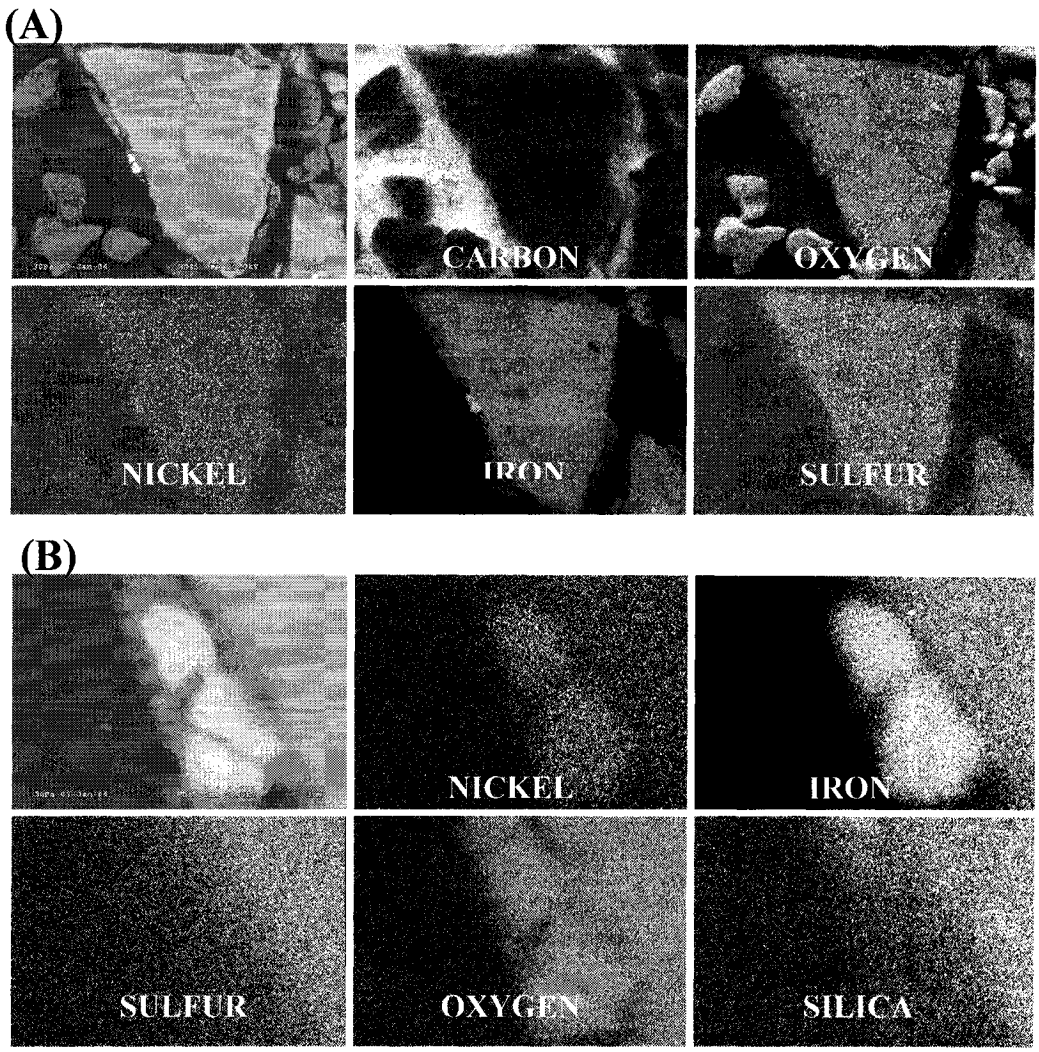

Figure C14: X-ray maps of sludge at pH 3.5 after 0.5 hours of leaching.

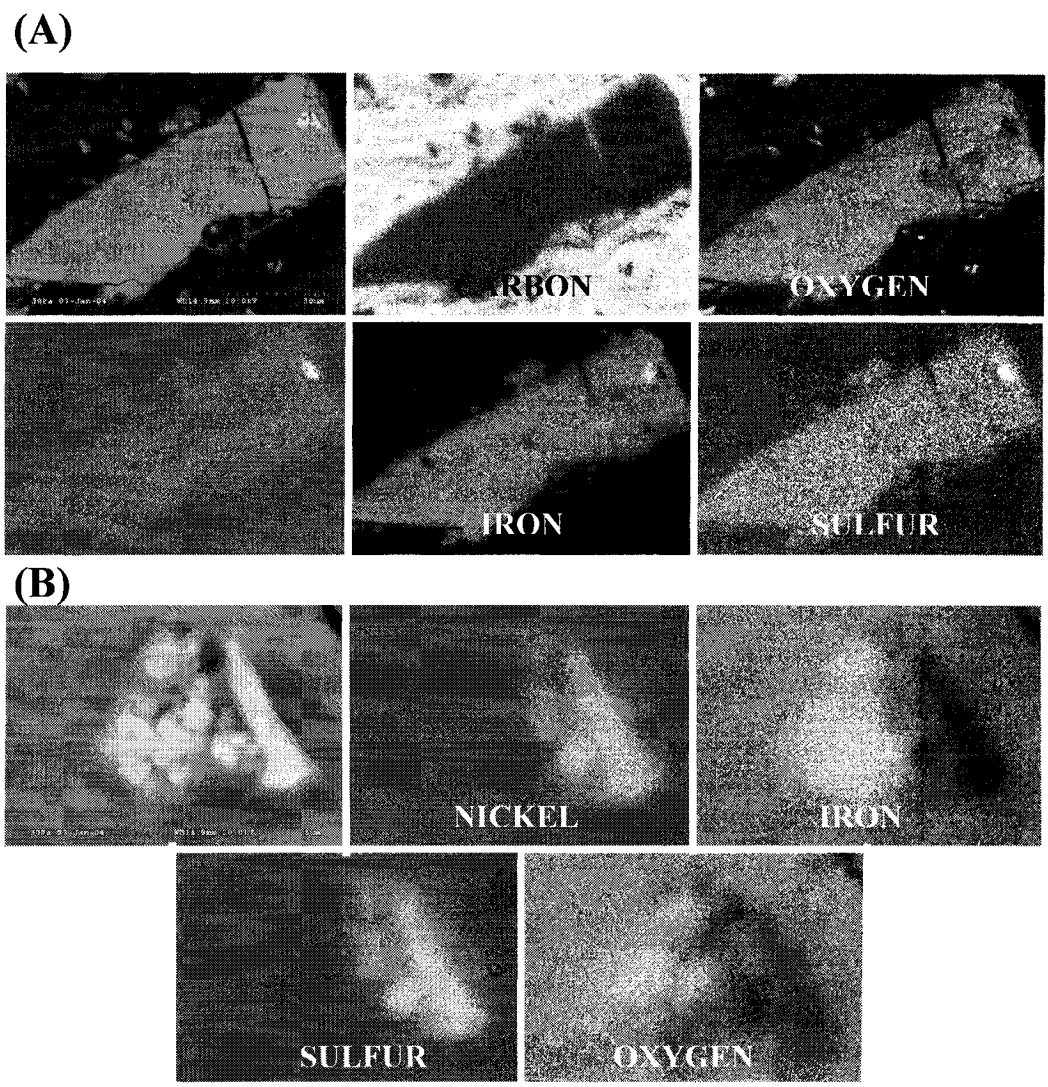

Figure C15: X-ray maps of sludge at pH 3.5 after 1.0 hours of leaching.

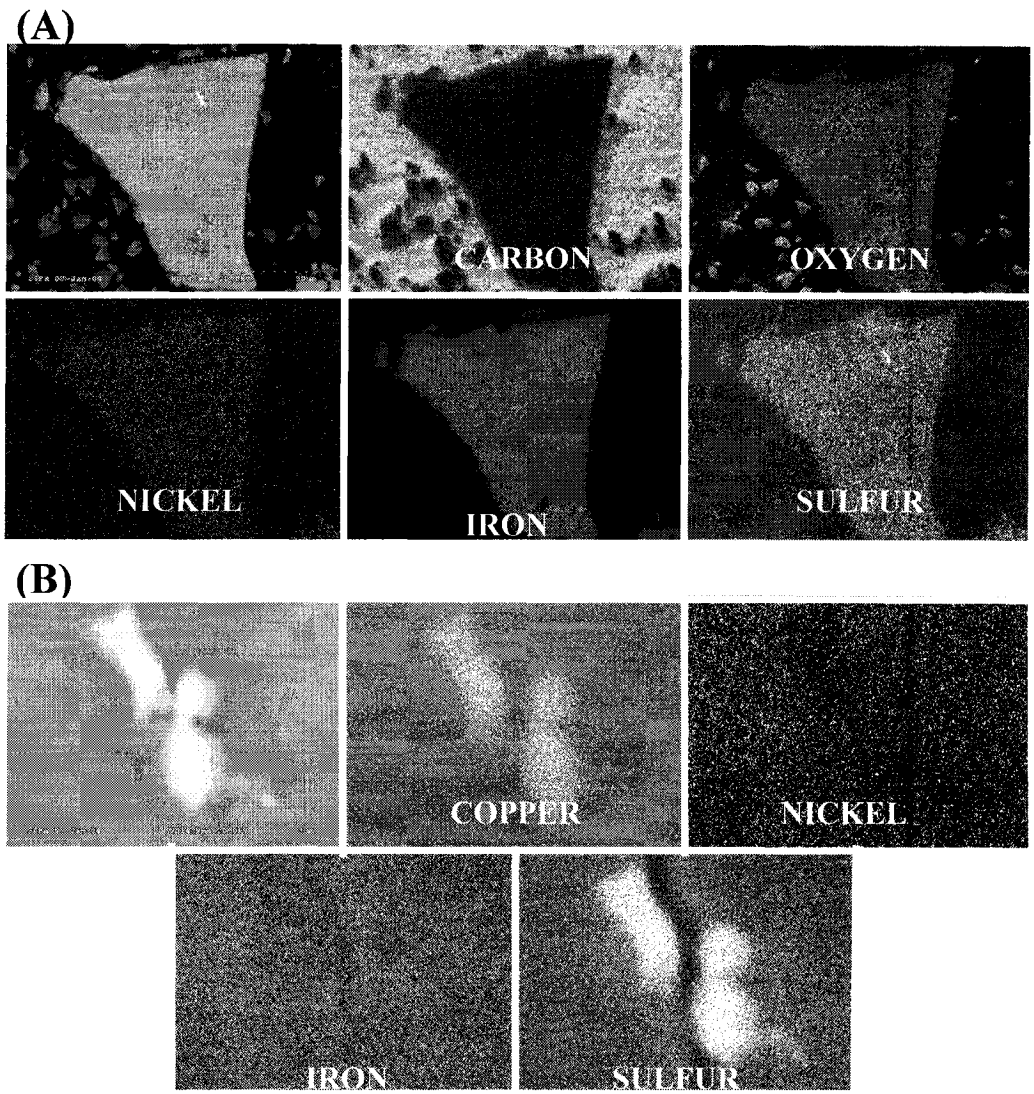

Figure C16: X-ray maps of sludge at pH 3.5 after 1.0 hours of leaching.

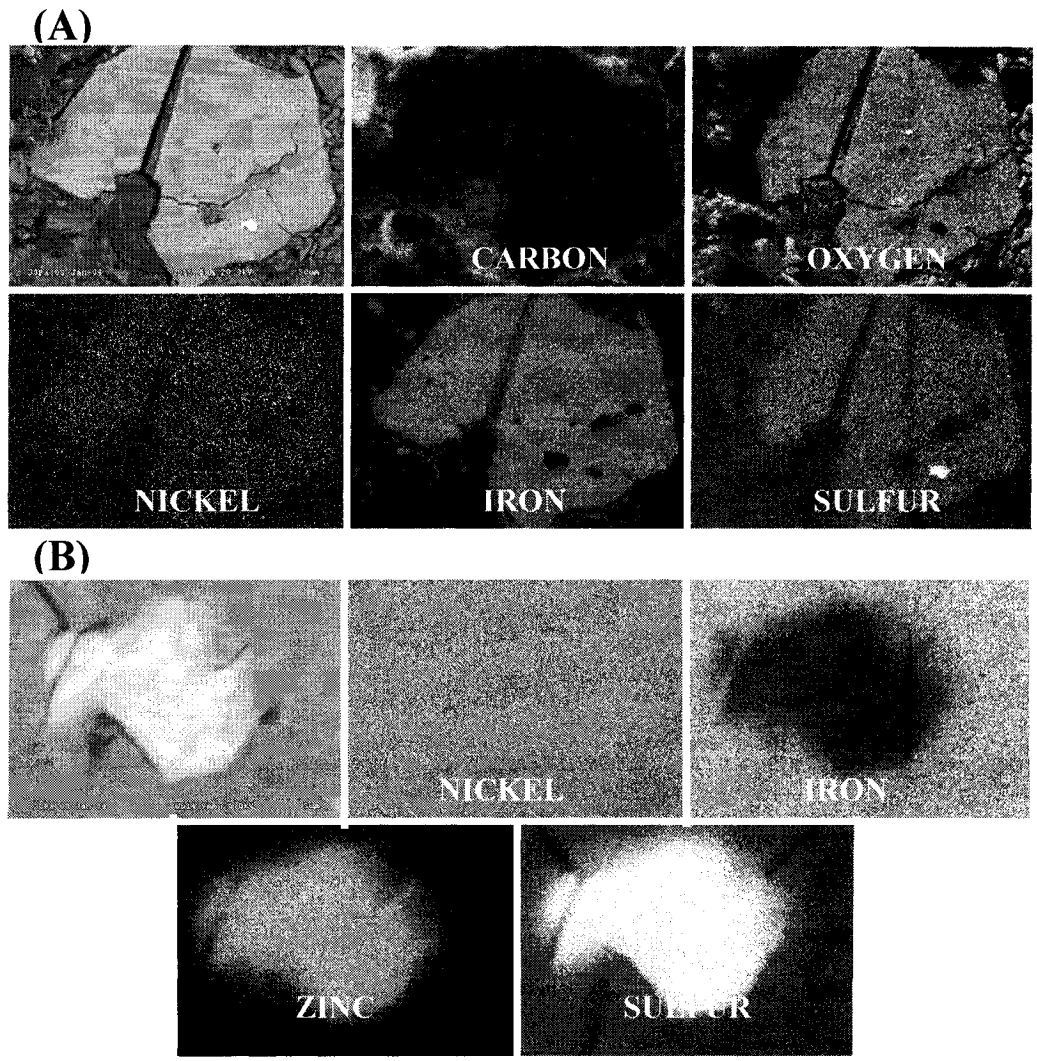

Figure C17: X-ray maps of sludge at pH 3.5 after 1.5 hours of leaching.

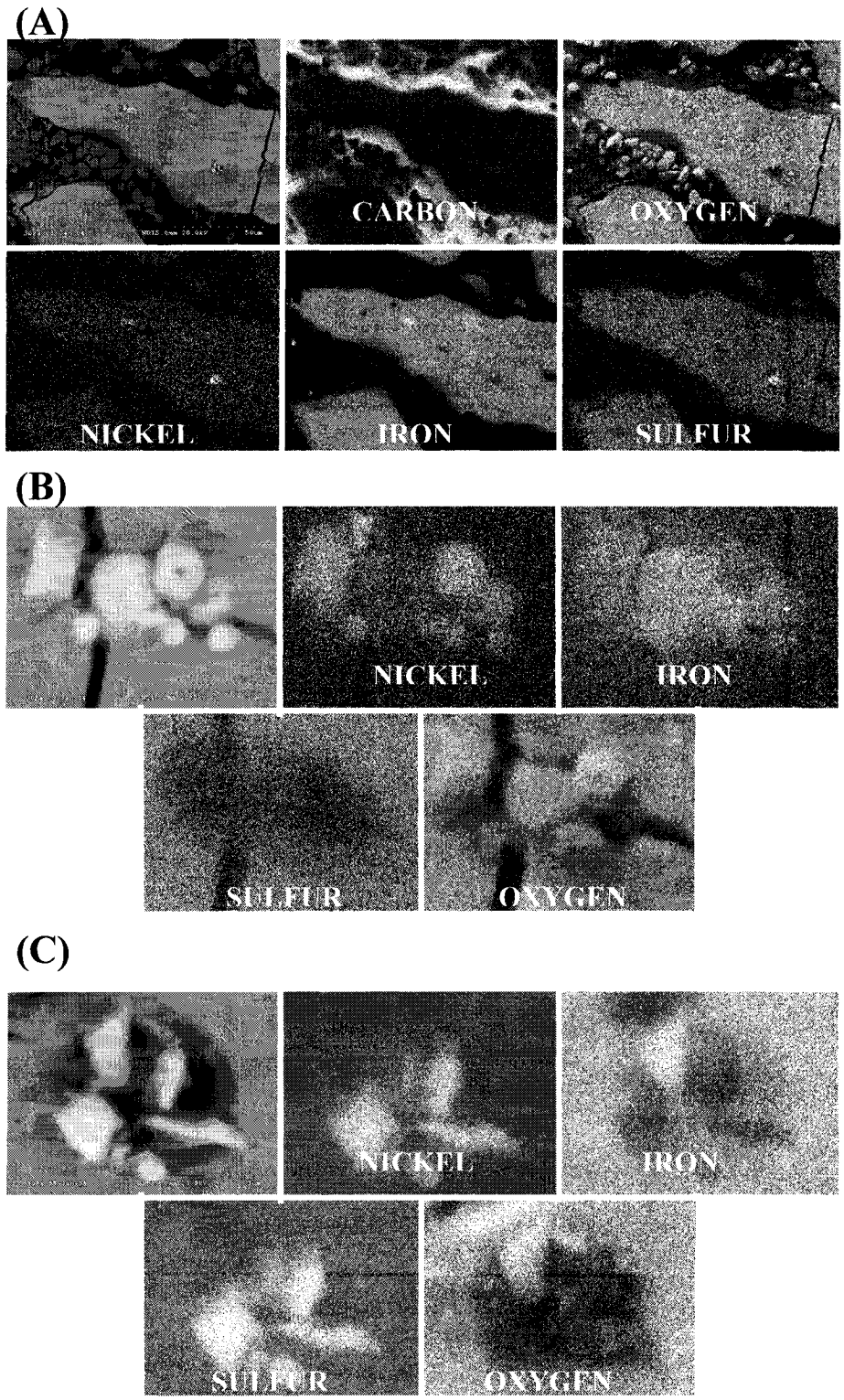

Figure C18: X-ray maps of sludge at pH 3.5 after 1.5 hours of leaching.

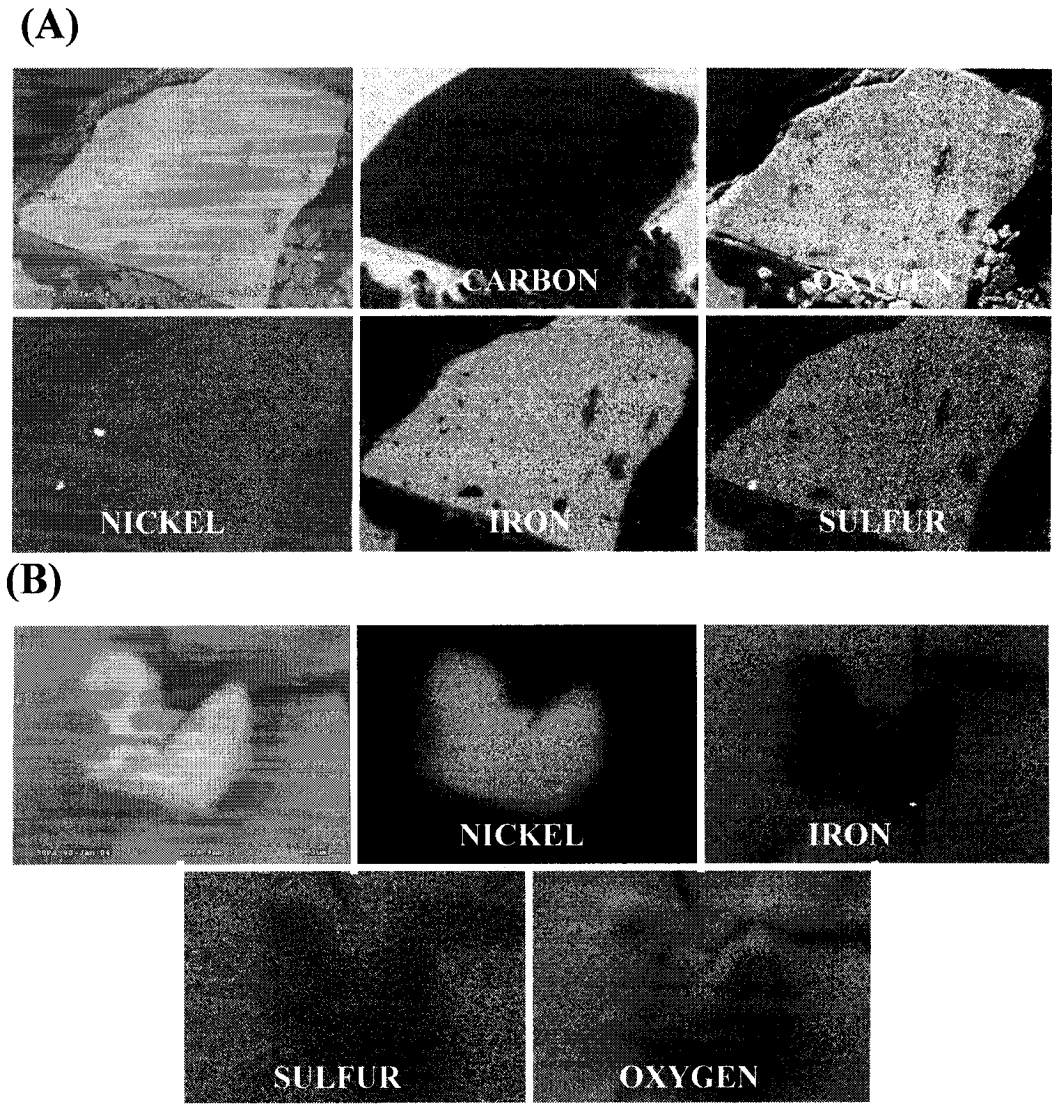

Figure C19: X-ray maps of sludge at pH 3.5 after 2.0 hours of leaching.

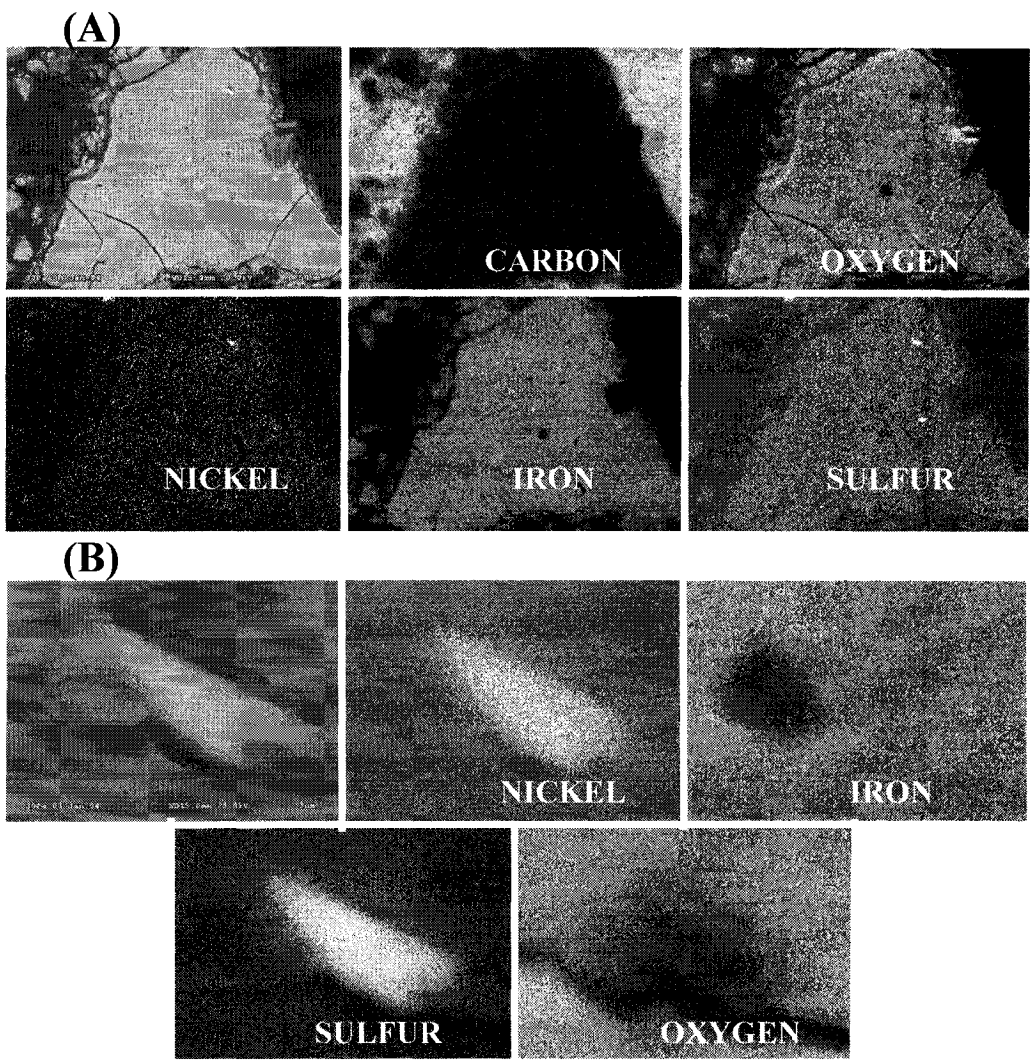

Figure C20: X-ray maps of sludge at pH 3.5 after 2.0 hours of leaching.

APPENDIX D

SLUDGE HOMOGENEITY

Figure D1: Image of sludge leach residue at pH 3. Numbers 1, 2 and 3 indicate the locations where a spectra was acquired for homogeneity testing.

Figure D2: Image of sludge leach residue at pH 3. Numbers 1, 2 and 3 indicate the locations where a spectra was acquired for homogeneity testing.

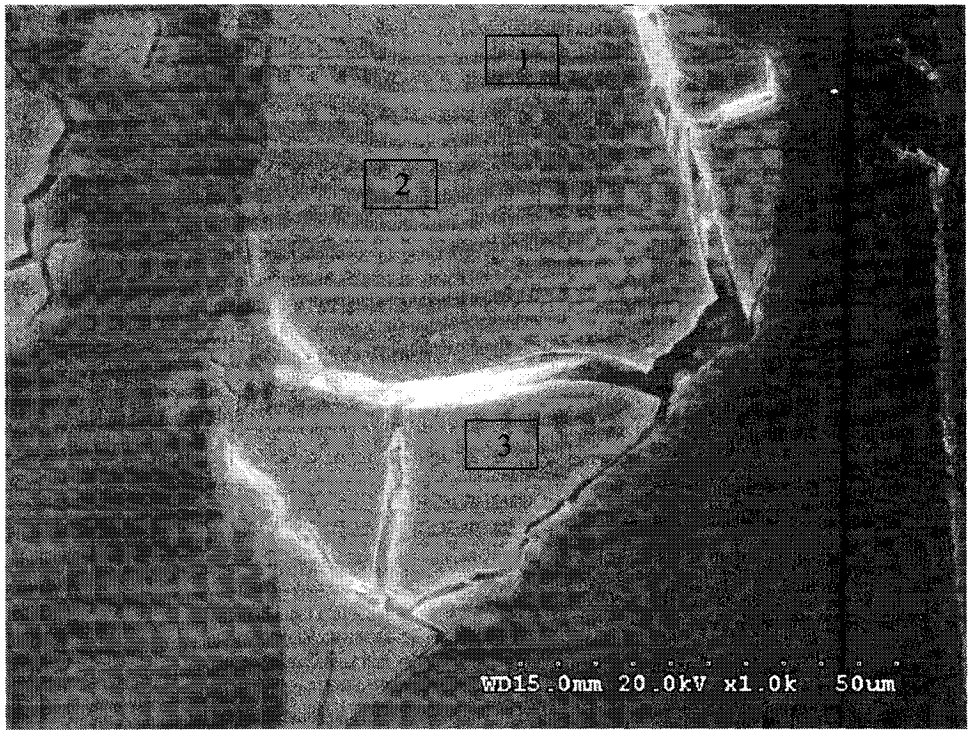

Figure D3: Image of sludge leach residue at pH 3. Numbers 1, 2 and 3 indicate the locations where a spectra was acquired for homogeneity testing.

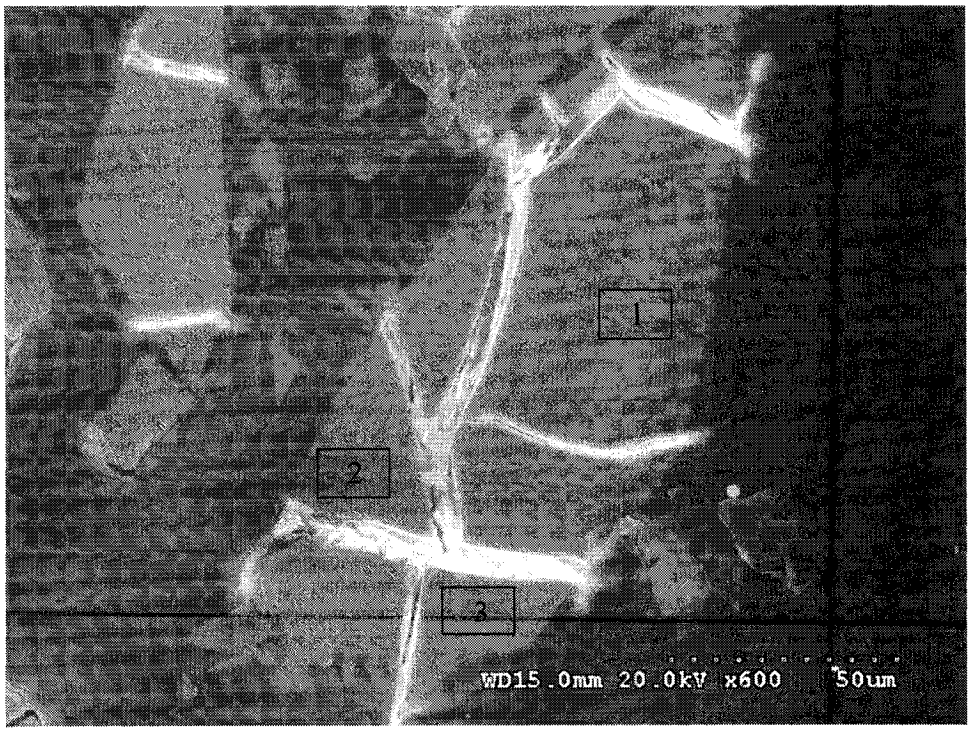

Figure D4: Image of sludge leach residue at pH 3. Numbers 1, 2 and 3 indicate the locations where a spectra was acquired for homogeneity testing.